

ABSTRACT

Title of Document: Atomic-level Characterization of
Fe(001)/MgO(001)/Fe(001) Tunneling
Magnetoresistance Structures and Spin-polarized
Scanning Tunneling Microscopy

Jookyung Lee, Doctor of Philosophy, 2010

Dissertation directed By: Professor R. D. Gomez
Department of Electrical and Computer
Engineering

This thesis seeks to understand the Fe-MgO-Fe system through a series of atomic level studies of the topographic, electronic, and magnetic properties of these epitaxial films. This multilayer system is uniquely important because of its huge tunneling magnetoresistance (TMR) arising from spin coherence and strong spin filtering through the structure. MgO-based magnetic tunnel junctions have been actively investigated and are now successfully applied to commercial products such as non-volatile magnetic random access memories and read-write heads for hard disk. However, despite its popularity most work has been done on macroscopic samples and has focused on the device-level performance. Yet very little effort has been

devoted towards the understanding at the atomic length scales including the effects of atomic steps and local variation in stoichiometry. The primary goal of this work is to elucidate the interplay between morphology, stoichiometry, local magnetism, and local electronic properties. To this end a multifaceted approach was used involving atomic/magnetic force microscopy (AFM/MFM), scanning tunneling microscopy (STM), scanning tunneling spectroscopy (STS), Auger electron spectroscopy, and low energy electron diffraction (LEED), which were operated in the cleanest possible conditions under an ultra-high vacuum. I linked the morphology directly to the formation of different magnetic domain configurations as a function of growth temperature and film thickness. I also correlated these atomic-level properties to the device-level performance. By investigating the topography and the surface electronic density of states with length scales in the nanometer regime, I found that the films had extremely inhomogeneous surface states. Because the structural defects such as surface steps, deep trenches and grain boundaries, as well as the existence of chemical impurities can perturb the spin-coherent tunneling, our observation of the electronic inhomogeneity can provide a direct clue for explaining the diminished TMR phenomenon on real systems compared to the theoretical expectation, which is one of longstanding problems to achieve high TMR in actual devices.

In addition to the Fe/MgO/Fe work, I also demonstrated spin polarized STM which revealed the anti-ferromagnetic spin-structure of single crystal chromium and the magnetic domains structure of permalloy film on silicon oxide.

ATOMIC-LEVEL CHARACTERIZATION OF Fe(001)/MgO(001)/Fe(001)
TUNNELING MAGNETORESISTANCE STRUCTURES AND SPIN-POLARIZED
SCANNING TUNNELING MICROSCOPY

By

Jookyung Lee

Dissertation submitted to the Faculty of the Graduate School of the
University of Maryland, College Park, in partial fulfillment
of the requirements for the degree of
Doctor of Philosophy
2010

Advisory Committee:

Professor R. D. Gomez, Chairman/Advisor

Professor Isaak Mayergoyz

Professor Agis A. Iliadis

Professor Robert Newcomb

Professor Lourdes G. Salamanca-Riba (Dean's Representative)

© Copyright by
Jookyung Lee
2010

Dedication

Dedicated to my parents
for the support and love they provide me
throughout my life

Acknowledgements

It is my great pleasure to express the gratitude to all of those who have supported me during graduate school. First and foremost, I would like to thank my advisor Professor R. D. Gomez for endless support, for his patience and enthusiasm, and for his friendly encouragement. His guidance helped me in all the time of research and thesis writing. I could not have imagined having a better advisor and mentor for my PhD study.

I would also like to thank the dissertation committee members Professor Isaak Mayergoyz, Professor Agis Iliadis, Professor Robert Newcomb, and Professor Lourdes Salamanca-Riba for their time and effort in the evaluation of this dissertation.

I am very grateful to all my friends and colleagues at the Laboratory for Physical Sciences (LPS) for providing me a wonderful working environment and helping me solve problems frequently happened. Special thanks go to Dr. Charles Krafft and Dr. Michael Dreyer for continuous support and advice on my research. I also thanks to my fellow group members, Konrad Aschenbach, Dr. Seok-Hwan Chung, and Jin-Seock Ma as well as to former members Herman Pandana, Marcia

Golub, Jui-Ping Chiang, Harita Tenneti, and Chao-Wei Chen for their help and friendship.

Lastly, I am deeply indebted to my parents Seung-Kiu Lee and Boo-Young Jung and my brother Jung-Hun Lee, who have always provided the unconditional support and love, and to my best friend Mark Keats, whose advice, support and participation were invaluable.

Table of Contents

| | |
|--|-----|
| Dedication | ii |
| Acknowledgements | iii |
| Table of Contents | v |
| List of Tables..... | ix |
| List of Figures | x |
| 1. Introduction..... | 1 |
| 2. Theoretical Modeling for Spin Dependent Tunneling | 6 |
| 2.1 Introduction..... | 6 |
| 2.2 Free Electron Models | 8 |
| 2.2.1 Simple tunneling problem | 8 |
| 2.2.2 Julliere model..... | 12 |
| 2.2.3 Slonczewski model..... | 15 |
| 2.3 Density Functional Theory..... | 17 |
| 2.3.1 Types of first principle methods..... | 17 |
| 2.3.2 Principles of density functional theory..... | 19 |
| 2.3.3 Exchange-correlation energy (E_{XC}) in density functional theory..... | 22 |
| 2.3.4 Implementations of density functional theory..... | 24 |
| 3. Theoretical Calculation for Fe/MgO/Fe (100) Epitaxial System..... | 26 |
| 3.1 Introduction..... | 26 |
| 3.2 Overview of Butler <i>et al.</i> 's first principle method | 29 |
| 3.2.1 The role of the symmetry in tunneling..... | 29 |

| | | |
|-------|---|----|
| 3.2.2 | The Layer Korringa-Kohn-Rostoker (LKKR) method | 31 |
| 3.2.3 | Transmission/Reflection matrices | 34 |
| 3.2.4 | Landauer conductance formula | 38 |
| 3.3 | Butler <i>et al.</i> 's calculation | 40 |
| 3.3.1 | Structure of iron-magnesium oxide..... | 41 |
| 3.3.2 | Electronic and magnetic structure | 42 |
| 3.3.3 | Tunneling conductance at zero bias for an Fe/MgO/Fe (001) | 47 |
| 3.4 | The effects of symmetry in Fe/MgO/Fe (001) at $k_{\parallel}=0$ | 53 |
| 4. | Overview of Scanning Probe Technique..... | 57 |
| 4.1 | Overview of Scanning Tunneling Microscopy/Spectroscopy..... | 57 |
| 4.1.1 | Tunneling phenomenon..... | 58 |
| 4.1.2 | Scanning Tunneling Microscopy (STM)..... | 63 |
| 4.1.3 | Scanning Tunneling Spectroscopy (STS) | 64 |
| 4.2 | Overview of atomic/magnetic force microscopy (AFM/MFM) | 67 |
| 4.2.1 | Interacting Forces between tip and sample | 68 |
| 4.2.3 | Magnetic Force Microscopy (MFM)..... | 72 |
| 5. | Study of Fe Ultrathin Films Grown Epitaxially on MgO (001)..... | 75 |
| 5.1 | Introduction | 75 |
| 5.2 | Experiments..... | 77 |
| 5.3 | Results and Discussions | 84 |
| 5.3.1 | Effect of temperature on morphology | 84 |
| 5.3.2 | Magnetic configurations..... | 87 |
| 5.3.3 | Magnetic images with ex-situ MFM | 90 |

| | |
|---|-----|
| 5.3.4 Post-annealing effect..... | 92 |
| 5.4 Conclusions..... | 93 |
| 6. STM/STS Study on the growth of Fe-MgO-Fe system on MgO(001) substrate | 95 |
| 6.1 Introduction..... | 95 |
| 6.2 Experiments..... | 97 |
| 6.3 Results and Discussion..... | 99 |
| 6.3.1 STM/STS study of Fe film on MgO (001)..... | 99 |
| 6.3.2 MgO film on Fe thick film (001) | 104 |
| 6.3.3 Growth of Fe/MgO/Fe junction structure..... | 108 |
| 6.4 Conclusions..... | 111 |
| 7. Implementation of Spin-polarized Scanning Tunneling Microscopy on single-crystal chromium (001)..... | 112 |
| 7.1 Introduction..... | 112 |
| 7.2 Spin-polarized STM..... | 115 |
| 7.3 Experiments..... | 118 |
| 7.3.1 Preparation of spin-polarized STM tips: | 118 |
| 7.3.2 Preparation of the Cr (001) sample | 119 |
| 7.4 Results..... | 124 |
| 7.4.1 Morphological and chemical influence on the local electronic structure of a clean Cr surface..... | 124 |
| 7.4.2 Nitrogen reconstruction on a clean Cr surface..... | 128 |
| 7.4.3 Preparation conditions for having a cleaned, less-damaged surface..... | 131 |
| 7.4.4 Implementation of spin-polarized STM on a Cr (001) crystal..... | 135 |

| | |
|--|-----|
| 7.4.5 Implementation of spin-polarized STM on a 200 nm thick Permalloy film | 140 |
| 7.5 Conclusions | 142 |
| 8. Future Work | 143 |
| APPENDIX A: Overview of the Omicron UHV System | 145 |
| A.1. Overview of the Omicron UHV system | 145 |
| A.2 Upgrading the preparation chamber of the UHV system | 147 |
| APPENDIX B: Design and Modification for the UHV System | 148 |
| B.1 Sample holder for the fast-entry lock | 148 |
| B.2 Shutter for three sputtering guns in the preparation chamber | 151 |
| B.3 Sample plate modification with an extended top plate | 152 |
| B.4 3-D drawing of a potential shutter for two additional sputtering guns | 153 |
| APPENDIX C: The Growth of Carbon Nanotubes (CNTs) on Silicon Oxide and Quartz Substrates | 154 |
| C.1 Procedures | 154 |
| C. 2 Results: Secondary Electron Microscopy (SEM) measurements | 155 |
| Bibliography | 158 |

List of Tables

| | |
|--|----|
| Table 5.1 The summary of the salient features from our observations..... | 94 |
|--|----|

List of Figures

Figure 2.1 A simple tunneling problem with a rectangular potential barrier: An electron moves from the left to right side, passing through the potential barrier (V_B). Their wavefunctions can be obtained by solving time-invariant Schrödinger equation. 8

Figure 2.2 Julliere's model: the tunneling current is proportional to the products of DOS for each spin in two electrodes. (a) When two ferromagnetic electrodes are magnetized in the same direction (parallel alignment), the current can be proportional to $N_1^\uparrow N_2^\uparrow + N_1^\downarrow N_2^\downarrow$, where $N_i^{\uparrow(\downarrow)}$ is the number of spin-up (down) electrons at Fermi level in the i -th electrode. Similarly, (b) when two electrodes are magnetized in the opposite direction (anti-parallel alignment), the tunneling current is proportional to $N_1^\uparrow N_2^\downarrow + N_1^\downarrow N_2^\uparrow$ 11

Figure 2.3 A classification of modern computational methods, which are widely used for calculating electronic structures of various systems. In particular, *ab initio*, or called first principle method, consists of three different approaches, Hartree-Fock (and post Hartree-Fock), density functional theory, and quantum Monte Carlo simulation. These three methods are alternatively used depending on the system. 18

Figure 2.4 Implementation of the density functional theory (DFT) methods, with the lists of approximations applied on a Schrödinger equation. 25

| | |
|--|----|
| Figure 3.1 Regrouping atomic orbitals into 4 symmetries (Δ_1 , Δ_5 , Δ_2 , and Δ_2') according to the symmetry criteria..... | 28 |
| Figure 3.2 Schematic overview of the LKKR calculation, repeated until self-consistent..... | 32 |
| Figure 3.3 Charge redistribution in the Fe/MgO/Fe system, from the calculation of Butler <i>et al.</i> Referred from [8] | 44 |
| Figure 3.4 Density of states for Fe (100) layers and for each spin near an interface with MgO. One hartree is 27.2 eV. Referred from [15]..... | 45 |
| Figure 3.5 Density of states for MgO layers and for each spin near an interface with Fe (100), referred from [15]..... | 46 |
| Figure 3.6 Majority conductance for 4, 8, 12 layers of MgO, calculated by Butler et al. Referred from [15]..... | 48 |
| Figure 3.7 Minority conductance for 4, 8, 12 layers of MgO, calculated by Butler et al. [15]..... | 49 |
| Figure 3.8 Conductance for the anti-parallel alignment of magnetic moments in the electrodes, calculated for 4, 8, 12 layers of MgO by Butler et al. [15]..... | 50 |
| Figure 3.9 Density of states calculated for a bcc Fe (100) bulk, referred from [37]; (a) crystal structure of a bcc Fe, (b) reciprocal lattice structure in Brillouin zone, and DOS for majority spin (c) and minority spin (d)..... | 52 |

Figure 3.10 Dispersion $k^2(E)$ for MgO in the range of the bandgap along the [100] direction. E_V is top of valence band, and E_C is the bottom of the conduction band. Referred from [15] 54

Figure 3.11 Tunneling DOS for $k=0$ for Fe/8 layers of MgO/Fe (100). Referred from [15] 56

Figure 4.1 Simple diagram of a one-dimensional electron tunnel junction, which can be applied to the STM setup as a tip-vacuum sample structure. Applied bias voltage (eV) makes the shift of the Fermi level between tip and sample. 58

Figure 4.2 Schematic illustration of the STM operation. A sharp metal tip attached on a piezoelectric tube is brought close to a sample, and scans the surface features by maintaining (a) a constant tunneling current (with feedback loop) or (b) a constant tunneling height (without feedback). At constant current mode, the tip position is recorded for topography, while at constant height mode the measured tunneling current is translated into the topography. 62

Figure 4.3 Energy diagram of a 1-D tip-vacuum-sample structure. Assuming that the tip has a featureless DOS, the DOS of the sample can only contribute the tunneling current as the function of the applied bias voltage. (a) At the positive bias voltage, the tunneling current can be proportional to the summation of the unoccupied states of the sample from the Fermi level to the bias, while (b) at the negative bias voltage, the current is the summation of the occupied states of the sample from the bias to the Fermi level..... 65

Figure 4.4 Schematic view of AFM detection: the deflection of cantilever is detected by the laser beam (IR LED), which is bounced on the rear side of the cantilever and then projected onto the position sensitive detector (PSD). 70

Figure 5.1 The Schematic of Fe growth on MgO (001) substrate. MgO has a NaCl-like face-centered cubic (fcc) structure with a lattice constant of 4.213 Å, and Fe has a body-centered cubic (bcc) structure with a lattice constant of 2.8666 Å. Thermodynamically, when Fe is deposited on MgO (001) crystal, Fe atoms rest on top of the O-site, which leads a good lattice match with a 45° rotation. 77

Figure 5.2 The preparation of MgO (001) substrate prior to Fe evaporation. The substrate was prepared by repeated cycles of sputtering with the energy of 1~1.5 keV and annealing up to 950 °C. The surface roughness (RMS) degraded with sputtering, and improved with annealing. The final surface state had an RMS roughness of less than 0.6 nm and a clear periodicity, as shown in the image of its Fourier transform (far right). 80

Figure 5.3 The effect of the annealing temperature on MgO (001) substrate. The AFM images describe the surface state after applying various temperatures of annealing, such as (a) less than 800 °C, (b) around 900 °C, (c) 930 ~ 960 °C, and (d) more than 1000 °C. Based on the improvement of roughness and periodicity, the optimized annealing temperature is found to be around 950 °C. 81

Figure 5.4 The Auger spectroscopy (AES) graphs onto the well prepared MgO (001) substrate. It shows clear peaks at an energy of around 500 eV and around 1150 eV, which correspond to the oxygen and magnesium peaks, respectively. Noticeably, the

carbon, which is the main contaminant in bulk MgO, is not apparent on the graph. While carbon was initially detected on AES, it disappeared under the noise level after repeated cleaning process..... 82

Figure 5.5 Low energy electron diffraction (LEED) images on an ultrathin Fe film grown at 400 °C on MgO (001) substrate. The diffraction energy for each of these images is (a) 40 eV, (b) 65 eV, and (c) 78eV. These images show the bcc crystalline structure of the Fe film, indicating a good epitaxial growth. 82

Figure 5.6 A thin Fe film grown on a MgO (001) substrate at room temperature. STM images of (a) 4 nm thick and (b) 14 nm thick film show that Fe grew as a random crystallite with overlapped round mounds. (c) The MFM image does not reveal any clear local magnetic variation, regardless of the thickness, except on a certain area that includes small magnetized particles, as shown in the image (d) (the MFM image of (d) is taken when Fe film is 0.5 nm thick. 83

Figure 5.7 STM/MFM images of 4 nm Fe thin film grown on a MgO (001) at 400 °C: (a) an STM image, (b) its 3-D implementation, (c) an MFM image and (d) its Fourier transform. According to the scan images, the Fe grew into pyramid-like islands with well-defined atomic terraces, and had a complex magnetic structure, which implies weak magnetic coupling..... 86

Figure 5.8 STM/MFM images of 14 nm Fe thin film grown on MgO (001) at 400 °C: (a) STM image, (b) its 3-D implementation, (c) MFM image and (d) the cross-section across the domain wall. 14 nm thick Fe formed pyramid-like islands, similar to the thin film. Magnetically, however, it had distinct features such as magnetic ripples

apparent along the magnetic easy-axis of bulk Fe. These ripples show long range magnetic ordering, implying stronger coupling. A 90° Néel wall was also found in MFM..... 89

Figure 5.9 MFM images measured in ambient condition on 14 nm thick Fe films, which are grown (a) at room temperature and (b) at high temperature of 400 °C. The room temperature sample showed a variety of magnetic domain walls such as Néel, Bloch, and cross ties, while the high temperature sample had a much simpler configuration. 90

Figure 5.10 STM and MFM images on the Fe thin film (< 4 nm thick), which was grown on MgO (001) substrate at room temperature and then annealed at a high temperature of 400 °C for 30 minutes..... 93

Figure 6.1 The schematic of the Fe/MgO/Fe (100) epitaxial system. Fe has a bcc structure with a lattice constant of 2.86 Å and MgO has a NaCl-like fcc structure with a lattice constant of 4.21 Å. A thin MgO film is sandwiched by two Fe structures, with a good lattice match (less than a 6 % mismatch). 96

Figure 6.2 STM images on a 25 nm thick Fe film grown on a cleaned MgO (001) substrate at a deposition temperature of 400 °C. The Fe grew into pyramid-like grains, which have crystallographic registry with the underlying MgO single-crystal. The scan areas were (a) 500 × 500 nm², (b) 200 × 200 nm², (c) 100 × 100 nm², and (d) 50 × 50 nm². 98

Figure 6.3 Simultaneous measurements of STM and STS on 25 nm thick Fe film grown on MgO (001) at 400 °C: (a) STM topography and the corresponding STS images (b) at +400 mV and (c) at 1V bias voltage. The STS conductivity maps have clear contrast differences in various regions. These regions can be sorted into 5 groups: terraces (T), step edges (SE), slope region (SL), upper right-handed area (W), and the bottom of a trench (B), which are labeled in the lower left-handed image. . 102

Figure 6.4 The corresponding STS data in various regions identified in figure 6.3: (a) current(i), (b) conductivity(di/dv), and (c) normalized conductivity(di/dv/(i/v)) versus bias voltage(v) spectra..... 103

Figure 6.5 Submonolayer of MgO deposited on thick Fe (001) film: STM topography at (a) less than 0.2 ML coverage (inset: zoomed image on a top flat terrace) and (b) slightly less than 1 ML coverage, and (c) corresponding spectroscopy data..... 105

Figure 6.6 STM images on 1 nm thin MgO layer deposited on thick Fe (001) film (a) at room temperature and then (b) annealed at 450 °C, and (c) the corresponding spectroscopy data. 106

Figure 6.7 STM/MFM study of Fe ($< 0.5 \text{ \AA}$)/ 3nm MgO/35 nm Fe structure grown epitaxially on MgO (001) substrate. STM images with increasing resolution: (a) in large area of $1\mu\text{m} \times 1\mu\text{m}$ and (b) $300\text{nm} \times 300\text{nm}$, and (c) a high resolution image of $100\text{nm} \times 100\text{nm}$ which is the zoomed scan of the square mark on (b). The high resolution image (c) clearly shows rectangular-shaped islands on the topmost Fe film. (d) MFM reveals multi-domain structures with well-ordered ripples, which were

formed from the bottom thick Fe film but not influenced by MgO and the topmost Fe films..... 110

Figure 7.1 Overview of how spin-polarized STM works on a topographically layered antiferromagnetic sample such as chromium by using the difference between spin polarized and non-polarized tips. With a non-magnetic, non-polarized tip, the height of each single step would be identical (in the case of chromium, height of 1.4 Å) since the tip does not distinguish between the alternating antiferromagnetic alignment of all the layers. However, with a spin-polarized tip, the tunneling current is modulated by the spin orientation between the probe and surface, so that terrace with favorable (parallel) spin orientation appears closer than those that are antiparallel. This difference in the tunneling current induces a vertical shift as an imposed feedback loop in order to maintain the set current while scanning. 114

Figure 7.2 Simplified Stoner ferromagnet model for spin-polarized tunneling: the tunneling current is proportional to the product of the density of states (DOS) of a tip and sample for each spin. When the tip and sample have same magnetization, the tunneling current is represented as $\rho_T^\uparrow(E) \rho_S^\uparrow(E) + \rho_T^\downarrow(E) \rho_S^\downarrow(E)$ and induces large amounts based on the product of both high densities. By contrast, when tip and sample are magnetized oppositely, the tunneling current is $\rho_T^\uparrow(E) \rho_S^\downarrow(E) + \rho_T^\downarrow(E) \rho_S^\uparrow(E)$, in which both terms are small because of the product of high and low densities. (ρ_T (or ρ_S) is the density of electron states (DOS) of the tip (or sample).) 117

Figure 7.3 Secondary electron microscopy (SEM) images of e-beam heated and Fe-coated STM tip..... 118

Figure 7.4 Evolution of chromium crystal surface with cleaning preparation: AFM images at various stages of repeated cycles of sputtering and annealing. (a) Initial state before any cleaning, measured using AFM in ambient condition. (b) UHV measurement after one cycle of sputtering (1.2 keV) and annealing, (c) after 2 additional cycles of sputtering and high temperature annealing (600 °C), and (d) after a total of 10 cycles at various combinations of annealing temperature, duration, and sputtering power. (e) high resolution image of (d), (f) after additional cleaning with high energy (2 keV) sputtering for 7 hours at room temperature, followed by rapid annealing (~ 10 min) at 600 °C. 120

Figure 7.5 Composition of topography and local conductance of a clean Cr surface. The following images were taken after 20 cycles of sputtering and annealing to remove oxides, including the native oxide and bulk segregated types. Left panel: STM topographic images on a clean Cr (001) surface, measured on the same sample with increasing resolution. Right pane: the corresponding local conductance images, which were taken at the bias voltage of (a) -100 mV, (b) -200 mV and (c) -100 mV. 123

Figure 7.6 Atomically resolved STM images of nitrogen reconstructions on a cleaned chromium. (a) The topography on 200 nm by 200 nm area shows relatively flat areas between steps. High resolution images on a top flat terrace ((b),(c)) and on wide steps ((d),(e)) show the atomic corrugations with two different phases. The nitrogen, which has migrated from the bulk, takes the interstitial sites at the surface and induces two kinds of reconstructed structure. The corresponding models are suggested in the middle of the figure, which are the p(1x1) and c(2x2) phases. 126

Figure 7.7 STM/STS measurement on Cr(001) shows the nitrogen contamination with p(1x1) and c(2x2) phases. (a) STM topography and dI/dU map at (b) 100 mV and (c) -100 mV bias voltage, which reveals a clear contrast difference on nitrogen reconstruction area. Graphs below show the full STS data on (d) Cr surface, (e) step edges and N-induced c(2x2) state, and (f) p(1x1) state..... 127

Figure 7.8 Low energy electron diffraction (LEED) measurement, as the function of the annealing temperature and duration. The LEED images were taken at the energy of 209 eV and recorded by using CCD camera. (a) At the temperature up to 350 °C, LEED showed a clear pattern, while in image (b) it has some additional spots at higher temperature of 450 °C. In addition, (c) the flash heating induced a much clearer pattern being diffused by longer heating, as shown in (d). Thus, the best annealing condition based on LEED measurement was the flash heating at 350 °C. 130

Figure 7.9 (a)~(c) STM images with different scan size on a cleaned Cr surface, which show no nitrogen reconstruction and less sputtering damages. These were obtained by low energy (600-800 eV) sputtering with subsequent annealing at 350 °C, after the amount of residual contamination was reduced by more than 10 additional cycles of cleaning. (d) Topography and the corresponding dI/dV maps taken at the bias voltage of -200 mV and 100 mV. (e) After additional annealing to 600 °C for 15 min, the STM showed a well-prepared surface with clear LEED pattern..... 133

Figure 7.10 Spin-polarized STM measurement on antiferromagnetic Cr (001): Topographic images (first column) and corresponding dI/dV maps at -250 mV bias

voltage (second column: row data, third column: filtered). The cross sections on rectangular segments are plotted on the first row. 134

Figure 7.11 Changes of MFM images by annealing temperature of (a) 200 °C, (b) 300 °C, (c) 450 °C, and (d) 650 °C. 138

Figure 7.12 MFM and SP-STM measurements on a 200 nm thick Permalloy film. (a) MFM image shows out-of-plane stripe domain structures with the width of around 300 nm. (b) STM images on a cleaned permalloy film and (c)~(d) its simultaneous measurements of conductance at the bias voltage of 400 mV (forward scan mode) and -400 mV (backward scan mode), respectively. At the bias voltage of 400 mV (in case of (c)), slight contrast changes with stripe pattern are found while no contrast difference is apparent at the bias voltage of -400mV (in case of (d)). This weak pattern is better distinct in the cross section of the rectangle presented in the image (c). In (d), the cross section graph shows the periodicity of around 300 nm width, which is compatible with the MFM measurement. 139

Figure 8.1 Examples of sample structures employing the CoFeB/MgO/CoFeB magnetic tunneling junction. The pseudo-spin-valve magnetic tunnel junction structure of (a) has produced a TMR of 604% at room temperature [88], and the sample structure of (b) was used for generating high-power microwave as reported in 2008 [89]. 144

Figure A.1 Pictures with front view and top view of the existing Omicron UHV system. It consists of the analysis chamber and preparation chamber, which are interconnected by a gate valve. The analysis chamber has various in-situ diagnosis

tools involving LEED, AES, AFM/MFM, and STM/STS, and the preparation chamber has equipped with two e-beam evaporators, an Ar-sputtering gun and a heating stage..... 146

Figure A. 2 The upgraded preparation chamber with additional fabrication capabilities. Three sputtering guns with source materials of CoFe, CoFeB and PtMn are now attached in the right-handed side of the chamber, and one triple e-beam evaporator and two single e-beam evaporators are in the left-handed side with source materials of MgO, Ru, Ta, Mg and Fe, respectively..... 147

Figure B. 1 Design and implementation of a new sample holder for the fast-entry lock (FEL) in the UHV system to increase the sample throughput. The new design consists of two identical holders, making it possible to transfer two samples into and out of the chamber at each FEL-pumping, while the original part had only one holder. Figures show (a) 3-D rendering of ProE design, (b) the fabrication and implementation in the system, and its machine drawing of (c) left and (d) right parts..... 149

Figure B.3 Design and modification of a sample plate: (a) machine drawing, (b) 3-D rendering and (c) its implementation. A large plate (2 inch by 1 inch) is placed on top of a conventional sample plate for increasing sample throughput..... 152

Figure B. 4 3-D rendering of the shutter in the preparation chamber, designed for the case of two additional sputtering guns. It would be attached to the front-top side of the preparation chamber because it is the only available flange. The shutter has a peanut shape and it rotates circularly along the center axis of the flange, which is angled 45 ° vertically. 153

| | |
|---|-----|
| Figure C.1 SEM images of CNTs grown on silicon oxide substrates by evaporating Fe nanoparticles in UHV..... | 155 |
| Figure C. 2 SEM images of CNTs on quartz substrates, which were grown by using a diluted ferritin solution..... | 156 |
| Figure C. 3 SEM images of CNTs on quartz by evaporating Fe-catalyst onto the sample, which was pre-covered by a metal shadow mask. | 156 |
| Figure C. 4 SEM images of CNTs on quartz substrates, which was pre-patterned by photo-lithography prior to the deposition of Fe and then lifted off. | 157 |

Chapter 1

Introduction

Magnetic information storage technology has evolved significantly during the past two decades with the exploitation of the ‘spin’ degree of freedom. Magnetoelectronics, or “spintronics”, has emerged as a thriving commercial industry offering products ranging from ultra sensitive sensors, magnetoresistive random access memories (MRAM), and disk read-write head for hard disk. These new generation micro/nano devices are designed using the quantum mechanical principles revealed by two important discoveries: the demonstration of giant magnetoresistance (GMR) effect in 1988 [1] and the large tunneling magnetoresistance (TMR) effect in 1995 [2, 3].¹ The critical feature of these effects is that they allow the electrical resistance across a junction comprised of magnetic and non-magnetic multilayers to be controlled by the application of an external magnetic field. This enables the storage of information in the form of a binary bit as either a high or low resistance state.

While similar in many respects, TMR and GMR effects differ in their constituent elements. TMR is observed on magnetic tunneling junctions (MTJs) consisting of two ferromagnetic films separated by a very thin insulating layer. GMR, on the other hand, uses a multilayer structure with non-magnetic metal spacers in the

¹ Indeed, these contributions are so vital that Albert Fert and Peter Grünberg were awarded the 2007 Nobel Prize in Physics for the discovery of GMR.

place of the insulator. Because TMR relies on tunneling, it is intrinsically high impedance, which leads to high magnetoresistance, reduced inelastic scattering, and well-controlled spin-polarization. The rapid progress in thin film fabrication technology and further miniaturization has increased the importance of TMR, which is displacing GMR in many applications.

There have been several transformative breakthroughs in the evolution of TMR. The concept of TMR was first proposed in 1975 by M. Julliere [4], who reasoned that the current from a ferromagnetic electrode to another through an insulating barrier is comprised by two independent parallel channels corresponding to spin-up and spin-down electrons. Julliere demonstrated the TMR up to 14% on a Co/oxidized Ge/Fe structure at 4.2K. While the concept was simple, it took 20 years to demonstrate the effect in room temperature and in technologically applicable configurations. In 1995, the development of a fabrication process that formed an amorphous aluminum oxide (Al_2O_3) insulating barrier without pin-hole defects allowed for a practical demonstration of Julliere's theory. Researchers T. Miyazaki and N. Tezuka reported about 18 % TMR at room temperature [2]. Further progress in fabrication allowed better quality films to be made with sharp interfaces and precise control of thickness (in the range of 1-2 nm). These lead to the increase of TMR up to 70% [5]. A disruptive technology was introduced in 2004, when a discontinuous jump in TMR of up to 180 % was achieved on a Fe/MgO/Fe (001) structure at room temperature [6, 7]. Compared with the amorphous Al_2O_3 layer, the magnetic Fe electrodes formed epitaxial layers with the crystalline magnesium oxide (MgO) barrier, and thus induced spin-coherent tunneling. In this new format, the

wavefunctions of the tunneling electrons are matched across the interface so their Bloch states are preserved through the whole tunneling process. In addition to conserving the spin state, MgO barrier also exhibits spin-filtering by having different decay rates in each of the Bloch states. Based on these properties, TMR of several orders of magnitude have been theoretically predicted on the Fe/MgO/Fe (001) system [8]. Recently, TMR up to 500 % was found at room temperature in CoFeB/MgO/CoFeB system [9]. While impressive, the reports on actual devices have fallen short of predictions.

This thesis examines the Fe/MgO/Fe (001) epitaxial system during sample growth, and measured topographic, electronic and magnetic properties at the atomic length scales, using the cleanest possible conditions to understand the difference between the theoretical prediction and experimental realities. Even though MgO-based MTJs have been actively investigated, this work is unique because most previous research has focused on macroscopic measurements on large structures and on the development of fabrication. The aim of this research, thus, is to augment our knowledge at the atomic level. To this end, the research focuses on the interplay between morphology, stoichiometry, and local magnetism, using a multifaceted approach involving atomic/magnetic force microscopy (AFM/MFM), scanning tunneling microscopy (STM), scanning tunneling spectroscopy (STS), Auger electron spectroscopy, and low energy electron diffraction (LEED), all operating under an ultra-high vacuum. The goal in this thesis was to provide an explanation for the discrepancy between the predicted TMR (>1000%) and the observation (<200 %), a longstanding obstacle to achieving high TMR in device applications. Apart from the

Fe/MgO/Fe work, this research also demonstrated the feasibility of spin-polarized tunneling from a ferromagnetic surface and a ferromagnetic coated STM tip, using a single crystal Cr (001) system known to have antiferromagnetically coupled adjacent planes.

The thesis is divided into seven chapters. Chapter 2 reviews the spin dependent tunneling, which is the basic concept for understanding the TMR effect. Specifically, the chapter covers Julliere, Stearns and Slonczewski's theoretical models based on free tunneling electrons, and then provides overviews of the density functional theory now widely used for calculating the structural, electronic, and magnetic properties of materials. Chapter 3 is specifically geared to the TMR calculation of Fe/MgO/Fe (001) system, the theoretical basis of the TMR effect in MgO-based MTJs. It will provide an overview of the calculation of Butler *et al.*, by summarizing their procedures and results in achieving the predicted value of TMR. Chapter 4 outlines the basic concepts and operating principles of AFM, MFM, STM, STS, the main diagnostic tools used throughout this work.

The subsequent chapters focus on the core experimental results of the research presented here. Chapter 5 covers experiments on the epitaxial growth of Fe on MgO (001) and its magnetic configuration as a function of thickness and deposition temperature. This chapter demonstrates how morphology depends on growth conditions, as well as how the magnetic structures vary from complex patterns in thin film to well-ordered magnetic ripples and domain walls in thick film.

Chapter 6 describes the surface morphology and stoichiometry of Fe film grown on an MgO (001) substrate, the MgO layer on the thick Fe film, and the

Fe/MgO/Fe multilayered structure. By directly comparing topography with the spatially localized surface density of states, the present research found that the surface is electronically inhomogeneous. This chapter discusses the manner in which electronic states evolve as a function of thickness of MgO layer, from submonolayer coverage, in which the overlayer acts as a small perturbation, to the underlying status of very thick coverage (> 1 nm), in which a clear bulk-like bandgap of MgO emerges. The observations presented here suggest the possible existence of an interfacial layer between Fe and MgO. Indeed, the electronic inhomogeneity and the interfacial layer may be responsible for the diminished TMR in real systems.

Finally, Chapter 7 demonstrates the implementation of spin-polarized STM (SPSTM) on a chromium single crystal. The operating principle of SPSTM is very similar to TMR. Details of the morphological evolution of Cr (001) are presented by the series of AFM/STM images at various stages. Repeated cycles of sputtering and annealing show the influence of oxygen and nitrogen on the migration of these species from the bulk to the surface. On a clean surface, the alternating contrasts on adjacent layers are revealed on spin-polarized tunneling, which corresponds to the topological antiferromagnetism of the Cr (001) single crystal.

Chapter 2

Theoretical Modeling for Spin Dependent Tunneling

2.1 Introduction

The tunneling magnetoresistance (TMR) effect is the primary enabler of vitally important technological advances such as plentiful and cheap data storage, non-volatile random access memories, and ultra-sensitive magnetic field sensors in our transportation system. TMR is used in devices known as magnetic tunnel junctions (MTJs), which are comprised, in their basic form, of ferromagnetic metals separated by a thin insulating layer. The current through the magnetic tunnel junction changes significantly depending on the relative magnetic orientations of the two ferromagnetic electrodes. Since the magnetization of these electrodes can be oriented by an external magnetic field, the total electrical resistance can be controlled by the application of an external magnetic field. This phenomenon is called TMR.

The spin states of electrons are unimportant in determining the properties of non-magnetic materials. Because the density of states of spin-up and spin-down states are equivalent, the contribution of each spin is negligible on the transport properties, except for a multiplicative factor of two. In magnetic materials, however, the density of the electronic states of each spin is different, or spin-polarized, leading to different contributions on the material properties, such as electrical conductivity and heat

capacity [10, 11]. In the case of a tunneling junction, the tunneling probability can be expressed as a function of the relative orientation of the spin states. To make the approach simpler, one can usually assume that an electron can only interact if they have the same spin orientation, combining to form their own independent conducting channel. This assumption is valid provided that the spin is conserved during the tunneling and the effects of spin-orbit coupling and spin-flipping can be ignored.

Spin dependent tunneling (SDT) is the premise for understanding TMR. A simple model was suggested by M. Julliere in 1975 [4], in which he proposed that the spin polarization of the tunneling current can be explained in terms of the amount of spin-up and -down electrons existing in the ferromagnetic electrodes. While the Julliere model was quite useful in interpreting early experiments, it was too simple to be applied to all the available data obtained subsequently, which were sometimes at odds with the experimental results. Thus, Stearns [12] and Slonczewski [13] modified the model to make take into account the new data. Nevertheless, though Stearns and Slonczewski's approaches are helpful in understanding the concept of SDT intuitively, they rely on a simple free electron model, which does not consider actual atomic structures and their effects on tunneling. Thus, these models were incapable of predicting the influence of the spin-dependent electronic bands. Predicting these influences required more sophisticated approaches, such as the density functional theory, which takes into account the influence of the structural and electronic properties of the entire junction, including the ferromagnetic metal, the insulator, and their interfaces.

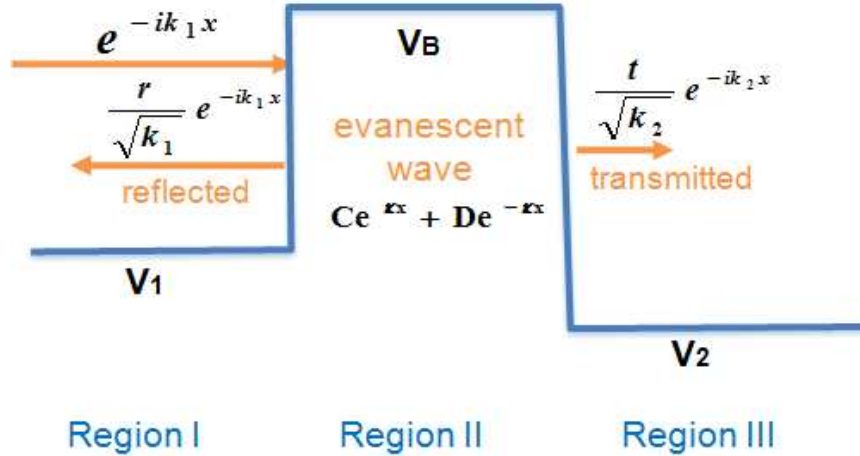


Figure 2.1 A simple tunneling problem with a rectangular potential barrier: An electron moves from the left to right side, passing through the potential barrier (V_B). Their wavefunctions can be obtained by solving time-invariant Schrödinger equation.

2.2 Free Electron Models

An exploration of this phenomenon must begin by studying the elementary model of tunneling of free electrons. Later, this chapter will examine free electron models as applied to magnetism by Julliere, Stearns, and Slonczeski [14, 15]

2.2.1 Simple tunneling problem

The simplest tunneling is a one dimensional case, shown schematically in figure 2.1. A free electron is incident on a rectangular potential barrier and traveling into three regions with potentials V_1 , V_B , and V_2 , respectively. The electron has the total energy, E , which satisfies the conditions of $V_1 < E$, $V_2 < E$, and $E < V_B$. The wavefunction of the electron can be obtained by solving the time-independent Schrödinger equation,

$$-\frac{\hbar^2}{2m}\nabla^2\Psi + V(x)\Psi = E\Psi \quad (2.1)$$

where Ψ is the electronic wavefunction, m is the electron mass, d is the width of the barrier, \hbar is Planck's constant, E is the energy of the tunneling electron, and V is the potential energy in each region. Assuming that the energy E and the transverse component of momentum k_{\parallel} are conserved during the tunneling (called ballistic transport), the electron moves coherently without any inelastic scattering and the wavefunction in each region can be expressed as,

$$\begin{aligned} \Psi &= \frac{\exp(ik_1x) + r \exp(-ik_1x)}{\sqrt{k_1}} && \text{in region I} \\ &= C \exp(\kappa x) + D \exp(-\kappa x) && \text{in region II} \\ &= \frac{t \exp(ik_2x)}{\sqrt{k_2}} && \text{in region III} \end{aligned} \quad (2.2)$$

$$\text{where } k_1 = \sqrt{\frac{2m(E - V_1 - k_{\parallel}^2)}{\hbar^2}}, \quad k_2 = \sqrt{\frac{2m(E - V_2 - k_{\parallel}^2)}{\hbar^2}}, \quad \kappa = \sqrt{\frac{2m(V_B - E + k_{\parallel}^2)}{\hbar^2}}$$

The coefficients can be approximated by matching the boundary conditions, i.e., the continuity of the wavefunction Ψ and its first derivative at boundary. Using these, it can easily be shown that the transmission coefficient is given by:

$$T(k_{\parallel}) = |t|^2 = \frac{16k_1k_2\kappa^2 \exp(2d\kappa)}{\{\kappa(k_1 + k_2)[1 + \exp(2d\kappa)]\}^2 + \{(\kappa^2 - k_1k_2)[1 - \exp(2d\kappa)]\}^2} \quad (2.3)$$

For the most tunneling case, the transmission probability is very small compared to the reflection, which leads to the condition that $\exp(-2d\kappa) \ll 1$.

Therefore, the equation (2.3) can be simplified to:

$$T(k_{\parallel}) \approx \frac{16k_1k_2\kappa^2 \exp(-2d\kappa)}{[\kappa(k_1 + k_2)]^2 + [(\kappa^2 - k_1k_2)]^2} = \frac{4k_1\kappa}{k_1^2 + \kappa^2} \frac{4k_2\kappa}{k_2^2 + \kappa^2} \exp(-2d\kappa) \quad (2.4)$$

This equation can be extended to spin dependent tunneling by considering into two spin channels. Depending on the spin state, the tunneling electron undergoes different potential in electrodes. Thus, the potential in the i -th electrode ($i=1$ or 2) can be changed into V_i^\uparrow or V_i^\downarrow , and the corresponding wavevector k_i also changes to k_i^\uparrow or k_i^\downarrow . When two electrodes are the same ferromagnetic metals and they are magnetized in the parallel direction, the tunneling by spin-up electrons can be represented in the equation (2.4) by replacing $k_1=k_2=k^\uparrow$; the tunneling by spin-down electrons can be done by doing $k_1=k_2=k^\downarrow$. Therefore, the total conductance, for the parallel magnetic alignment of two same ferromagnetic electrodes, can be predicted as the summation of these two cases:

$$T_P \approx \left[\left(\frac{4k^\uparrow \kappa}{k^{\uparrow 2} + \kappa^2} \right)^2 + \left(\frac{4k^\downarrow \kappa}{k^{\downarrow 2} + \kappa^2} \right)^2 \right] \exp(-2d\kappa) \quad (2.5)$$

On the other hand, when the same electrodes are magnetized in the opposite direction, the tunneling of each channel can be obtained by changing k_1 and k_2 into k^\uparrow and k^\downarrow in the equation (2.4), and the conductance for the anti-parallel alignment can be calculated as:

$$T_{AP} \approx 2 \times \frac{4k^\uparrow \kappa}{k^{\uparrow 2} + \kappa^2} \frac{4k^\downarrow \kappa}{k^{\downarrow 2} + \kappa^2} \exp(-2d\kappa) \quad (2.6)$$

$$\text{TMR is defined as } TMR \equiv \frac{R_{AP} - R_P}{R_P} = \frac{G_P - G_{AP}}{G_{AP}} \approx \frac{T_P - T_{AP}}{T_{AP}} \quad (2.7)$$

If it is non-polarized, i.e., $k^\uparrow=k^\downarrow=k$, the tunneling conductance between parallel and anti-parallel alignment will be equivalent ($T_P=T_{AP}$), which leads to the TMR value of 0%. On the other hand, if it is 100% polarized, i.e., when the electrode has only one spin electron, there will be no component for minority spin ($k^\downarrow=0$), so that T_{AP}

vanishes. Thus, if we can make an ideal half metal and use it as electrode, it can induce the infinite value of TMR.

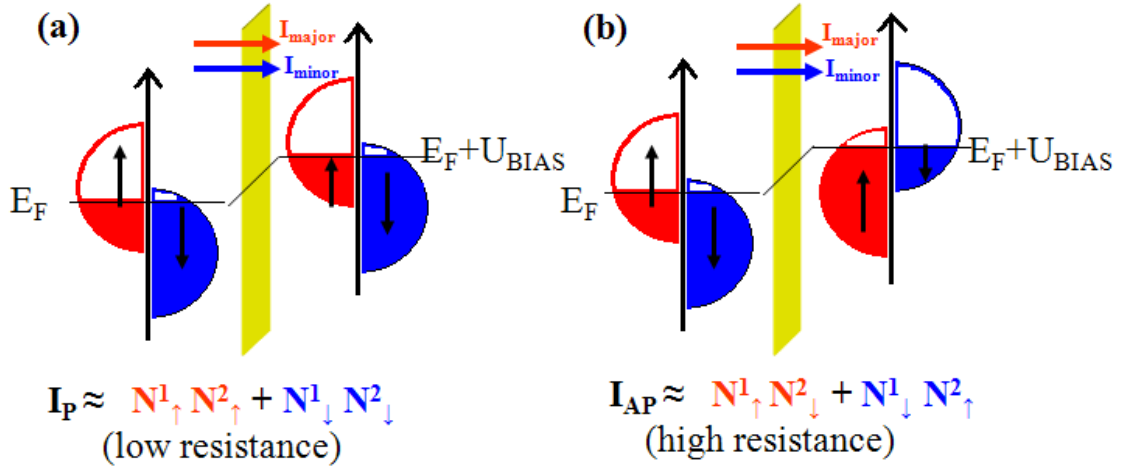


Figure 2.2 Julliere's model: the tunneling current is proportional to the products of DOS for each spin in two electrodes. (a) When two ferromagnetic electrodes are magnetized in the same direction (parallel alignment), the current can be proportional to $N_1^\uparrow N_2^\uparrow + N_1^\downarrow N_2^\downarrow$, where $N_i^{\uparrow(\downarrow)}$ is the number of spin-up (down) electrons at Fermi level in the i -th electrode. Similarly, (b) when two electrodes are magnetized in the opposite direction (anti-parallel alignment), the tunneling current is proportional to $N_1^\uparrow N_2^\downarrow + N_1^\downarrow N_2^\uparrow$.

2.2.2 Julliere model

A simple but very intuitive model was proposed in 1975 by Julliere [4] in order to explain spin-dependent tunneling (SDT). While purely classical, it nevertheless explained some essential features of SDT. The later refinements of Slonczewski took into consideration the quantum mechanical aspects of the problem and explained some of the subtleties of the effect. The Julliere model starts with two assumptions. First, the electron's spin is conserved during a tunneling process. Second, the tunneling probability for a particular spin orientation is proportional to the product of the amounts of the electrons with the spin state in each electrode. In other words, the tunneling processes for spin-up or -down electrons are independent, and each current can be represented in terms of the density of states (DOS) for majority or minority spin at the Fermi level in each electrode. In the case of parallel alignment, the majority (or minority) spin direction in one electrode is the majority (or minority) in the other, while in the case of anti-parallel alignment the majority spin in one electrode is the minority in the other. Therefore, based on these assumptions, the conductance for the parallel and anti-parallel magnetic alignments (G_P and G_{AP}) of two ferromagnetic electrodes can be described as:

$$\begin{aligned} G_P &\propto \rho_1^\uparrow \rho_2^\uparrow + \rho_1^\downarrow \rho_2^\downarrow \\ G_{AP} &\propto \rho_1^\uparrow \rho_2^\downarrow + \rho_1^\downarrow \rho_2^\uparrow \end{aligned} \quad (2.8)$$

where $\rho_{1(or 2)}^\uparrow$ and $\rho_{1(or 2)}^\downarrow$ are the DOS of spin-up and -down electrons at the Fermi level in the electrode 1(or 2). While his suggestion appeared ad hoc, it is nevertheless intuitive, and the idea is valid even under the modern approach based on Bardeen's tunneling theory. With the added assumption that the tunneling matrix is independent

of the energy, and in the limit of small bias voltage applied across the junction, the tunneling conductance can be expressed as being linearly proportional to the density of states of each electrode at Fermi level [16]. The details will be shown in chapter 4.

When we define the polarization of the each electrode as:

$$P_i = \frac{\rho_i^\uparrow - \rho_i^\downarrow}{\rho_i^\uparrow + \rho_i^\downarrow}, \quad \text{where } i=1, 2 \quad (2.9)$$

then the TMR, corresponding to the relative difference of the tunneling conductance between parallel (P) and anti-parallel (AP) alignments of two electrodes, can be expressed using equations (2.5) and (2.6) as,

$$TMR \equiv \frac{R_{AP} - R_P}{R_P} = \frac{G_P - G_{AP}}{G_{AP}} = \frac{2P_1P_2}{1 - P_1P_2} \quad (2.10)$$

This model ascribes the TMR as an intrinsic property of the ferromagnetic materials, and it can be calculated simply by knowing the polarization of each electrode. However, this did not always agree with some experimental results. Indeed, the polarization values of various ferromagnetic metals, which were measured directly by Tedrow and Merservey [17] on a ferromagnet-insulator (alumina)-superconductor (aluminum) junction, sometimes contradicted the calculated predictions based on its DOS at Fermi level, as defined in equation (2.9). In particular, for Ni and Co materials, the calculation of electronic structures shows that the DOS for the minority spin is always higher than for the majority spin, which results in a negative value of the polarization. However, the measured value is always positive.

To fix this inconsistency, Stearns modified the definition of the polarization by considering the effective mass of electrons. He pointed out that in Julliere's model

all electrons contributed to the conductance equally, while in reality, electrons tunnel through a barrier with different momentum and different decay rates. More to the point, Sterns included the effect of the curvature of energy bands since the effective mass is $\frac{1}{m^*} = \frac{1}{\hbar} \frac{\partial^2 E}{\partial k^2}$. For example, localized d-electrons decay very quickly, while dispersive s-like electrons with a small effective mass decay slowly. Therefore, Sterns suggested considering the conductance from dispersive bands only, which are dominant in most tunneling processes. Thus, the polarization of the electrode needs to be modified by using the Fermi wavevector of the itinerant electrons rather than the total DOS.

$$P_i = \frac{k_i^\uparrow - k_i^\downarrow}{k_i^\uparrow + k_i^\downarrow}, \quad \text{where } i=1, 2 \quad (2.11)$$

Here, k^\uparrow and k^\downarrow are the Fermi wavevectors of the dispersive bands for the spin-up and -down electrons. This model can explain the inconsistency between Julliere's model and Tedrow and Merservey's experiment on the polarization of Co and Ni materials. In case of Ni, for example, majority spin electrons have a dominant dispersive band at the Fermi level, while the minority spin electrons have several kinds of bands. Thus, even though the total DOS of minority spin is higher than that of majority spin, the contribution from the dispersive band of majority spin can be more dominant on tunneling than those from any other bands of minority spin, which can induce the positive polarization value, as measured in the experiment [17].

In summary, the models of Julliere and Stern consider the TMR as the intrinsic property of the ferromagnetic electrodes. While these models were useful interpreting the early experimental data on SDT, their models did not consider the

fact that the tunneling process can be affected by the electronic structures of the insulator as well. In fact, including the electronic states of the barrier is the key to achieving very high TMR values.

2.2.3 Slonczewski model

In 1989, Slonczewski suggested the first accurate theoretical model for TMR in the limit of a thick barrier. He used a simple free-electron tunneling model with a rectangular potential barrier, in which the transmission probability through the junction can be expressed in the form of equation (2.4). If one looks at the equation carefully, it can be interpreted as the combinations of the transmission probability across the left and right interface of the electrode-barrier, with the exponential decay in the barrier.

$$T(k_{\parallel}) = \frac{4k_1\kappa}{k_1^2 + \kappa^2} \frac{4k_2\kappa}{k_2^2 + \kappa^2} \exp(-2d\kappa)$$

$$\rightarrow T_{\mathbf{B}}(\mathbf{k}_{\parallel}) = T_L(\mathbf{k}_{\parallel})T_R(\mathbf{k}_{\parallel}) \exp(-2\kappa d) \quad (2.12)$$

Here the transmission probability at each interface is defined as: $T_i = \frac{4k_i\kappa}{k_i^2 + \kappa^2}$.

When the barrier is thick enough, the tunneling is dominant at $k_{\parallel} = 0$. Thus, by ignoring any transverse component ($k_{\parallel} \neq 0$), the decay factor can be simplified as:

$$\kappa = \sqrt{\frac{2m(V_B - E_F + k_{\parallel}^2)}{\hbar^2}} \rightarrow \kappa_0 = \sqrt{\frac{2m(V_B - E_F)}{\hbar^2}} \quad (2.13)$$

and the transmission probability is changed to:

$$T_{\mathbf{B}}(\mathbf{k}_{\parallel}) = T_L(\mathbf{k}_{\parallel})T_R(\mathbf{k}_{\parallel})\exp(-2\kappa_0 d), \text{ with } T_i = \frac{4k_i\kappa_0}{k_i^2 + \kappa_0^2} \quad (2.12a)$$

Based on these expressions, Slonczewski interpreted that the spin polarization comes from the difference in transmission probability between the majority and minority spins at the interface, not from the DOS or the wavevector of electrons in the electrode. Therefore, he modified the definition of the polarization by replacing the DOS in equation (2.6) with the transmission probability, T_i , at the interface. Then, the effective polarization can be defined as:

$$P_i^{eff} \equiv \frac{T_i^{\uparrow} - T_i^{\downarrow}}{T_i^{\uparrow} + T_i^{\downarrow}} = \frac{(k_i^{\uparrow} - k_i^{\downarrow})(\kappa_0^2 - k_i^{\uparrow}k_i^{\downarrow})}{(k_i^{\uparrow} + k_i^{\downarrow})(\kappa_0^2 + k_i^{\uparrow}k_i^{\downarrow})} = P_i \frac{(\kappa_0^2 - k_i^{\uparrow}k_i^{\downarrow})}{(\kappa_0^2 + k_i^{\uparrow}k_i^{\downarrow})} \quad (2.14)$$

In addition, Stearns generalized the tunneling conductance as a linear function of the cosine angle θ when the magnetic moments of two ferromagnetic electrodes are oriented not simply parallel or anti-parallel, but with any angle θ , which implied an interfacial exchange coupling between the ferromagnets.

$$G(\theta) = G_0(1 + P_1^{eff} P_2^{eff} \cos(\theta)) \quad (2.15)$$

In the special cases, when the angle θ is 0° (in-phase) or 180° (out-of-phase), the conductance for parallel and anti-parallel alignment can be described as:

$$\begin{aligned} G_P &= G_0(1 + P_1^{eff} P_2^{eff}) \\ G_{AP} &= G_0(1 - P_1^{eff} P_2^{eff}) \end{aligned} \quad (2.16)$$

The TMR is expressed as same as equation (2.7), except using P^{eff} instead P .

$$TMR \equiv \frac{G_P - G_{AP}}{G_{AP}} = \frac{2P_1^{eff} P_2^{eff}}{1 - P_1^{eff} P_2^{err}} \quad (2.17)$$

In summary, the main difference in the Julliere and Slonczewski models lies in the definition of ‘polarization’. Unlike in Julliere’s model, Slonczewski’s model

identified the origin of the TMR in the properties of the coupling between the insulator and the ferromagnetic metal.

2.3 Density Functional Theory

With the success of the Slonczewski model in showing the key role of the interfaces, it became necessary to utilize more sophisticated tools to model the band structures for all materials in the structure. A very popular method is density functional theory.

2.3.1 Types of first principle methods

The first principle methods, or *ab initio*, are computational methods based on quantum mechanics/chemistry. These principles do not use any experimental data, and begin with the definition of the Hamiltonian of the system. Within the Born-Oppenheimer approximation, such that the nuclei are assumed to be static compared to electrons, the first principle methods use the exact expression of the Hamiltonian, but have the approximation of the wavefunction. The semi-empirical methods, on the other hand, approximate both the wavefunction and the Hamiltonian.

Computational Approaches

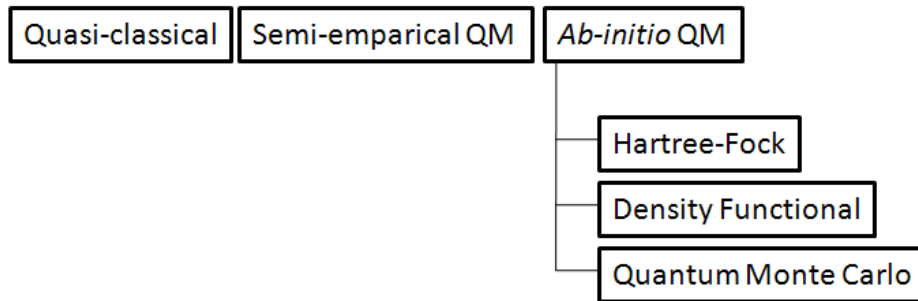


Figure 2.3 A classification of modern computational methods, which are widely used for calculating electronic structures of various systems. In particular, *ab initio*, or called first principle method, consists of three different approaches, Hartree-Fock (and post Hartree-Fock), density functional theory, and quantum Monte Carlo simulation. These three methods are alternatively used depending on the system.

The simplest of the first principle methods is the Hartree-Fock approach. It assumes that the many-electron wavefunction can be represented as the product of a set of single-electron wavefunctions. By using the variational principle, all parameters can be decided as the value that can be found by minimizing the total energy and the ground state of the system. The one of weakness of this approach is that it considers only the electron-exchange, not the electron-correlation. Neglecting the electron-correlation often leads to large discrepancy in experimental results. To include the correlation, several modifications have been suggested, called ‘post Hartree-Fock’ or ‘beyond Hartree-Fock’ methods. Among the post Hartree-Fock methods, the configuration interaction calculation and the Møller-Plesset perturbation theory [18] are widely used.

The density functional theory (DFT) is an alternative to the Hartree-Fock calculations. While the Hartree-Fock and post Hartree-Fock methods are expressed on the basis of the wavefunction, DFT uses electron density instead. The electron density is a real physical quantity and can be easily represented in three dimensions. I will attempt to explain the salient details of this approach in the following sections.

Lastly, the Quantum Monte Carlo method is a numerical simulation [19], which represents quantum many-electron effects on the wavefunction directly. Different from the Hartree-Fock method, it avoids the variational estimation and uses an explicitly corrected wavefunction whose integral can be numerically calculated by the Monte Carlo analysis algorithm. It is the most accurate method, but it comes at the expense of time, and requires high performance computing such as super-computing.

2.3.2 Principles of density functional theory

The density functional theory (DFT) was introduced in the 1960's [20, 21] and earned W. Kohn the Nobel Prize in 1998. The DFT is the most successful approach for computing the electronic structure of various materials, from atoms, molecules to solid, fluids and complex molecular systems [review articles: 22-24].

Ideally, if we solve the Schrödinger equation, we can define all physical properties of the system. However, in reality, in a multi-particle system, the calculation is very complicated and sometimes impossible within the limits of our current computing capabilities. Here it is important to consider the system consisting of M nuclei and N electrons. Even if one assumes that the heavier nuclei are

considered as being fixed in space (Born-Oppenheimer approximation), the time-independent, non-relativistic Schrödinger equation is expressed as:

$$\left\{ -\frac{\hbar^2}{2m} \sum_{i=1}^N \nabla_i^2 - \sum_{i=1}^N \sum_{l=1}^M \frac{Z_l e^2}{|\vec{r}_i - \vec{R}_l|} + \frac{1}{2} \sum_{i=1}^N \sum_{j>i}^N \frac{e^2}{|\vec{r}_i - \vec{r}_j|} \right\} \Psi = E\Psi \quad (2.18)$$

where \vec{r}_i is the positions of the i -the electrons, and \vec{R}_l, Z_l are the positions and atomic numbers of the l -the nuclei. The wavevector is the function of \vec{r}_i , i.e., $\Psi = \Psi(\vec{r}_1, \vec{r}_2, \vec{r}_3, \dots, \vec{r}_N)$, which in and at it very complicated.

The DFT is the alternative method for finding a good approximation of the solutions of the Schrödinger equation. Instead of using the wavevector Ψ directly, the DFT uses the electron density distribution $n(\vec{r})$, which can be defined as:

$$n(\vec{r}) = N \int \dots \int |\Psi(\vec{r}, \vec{r}_2, \vec{r}_3, \dots, \vec{r}_N)|^2 d\vec{r}_2 d\vec{r}_3 \dots d\vec{r}_N \quad (2.19)$$

This electron density distribution $n(\vec{r})$ vanishes at infinity and integrates to the total number of electrons N . It is proven that if the ground state of $n(\vec{r})$ is known, it can specify the external potential V_{ext} uniquely. That means that the physical system can be completely identified by $n(\vec{r})$ (the first Hohenberg-Kohn theorem). In addition, as the ground state energy E is determined when the trial wave functions $\tilde{\Psi}$ satisfy the Rayleigh-Ritz minimal condition $E = \min_{\tilde{\Psi}} (\tilde{\Psi}, H\tilde{\Psi})$, the ground energy E also can be obtained in terms of trial densities $\tilde{n}(\vec{r})$, satisfying the similar condition of $E = \min_{\tilde{n}(\vec{r})} E_v[\tilde{n}(\vec{r})]$ (the Hohenberg-Kohn minimum principle).

The next step in implementing the DFT is to reduce the intractable many-body Hamiltonian problem of interacting electrons into the non-interacting single-particle-like form by redefining the effective potential (this is called the self-consistent Kohn-Sham method). The Hamiltonian is the summations of the kinetic energy (T), the potential energy (V), and electron-electron interaction energy (U), as shown in equation (2.18).

$$\left\{ -\frac{\hbar^2}{2m} \sum_{i=1}^N \nabla_i^2 - \sum_{i=1}^N \sum_{l=1}^M \frac{Z_l e^2}{|\vec{r}_i - \vec{R}_l|} + \frac{1}{2} \sum_{i=1}^N \sum_{j>i}^N \frac{e^2}{|\vec{r}_i - \vec{r}_j|} \right\} \Psi = (T + V + U) \Psi = E \Psi \quad (2.18a)$$

When we express the energy $E_v[\tilde{n}(\vec{r})]$ in terms of the potential energy (V), non-interacting kinetic energy (T_s), classical Coulomb interaction (J), and unknown function E_{XC} , which contains the remaining parts, $E_v[\tilde{n}(\vec{r})]$ is shown as the following:

$$\begin{aligned} E_v[\tilde{n}(\vec{r})] &= \langle \Psi(\tilde{n}) | T + V + U | \Psi(\tilde{n}) \rangle \\ &= T_s + V + J + E_{XC} \quad (2.20) \\ &= T_s[\tilde{n}(\vec{r})] + \int \tilde{n}(\vec{r}) V(\vec{r}) d\vec{r} + \frac{1}{2} \int \frac{\tilde{n}(\vec{r}) \tilde{n}(\vec{r}')}{|\vec{r} - \vec{r}'|} d\vec{r} d\vec{r}' + E_{XC}[\tilde{n}(\vec{r})] \end{aligned}$$

Where E_{XC} is called the exchange-correlation energy and is defined as $E_{XC} = T - T_s + U - J$ mathematically. If we specify the effective potential V_{eff} with the last three terms in the equation, the Hamiltonian is simplified identically into the case of non-interacting particles moving under the effective potential.

$$V_{eff} = V(\vec{r}) + \int \frac{n(\vec{r}')}{|\vec{r} - \vec{r}'|} d\vec{r}' + v_{XC}(\vec{r}), \quad \text{where } v_{XC} \equiv \frac{\delta}{\delta \tilde{n}} E_{XC}[\tilde{n}(\vec{r})] |_{\tilde{n}=n(\vec{r})} \quad (2.21)$$

$$H \phi_j = \left\{ -\frac{1}{2} \nabla^2 + V_{eff}(\vec{r}) \right\} \phi_j = \varepsilon_j \phi_j \quad (2.22)$$

The multi-particle Hamiltonian equation changes to the single particle equation with the wavevector ϕ_j , and this equation is called the Kohn-Sham equation.

The major problem of DFT is to find the exchange-correlation energy E_{XC} , used so far as a mathematical term. If the exact exchange-correlation function is known, the system is solved exactly. However, because this function is too complicated to be expressed in a closed form (except for the free electron gas), the proper approximations must be used in order to reflect the electronic structures of the system. As previously noted, this function is from the difference of the Hamiltonian between the interacting many-electron system to the non-interacting single electron system. Thus, this term includes all the effects of exchange and correlation interactions, such as Pauli exclusion between electrons with same spin orientations, and the instantaneous reaction of electrons with opposite spins.

2.3.3 Exchange-correlation energy (E_{XC}) in density functional theory

The most widely used approximation for E_{XC} is the local-density approximation (LDA). The LDA is based on the homogeneous electron gas (HEG) model [22], in which electrons move on a positively distributed charge in the background while the total ensemble is neutral. The LDA assumes that the exchange-correlation energy at a position \vec{r} can be represented as the energy in an uncorrelated homogeneous electron gas, where the electronic density is found to be the same as the electron gas at position \vec{r} ,

$$E_{XC}^{LDA} \equiv \int e_{XC}(n(r))n(r)dr \quad (2.23)$$

where $e_{XC}(n)$ is the exchange-correlation energy density, the function of the density n in a uniform electron gas. This energy density is weighted with the probability $n(r)$, the probability that an electron can be found at this position. The quantity $e_{XC}(n)$ can be further split into two contributions, one from the exchange and the other from the correlation: i.e.,

$$e_{XC}(n(\vec{r})) = e_X(n(\vec{r})) + e_C(n(\vec{r})) \quad (2.24)$$

The exchange part, e_X , was originally derived by Bloch and Dirac and is defined as $e_X \equiv -\frac{3}{4} \left(\frac{3n(\vec{r})}{\pi} \right)^{1/3} = -\frac{0.458}{r_s}$, where r_s is given by $\frac{4\pi}{3} r_s^3 = \frac{1}{n}$. Even though the explicit expression is not known, the correlation part, e_C , can be estimated by several methods, firstly by E. P. Wigner (1938) as $e_C = -\frac{0.44}{r_s + 7.8}$, and recently, with a high accuracy, by using quantum Monte Carlo simulations of the homogeneous electron gas. There are many approaches from quantum Monte Carlo simulations, such as Vosko-Wilk-Nusair, Perdew-Zunger, Cole-Perdew, and Perdew-Wang codes.

The LDA can be extended to the local-spin-density approximation (LSDA) for spin-polarized systems [25]. By employing two spin densities, $n_\alpha(r)$ and $n_\beta(r)$, with the total electron density $n(r) = n_\alpha(r) + n_\beta(r)$, the exchange-correlation energy can be expressed as:

$$E_{XC}^{LSDA}(n_\alpha(r), n_\beta(r)) \equiv \int n(r) \cdot e_{XC}((n_\alpha(r), n_\beta(r))) dr \quad (2.25)$$

Here, the exchange energy density is the summation of the exchange energy density from two spin-unpolarized cases: i.e., $e_X = \frac{1}{2} \{e_X(2n_\alpha) + e_X(2n_\beta)\}$. The correlation energy density can be expressed as a function of the total density (n) and the spin

polarization (P), i.e., $e_C(n, P)$, where P is defined as $P = \frac{n_\alpha - n_\beta}{n_\alpha + n_\beta}$. Several

descriptions for the correlation have been suggested, as in the case of LDA.

Another intensively developed approximation is the generalized gradient approximation (GGA). GGA goes beyond LDA by including information not only about the density $n(r)$ but also about the gradient of the charge density $\nabla n(r)$, which takes into account the non-homogeneity of the true electron density.

2.3.4 Implementations of density functional theory

Depending on the system, a different approach has to be chosen to effectively represent the various properties of real materials, such as structural, mechanical, electronic, optical, and magnetic properties, etc. Even in the DFT calculation, the different approximation and the corresponding program codes need to be executed to acquire the best match with the experimental data, or the most realistic prediction. Figure 2.4 summarizes the implementations based on the DFT. The simulation results and the easiness of the calculation vary significantly, depending not only on the approximation of the exchange-correlation energy such as LDA and GGA, but also on whether one uses full potential or pseudo-potential technique, or whether one uses the basis in the form of plane or spherical waves.

Typical DFT Implementation

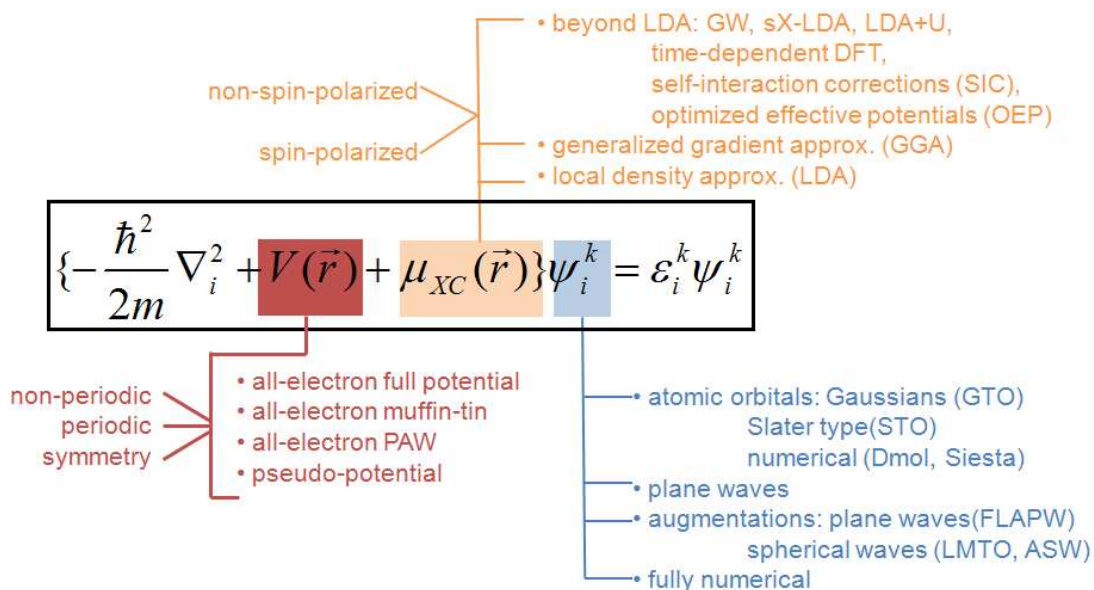


Figure 2.4 Implementation of the density functional theory (DFT) methods, with the lists of approximations applied on a Schrödinger equation.

Once the detailed methods are determined with proper potential energies, the calculations are iterated self-consistently, beginning with a trial electron density. The Hamiltonian is calculated using this electron density, and then diagonalized in order to get the eigenvalues and eigenvectors of the system. By using those values, a new electron density can be obtained. These cycles are repeated until the self-consistency is achieved such that the proper physical quantities can be computed.

Chapter 3

Theoretical Calculation for Fe/MgO/Fe (100) Epitaxial System

3.1 Introduction

Magnetic tunnel junctions (MTJs) employing a magnesium oxide barrier have come front and center in magnetic storage industry since the high TMR (up to 180 %) was observed at room temperature based on a Fe/MgO/Fe (001) system [6]. Compared with the aluminum oxide insulator, which is amorphous, MTJs with a magnesium oxide barrier have grown epitaxially into single-crystal structures. Consequently, the electronic properties of the MTJs, such as the tunneling conductance, depend on specific crystallographic directions, as the electrons encounter different periodic potentials depending upon the transport direction. Thus, the description of the tunneling phenomena in this case is beyond the free-electron model, and needs to take into account the actual atomic structures. Ideally, the Bloch states of these electrons are conserved during the entire tunneling process by coupling the wavefunctions at electrodes with those in an insulating layer.

There are two independent calculations that have been made for the TMR of a Fe/MgO/Fe (001) epitaxial system. One is based on Butler *et al.*'s first principle method [8], and the other is based on Mathon and Umerski's multiband tight binding

method [26]. Even though these methods are based on different assumptions, they arrive at very similar qualitative conclusions, and both have predicted extremely large TMR (more than 1000 %). According to Butler *et al.*, in the case of a large MgO barrier thickness, the large TMR comes from the spin filtering effects, such as different attenuation rates in the barrier and different emission/collection rates in the ferromagnetic electrodes with respect to the symmetry of the wavefunction. This chapter reviews the calculations made by Butler *et al.*, and elaborates on the procedures and results for the tunneling conductance on an Fe/MgO/Fe system [15].

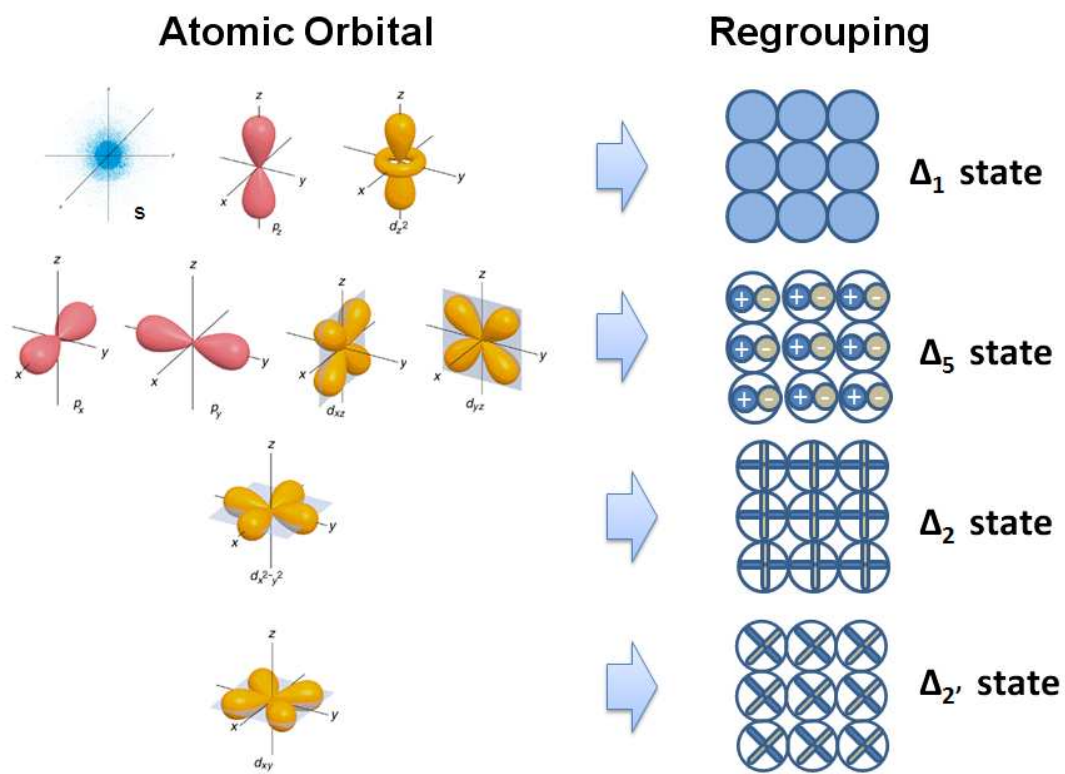


Figure 3.1 Regrouping atomic orbital into 4 symmetries (Δ_1 , Δ_5 , Δ_2 , and Δ_2') according to the symmetry criteria. The atomic orbital images were taken from the website: http://www.chem.ufl.edu/~itl/2045_s00/lectures/lec_10.html

3.2 Overview of Butler *et al.*'s first principle method

Butler *et al.* obtained the total tunneling conductance for parallel and anti-parallel alignments by calculating the transmission coefficients of the Bloch states for each majority and minority spin electron. An electron traveling in a single crystal can be represented by Bloch states, which are wavefunctions with the same periodicity as the crystal potential. In the coherent tunneling, these Bloch states are conserved by coupling with each other as having same symmetry at the electrode/insulator interfaces. By finding bulk Bloch eigenstates and matching wavefunctions, the transmission coefficient for each state can be obtained. The total conductance can then be induced by summarizing these coefficients according to the Landauer equation. Prior to the study on the actual calculation on a Fe/MgO/Fe structure, this chapter will explore the general role of symmetry in spin coherent tunneling, and briefly review principles and techniques such as the self-consistent layer KKR method, transmission matrices conversion, and the Landauer conductance formula.

3.2.1 The role of the symmetry in tunneling

The symmetry of the Bloch states has an important role in tunneling as it relates to the coupling of the electrode (Fe) and insulating barrier (MgO) wavefunctions. Unlike in the simple tunneling model, the atomic orbital or the atomic curvature affects the decay rate in a real system. For example, it is well known that electrons with s-like states decay slowly in an insulator, while p-like electrons decay quickly and d-like electrons even more quickly. Mathematically, tunneling can be represented as the wavefunction in the form of $\Psi(x, y, z) = \phi(x, y) \exp(-\kappa z)$, based on

the assumption that the structure consists of infinitely extended layers on the x-y plane and that the total energy and transverse component of momentum are conserved. In order to make the approach simple and intuitive, the system is assumed to have a constant potential barrier (V_B). For the tunneling electrons, which are incident perpendicularly to the interface plane (i.e., when $\mathbf{k}_{\parallel}=0$), the decay factor κ can be obtained as:

$$\kappa^2 = \frac{2m(V_B - E_F)}{\hbar^2} - \frac{\langle \phi | \frac{\partial^2}{\partial x^2} + \frac{\partial^2}{\partial y^2} | \phi \rangle}{\langle \phi | \phi \rangle} \quad (3.1)$$

The first term is the same in the free-electron tunneling problem, but the second term, which is related to the nodes of the function $\phi(x, y)$ in the plane of the interface, is newly found. Because the second term, including minus sign, is always positive, the lateral oscillation of the wavefunction yields an additional increase in the decay rate. That is, the electrons, having a higher atomic curvature due to more lateral nodes, penetrate the barrier more slowly than those with a lower curvature, and have a lower probability of penetrating the barrier at all.

In the case of $\mathbf{k}_{\parallel}=0$, the atomic orbitals (s , p , and d) can be rearranged into three groups according to the symmetry condition, as summarized in figure 3.1. Each group has same in-plane modulation, so it has the same magnetic quantum number m_l related to the angular momentum of orbital along z-axis. The symmetry Δ_1 , at $m_l=0$, projects the circular shape on the xy-plane and includes the s , p_z , and d_{z^2} orbitals. The symmetry Δ_5 , i.e., at $m_l=\pm 1$, forms two ellipsoids and it contains

p_x, p_y, d_{xz} , and d_{yz} orbitals. Lastly, the symmetry Δ_2 (or $2'$), at $m_l = \pm 2$, has four pear-shaped balls on the xy -plane, where Δ_2 is regrouping with the $d_{x^2-y^2}$ orbital and the Δ_2' is regrouping with the d_{xy} orbital. In general, the attenuation rate varies as $\kappa(\Delta_1) < \kappa(\Delta_5) < \kappa(\Delta_2 \text{ (or } 2'))$.

For the case of $\mathbf{k}_{\parallel} \neq 0$, the influence of symmetry is more complex. Due to the existing transverse component, the Bloch states in the electrodes are coupled in a complicated manner with the decaying evanescent states, and the wavefunction becomes a mixture of various symmetry states, as below.

$$\Psi(\mathbf{r}, z) = \sum_{\mathbf{g}} c_{\mathbf{g}} e^{i(\mathbf{k}_{\parallel} + \mathbf{g}) \cdot \mathbf{r} - \sqrt{(2m/\hbar^2)(V_B - E) + (\mathbf{k}_{\parallel} + \mathbf{g})^2} z} \quad (3.2)$$

Here \mathbf{r} is a vector on the x - y plane, and \mathbf{g} is the reciprocal lattice vector.

3.2.2 The Layer Korringa-Kohn-Rostoker (LKKR) method

The Layer Korringa-Kohn-Rostoker (LKKR) technique [27] is a commonly used tool for determining the electronic density of states (DOS) of a solid crystal. The LKKR technique is a self-consistent method based on the density functional theory (DFT) with the local spin density approximation (LSDA) or other approximations. By accounting for the scattering events an electron encounters within a solid, the LKKR can examine electronic and magnetic structures and ultimately allow for calculation of the transmission and reflection amplitudes of the tunneling electrons.

LKKR Calculation Scheme Overview

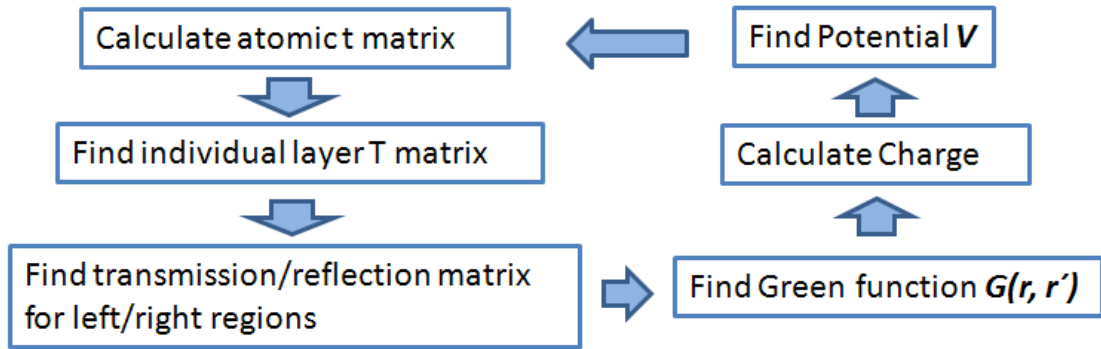


Figure 3.2 Schematic overview of the LKKR calculation, repeated until self-consistent.

The LKKR technique approaches the system as a multi-layered structure. Starting with a single atomic layer, all the potential effects are divided and applied to each layer, after which a scattering matrix for each layer can be obtained. Subsequently, this single-layer matrix is extended to multi-layers. Mathematically, this approach can be derived from perturbation theory and Green function expansion. When the Hamiltonian is expressed as the summation of the free-space Hamiltonian (H_0) and the perturbing potential (V), the wavefunction can also be presented as the sum of the free-space wavefunction (χ) at a position (r) with contributions by the perturbing potential (V) at different sites (r')

$$\psi(r) = \chi(r) + \int G_0(r, r') V(r') \psi(r') d^3 r', \quad (3.3)$$

where G_0 is the free electron propagator and is related to the electron under the potential V without scattering. From this, the system's Green function can be expanded into $G = G_0 + G_0VG$, and we can define the scattering matrix T as,

$$\begin{aligned} G &= G_0 + G_0VG = G_0 + G_0VG_0 + G_0VG_0VG_0 + G_0VG_0VG_0VG_0 + \dots \\ &= G_0 + G_0(V + VG_0V + VG_0VG_0V + \dots)G_0 = G_0 + G_0TG_0 \end{aligned} \quad (3.4)$$

$$\text{with } T = V + VG_0V + VG_0VG_0V + \dots$$

This scattering matrix T includes all possible scatterings within the potential assembly. Assuming that the potential (V) is divided into each layer, as in $V = \sum_i V^i$,

the T matrix can be expressed in terms of the single site scattering matrix t

$$\begin{aligned} T &= \sum_i V^i + \sum_i V^i G_0 \sum_j V^j + \dots \\ \Rightarrow T &= \sum_i t^i + \sum_i \sum_{j \neq i} t^i G_0 t^j + \dots, \quad \text{where } t^i = V^i + V^i G_0 V^i + \dots \end{aligned} \quad (3.5)$$

Furthermore, the scattering matrix T can be expressed as the summation of all the scattering sequences by layer, i.e., $T = \sum_{i,j} T^{ij}$, where $T^{ij} = t^i \delta_{ij} + t^i G_0 \sum_{k \neq j} T^{kj}$.

Therefore, following these mathematical expressions, the LKKR work can be divided into three steps: firstly, calculating the properties of the individual t matrices, then, calculating the scattering properties of each layer (T^{ij}), and lastly, embedding the layers between the two electrodes corresponding to the total system.

The LKKR is a self-consistent method, which means that it is calculated repeatedly until the approximation of a solution is arrived at within a suitable error. Based on the proper physical model, the charge distribution is initially applied to

determine the potential V . By dividing the potential to multi-layers, one can calculate atomic t matrix and the individual layer T^j matrix, thereby obtaining the transmission/reflection matrix for the system. This entire calculation allows one to newly define the Green function $G(r, r')$, which induces the charge redistribution. The general scheme of this calculation is overviewed in figure 3.2.

3.2.3 Transmission/Reflection matrices

The LKKR code generates the transmission and reflection coefficients $(t_{gg}^{++}, t_{gg}^{--}, t_{gg}^{+-}, t_{gg}^{-+})$ based on the plane waves, while calculating the electronic structures of the whole system. In order to compute the tunneling conductance, one must know the transmission and reflection matrices of the Bloch electrons, which are incident from one side of the sample. Therefore, it is necessary to transfer the transmission and reflection coefficients of plane waves to those of Bloch wavefunctions.

Prior to this process, the Bloch eigenfunctions of the bulk, for both electrodes, can be obtained from a transfer-matrix analysis, also derived from the LKKR simulation. When these Bloch wavefunctions are expressed as the summations of plane waves (in the form of $\exp(i\mathbf{K}_g^\pm \cdot \mathbf{r})$) over the reciprocal lattice vectors, they can be described as:

$$\phi_{k_z^\pm} = \sum_{\mathbf{g}} c_{k_z^\pm \mathbf{g}}^+ \exp(i\mathbf{K}_g^+ \cdot \mathbf{r}) + \sum_{\mathbf{g}} c_{k_z^\pm \mathbf{g}}^- \exp(i\mathbf{K}_g^- \cdot \mathbf{r}) \quad (3.6)$$

where the vectors \mathbf{g} in the wave vectors $\mathbf{K}_\mathbf{g}^\pm$ are two-dimensional reciprocal lattice vectors and the label + or – indicates the traveling direction. Here the wave vectors $\mathbf{K}_\mathbf{g}^\pm$ are found as,

$$\mathbf{K}_\mathbf{g}^\pm = \{(\mathbf{K}_\mathbf{g}^\pm)_{\text{Parallel}}, (\mathbf{K}_\mathbf{g}^\pm) \cdot \hat{z}\} = \{\mathbf{k}_\parallel + \mathbf{g}, \pm \sqrt{\frac{2m}{\hbar^2} E - (\mathbf{k}_\parallel + \mathbf{g})^2}\} \quad (3.7)$$

That is, the wave vector is composed of two components, parallel and perpendicular to the layers, and \mathbf{k}_\parallel is the transverse component of momentum \mathbf{k} which exists within the first Brillouin zone. The coefficients $c_{k_z^\pm \mathbf{g}}$ can be computed from the numerical simulations. Conversely, a plane wave can be represented in the expansion of the Bloch wavefunctions.

$$\exp(i\mathbf{K}_\mathbf{g}^\pm \cdot \mathbf{r}) = \sum_{k_z^+} \mu_{\mathbf{g}k_z^+}^\pm \phi_{k_z^+}(\mathbf{r}) + \sum_{k_z^-} \mu_{\mathbf{g}k_z^-}^\pm \phi_{k_z^-}(\mathbf{r}) \quad (3.8)$$

The expansion coefficients ($\mu_{\mathbf{g}k_z}^\pm$) can be derived from the inverse matrix of the coefficients $c_{k_z^\pm \mathbf{g}}$.

Assuming an electron is incident from the left electrode, the total wavefunction on the left-hand side of the barrier can be the summation of an incident plane wave from the left side and all reflected plane waves through the barrier. When the total wave function is extended on the basis of the Bloch states, the relationship is satisfied as:

$$\psi_\mathbf{g}^+ = \exp(i\mathbf{K}_\mathbf{g}^+ \cdot \mathbf{r}) + \sum_{\mathbf{g}} t_{\mathbf{g}\mathbf{g}}^{+-} \exp(i\mathbf{K}_\mathbf{g}^- \cdot \mathbf{r}) = \sum_{k_z^+} A_{\mathbf{g}^+k_z^+}^L \phi_{k_z^+}^L(\mathbf{r}) + \sum_{k_z^-} A_{\mathbf{g}^+k_z^-}^L \phi_{k_z^-}^L(\mathbf{r}) \quad (3.9)$$

where the coefficient $t_{\mathbf{g}\mathbf{g}'}^{+-}$ indicates the reflection amplitude of a plane wave from the reciprocal vector \mathbf{g} to \mathbf{g}' . By using equation (3.8), the coefficients of the Bloch states can be expressed in terms of the expansion coefficients ($\mu_{\mathbf{g}k_z}^\pm$) and the reflection coefficients ($t_{\mathbf{g}\mathbf{g}'}^{+-}$).

$$A_{\mathbf{g}^+k_z^+}^L = \mu_{\mathbf{g}^+k_z^+}^{L+} + \sum_{\mathbf{g}'} t_{\mathbf{g}\mathbf{g}'}^{+-} \mu_{\mathbf{g}'k_z^+}^{L-} \quad (3.10)$$

Similarly, the total wave function on the right-hand side can be the summation of the transmitted plane waves

$$\psi_{\mathbf{g}^+}^{R+} = \sum_{\mathbf{g}'} t_{\mathbf{g}\mathbf{g}'}^{++} \exp(i\mathbf{K}_{\mathbf{g}'}^+ \cdot \mathbf{r}) = \sum_{k_z^+} A_{\mathbf{g}^+k_z^+}^R \phi_{k_z^+}^R(\mathbf{r}) + \sum_{k_z^-} A_{\mathbf{g}^+k_z^-}^R \phi_{k_z^-}^R(\mathbf{r}) \quad (3.11)$$

$$\text{which satisfies the relationship of } A_{\mathbf{g}^+k_z^+}^R = \sum_{\mathbf{g}'} t_{\mathbf{g}\mathbf{g}'}^{++} \mu_{\mathbf{g}'k_z^+}^{R+} \quad (3.12)$$

On the other hand, in the case of the tunneling incident from the right electrode, the derived relationships must be in a similar form to the equations (3.10) and (3.11), but exchanging the labels + and -, and the superscripts L and R.

$$A_{\mathbf{g}^-k_z^-}^L = \sum_{\mathbf{g}'} t_{\mathbf{g}\mathbf{g}'}^{--} \mu_{\mathbf{g}'k_z^-}^{L-} \quad (3.13)$$

$$A_{\mathbf{g}^-k_z^-}^R = \mu_{\mathbf{g}^-k_z^-}^{R-} + \sum_{\mathbf{g}'} t_{\mathbf{g}\mathbf{g}'}^{-+} \mu_{\mathbf{g}'k_z^-}^{R+} \quad (3.14)$$

Therefore, based on these relationships, the matrices of $A_{\mathbf{g}^+k_z^+}^L, A_{\mathbf{g}^+k_z^+}^R, A_{\mathbf{g}^-k_z^-}^L, A_{\mathbf{g}^-k_z^-}^R$ can be calculated by using the already computed values, such as the expansion coefficients and the transmission and reflection coefficients of the plane wave.

Next, one must explore the entire process in terms of the transmission and reflection coefficients of the Bloch waves. The outgoing Bloch waves on the left side involve two components: the reflected Bloch waves incident from the left side, and the transmitted Bloch waves incident from the right side. This can be expressed mathematically as:

$$A_{\mathbf{g}^+k_z^-}^L = \sum_{k_z^+} A_{\mathbf{g}^+k_z^+}^L T_{k_z^+k_z^-}^{+-} + \sum_{k_z^-} A_{\mathbf{g}^+k_z^-}^R T_{k_z^-k_z^-}^{--} \quad (3.15)$$

In this equation, the superscript L or R means that the existing waves are either on the left or right side of electrode, and the subscript k^+ or k^- indicates the direction of the incident waves, either from the left or right side. Thus, $A_{\mathbf{g}^+k_z^-}^L, A_{\mathbf{g}^+k_z^+}^L$, and $A_{\mathbf{g}^+k_z^-}^R$ denote the amplitudes of the outgoing waves on the left side, the reflected waves from the left side, and the transmitted waves from the right side, respectively. In addition, $T_{k_z^+k_z^-}^{+-}$ and $T_{k_z^-k_z^-}^{--}$ indicate the reflection coefficients of the Bloch waves incident from the left side, and the transmission coefficients of the Bloch waves incident from the right side, respectively. Similarly, the outgoing Bloch waves on the right side are the summation of the reflected waves from the right side and the transmitted waves from the left side.

$$A_{\mathbf{g}^+k_z^+}^R = \sum_{k_z^+} A_{\mathbf{g}^+k_z^+}^L T_{k_z^+k_z^+}^{++} + \sum_{k_z^-} A_{\mathbf{g}^+k_z^-}^R T_{k_z^-k_z^+}^{-+} \quad (3.16)$$

$T_{k_z^+ k_z^-}^{++}$ and $T_{k_z^- k_z^-}^{-+}$ are the transmission coefficients for the Bloch waves incident from the left-hand side of the barrier, and the reflection coefficients for the Bloch waves incident from the right-hand side.

These expressions can be organized into a matrix form:

$$\begin{pmatrix} A_{\mathbf{g}^+ k_z^+}^R & A_{\mathbf{g}^+ k_z^-}^L \\ A_{\mathbf{g}^- k_z^+}^R & A_{\mathbf{g}^- k_z^-}^L \end{pmatrix} = \begin{pmatrix} A_{\mathbf{g}^+ k_z^+}^L & A_{\mathbf{g}^+ k_z^-}^R \\ A_{\mathbf{g}^- k_z^+}^L & A_{\mathbf{g}^- k_z^-}^R \end{pmatrix} \begin{pmatrix} T^{++} & T^{+-} \\ T^{-+} & T^{--} \end{pmatrix} \quad (3.17)$$

The transmission/reflection coefficients for the Bloch waves, T^{++}, T^{+-}, T^{-+} and T^{--} , can be obtained by using the coefficients, $A_{\mathbf{g}^{\pm} k_z^{\pm}}^L$ and $A_{\mathbf{g}^{\pm} k_z^{\pm}}^R$ that were already calculated from equations (3.10), (3.12)-(3.14).

3.2.4 Landauer conductance formula

Once the transmission coefficients are computed, the tunneling conductance can be obtained from the summation of these transmission coefficients based on the Landauer conductance formula, expressed as:

$$G = \frac{e^2}{h} \sum_{\mathbf{k}_{\parallel}, j, i} T(\mathbf{k}_{\parallel}, j, i) \quad (3.18)$$

This formula can be induced by considering two reservoirs, which have chemical potential μ_1, μ_2 and distribution function $f(\mu_1), f(\mu_2)$ with each other. When two reservoirs are connected in the z-direction, the current density J^+ flowing from

reservoir 1 to 2 can be described using the transmission probability of electrons, $T^+(\mathbf{k}, \mathbf{k}')$, transferring probability from momentum \mathbf{k} at reservoir 1 to momentum \mathbf{k}' at reservoir 2.

$$J^+ = \frac{e}{(2\pi)^3} \int d^3k v_z^+(\mathbf{k}) f(\mu_1) \sum_{\mathbf{k}'} T^+(\mathbf{k}, \mathbf{k}') \quad (3.19)$$

Here, the volume integral in the \mathbf{k} -space can be transformed into the products of the line integral along the z -direction and the summation over two-dimensional transverse

momentum space, i.e., $v = \frac{1}{\hbar} \frac{dE}{dk} \rightarrow v_z = \frac{1}{\hbar} \frac{\partial \varepsilon}{\partial k_z}$ and $\frac{Area}{(2\pi)^2} \int d^2\mathbf{k}_{\parallel} \rightarrow \sum_{\mathbf{k}_{\parallel}}$.

$$\begin{aligned} \therefore J^+ &= \frac{e}{Area} \sum_{\mathbf{k}_{\parallel}, j; \mathbf{k}', i} \frac{1}{2\pi} \int dk_z \frac{1}{\hbar} \frac{\partial \varepsilon}{\partial k_z} f(\mu_1) T^+(\mathbf{k}, \mathbf{k}') \\ &= \frac{1}{Area} \frac{e}{\hbar} \int^{\mu_1} d\varepsilon \sum_{\mathbf{k}_{\parallel}, j; \mathbf{k}'_{\parallel}, i} T^+(\mathbf{k}_{\parallel}, j; \mathbf{k}'_{\parallel}, i) \end{aligned} \quad (3.20)$$

where \mathbf{k}_{\parallel} (\mathbf{k}'_{\parallel}) is the transverse component of \mathbf{k} (\mathbf{k}'), and i and j are indices for degeneracy and spin channel. Similarly, the current density from reservoir 2 to 1 can be described as:

$$J^- = \frac{1}{Area} \frac{e}{\hbar} \int^{\mu_2} d\varepsilon \sum_{\mathbf{k}_{\parallel}, j; \mathbf{k}'_{\parallel}, i} T^-(\mathbf{k}_{\parallel}, j; \mathbf{k}'_{\parallel}, i) \quad (3.21)$$

In the equilibrium state, the net current is zero, $J^+ = J^-$. Therefore, the summations of transmission probability of both directions are the same.

$$\sum_{\mathbf{k}_{\parallel}, j; \mathbf{k}'_{\parallel}, i} T^+(\mathbf{k}_{\parallel}, j; \mathbf{k}'_{\parallel}, i) = \sum_{\mathbf{k}_{\parallel}, j; \mathbf{k}'_{\parallel}, i} T^-(\mathbf{k}_{\parallel}, j; \mathbf{k}'_{\parallel}, i) \equiv \sum_{\mathbf{k}_{\parallel}, j; \mathbf{k}'_{\parallel}, i} T(\mathbf{k}_{\parallel}, j; \mathbf{k}'_{\parallel}, i) \quad (3.22)$$

For a sufficiently small voltage, the net current can be expressed in equation (3.20) and (3.21) as the linear response to the applied bias voltage,

$$I = I^+ - I^- = \frac{e^2}{h} \sum_{\mathbf{k}_{\parallel}, j; \mathbf{k}'_{\parallel}, i} T(\mathbf{k}_{\parallel}, j; \mathbf{k}'_{\parallel}, i) \frac{\mu_1 - \mu_2}{e} \quad (3.23)$$

Thus, the conductance can be represented as:

$$G = \frac{e^2}{h} \sum_{\mathbf{k}_{\parallel}, j; \mathbf{k}'_{\parallel}, i} T(\mathbf{k}_{\parallel}, j; \mathbf{k}'_{\parallel}, i) \quad (3.24)$$

If \mathbf{k}_{\parallel} is conserved during the transport, the conductance can be simplified to the equation (3.18). In summary, the Landauer formula reveals that the conductance of each spin channel can be expressed as the summation of transmission coefficients over the 2-D Brillouin zone.

3.3 Butler *et al.*'s calculation

Butler *et al.* calculated the tunneling conductance on a Fe/MgO/Fe (001) epitaxial system based on the density functional theory (DFT). First, they found a precise image of the structure, including the Fe-O interface which minimizes the total energy. Then, they obtained the electronic structure using the LKKR technique. The calculated electronic density of states (DOS) of Fe and MgO for each spin was used for finding the transmission amplitude of Bloch waves, after which the tunneling

conductance was computed for parallel and anti-parallel alignments with different thickness of MgO layer.

3.3.1 Structure of iron-magnesium oxide

In order to compute the tunneling conductance, the first step is to get a reliable physical model of the Fe/MgO/Fe (100) epitaxial system, including a precise image of Fe-O interface. Experimentally, the growth of Fe on MgO [28-31] and MgO on Fe [32] are well-studied. According to the low energy electron diffraction (LEED) experiments [33], one can infer that Fe atoms sit on top of O atoms on a clean single-crystal MgO (100) substrate, while an MgO film grows layer-by-layer onto a bcc crystalline Fe (100) structure with a 45 ° rotation as O atom sits onto the topmost Fe atoms. Even though the exact Fe-O separation is hard to obtain experimentally, LEED data suggests around 2.0 Å as the distance between Fe and O at the interface.

Theoretically, the physical images of the whole stack can be obtained by calculating the total energy of the system. The structure which results in the lowest energy can be regarded as having the optimized geometry and proper atomic arrangements. Li and Freeman made the total energy calculation based on the density functional theory (DFT) with the local spin density approximation (LSDA), implemented using the full potential linearized augmented plane wave (FLAPW) technique [34]. They used a physical model with five monolayers of MgO (100) sandwiched between one or two layers of Fe. This calculation showed that Fe atoms are likely to rest on O atoms and that the distance between Fe and O is obtained at 2.3 Å.

Similarly, Butler *et al.* calculated the Fe/MgO/Fe (001) structure by using the full potential DFT-LSDA with the plane wave pseudopotential technique. They used a model with five MgO (100) layers covered by five layers of Fe (100) on both sides. They found 2.169 Å as the Fe-O distance, which is between the value measured by LEED and the value predicted by implementing the FLAPW technique. The calculation also predicted that the spacing between the first and second layers of Fe would be slightly smaller (~2 %) than the spacing between next two layers, and that the Mg atoms in the first MgO layer would shift 0.05 Å towards the Fe side at the interface.

3.3.2 Electronic and magnetic structure

The electronic density of states (DOS) for each spin channel has to be calculated to determine the electronic and magnetic structures of the system. The Layer Korringa-Kohn-Rostoker (LKKR) technique was used for this work. The physical model, which has an MgO insulating barrier inserted in the middle of two semi-infinite Fe leads with the Fe-O distance of 2.16 Å, was used for the LKKR code. Even if the LKKR does not require periodicity or symmetry to the perpendicular direction of the interface in principle, using semi-infinite stacks can make the calculation much simpler with two-dimensional translational symmetry. The LKKR calculation used LSDA with DFT, which includes Perdew-Zunger parametrized approximation on the exchange-correlation energy, in order to consider magnetic property [35].

As previously noted, the LKKR is a self-consistent method. This iterative method induces the charge redistribution along the entire junction in order to correct the offsets of Fermi energies of Fe and MgO layers. The calculated rearrangement of charge is shown in figure 3.3, where a small amount of electron transfers from MgO to Fe at interface, forming a weak dipole layer. This small charge transfer between Fe and MgO is also demonstrated in other calculations using FLAPW [34].

The electronic DOS for an Fe/MgO/Fe (001) is shown in figure 3.4 and 3.5. For the Fe layers (in figure 3.4), the DOS of the interfacial layer is different from that of the bulk regardless of spin channel, but the actual tendency near the interface is the opposite between the majority and minority DOS. That is, the majority DOS of the interfacial layer decreases near the Fermi energy, while the minority DOS of the interfacial layer shows a sharp localized peak. The peak seems to come from an interfacial resonance state (IRS), which can be weakly coupled with the bulk states so that it can contribute the additional tunneling conductance for the minority spin channel. On the other hand, for the MgO layers (in figure 3.5), a wide bandgap is presented, especially for the interior layers of MgO. This gap has a width of around 5.5 eV, which has a good agreement with the other calculation results, but is less than the experimentally measured value of 7.8 eV [36]. Comparatively, a small amount of DOS is found in the energy range of the bandgap on the interfacial layer. These states are interpreted to be from the evanescent states injected from the Fe electrode during the tunneling process.

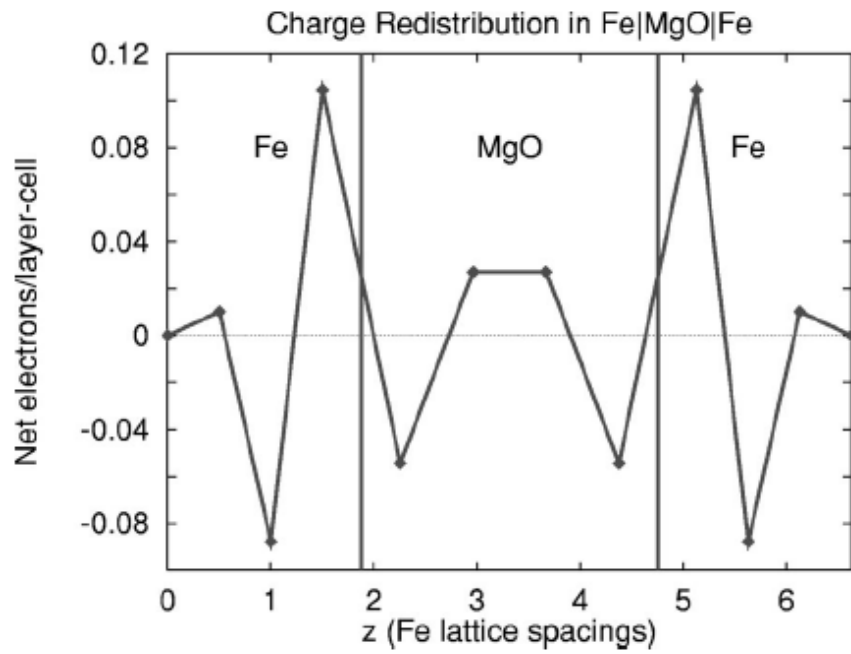


Figure 3.3 Charge redistribution in the Fe/MgO/Fe system, from the calculation of Butler *et al.* Referred from [8]

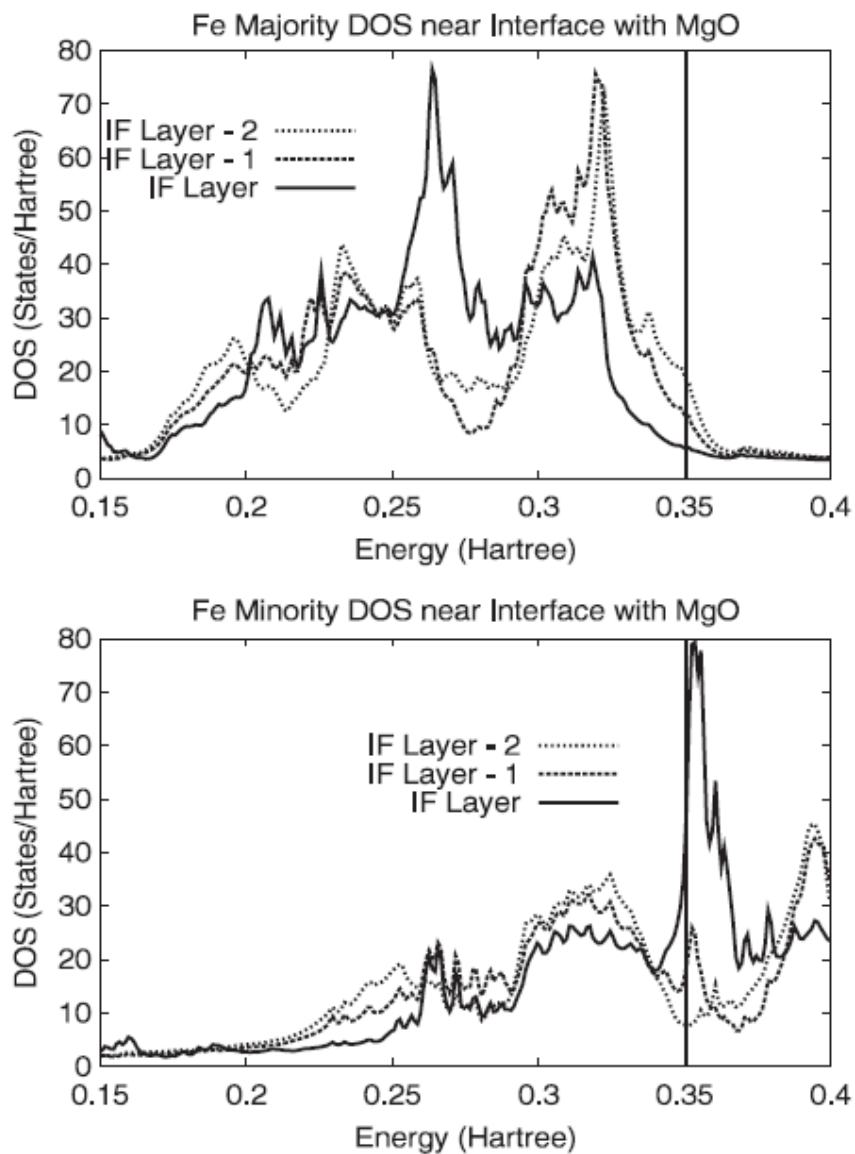


Figure 3.4 Density of states for Fe (100) layers and for each spin near an interface with MgO. One hartree is 27.2 eV. Referred from [15]

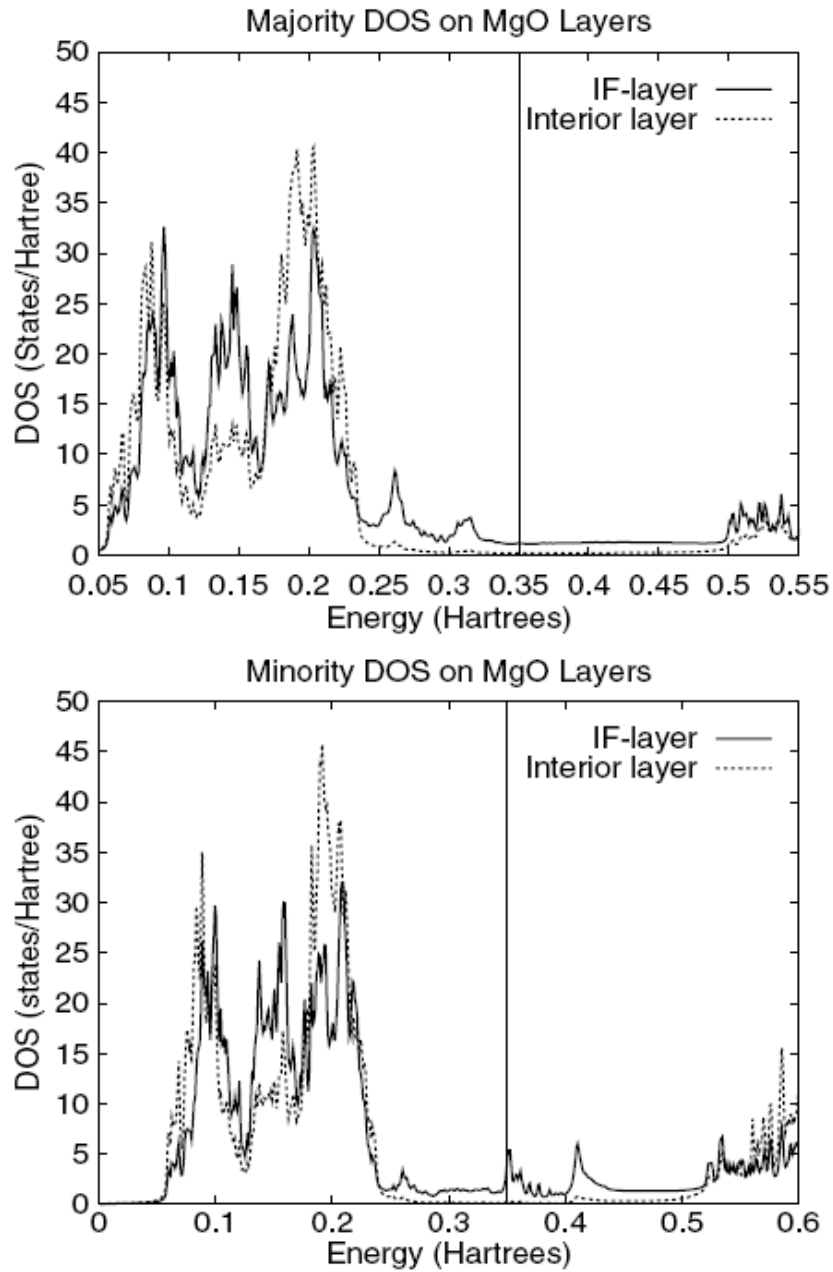


Figure 3.5 Density of states for MgO layers and for each spin near an interface with Fe (100), referred from [15]

3.3.3 Tunneling conductance at zero bias for an Fe/MgO/Fe (001)

When the magnetic moments of two ferromagnetic electrodes are aligned on the same direction, the majority spin of electrons in one electrode is equal to that in the other electrode and the tunneling between these electrons make the conducting channel for the majority spin. Similarly, the tunneling of electrons with the minority spin direction forms the minority spin channel. Therefore, the total tunneling conductance for the parallel alignment is the summation of the conductance of majority and minority spin channels. On the other hand, when two electrodes are magnetized at opposite directions, the majority spin direction in one electrode is the minority spin direction in the other, and vice versa. For a Fe/MgO/Fe system, when two electrodes are identical, the total tunneling conductance for the anti-parallel alignment can be represented as double the amount of the transmission conductance between the majority spin electrons in one electrode, and minority spin electrons in the other electrode.

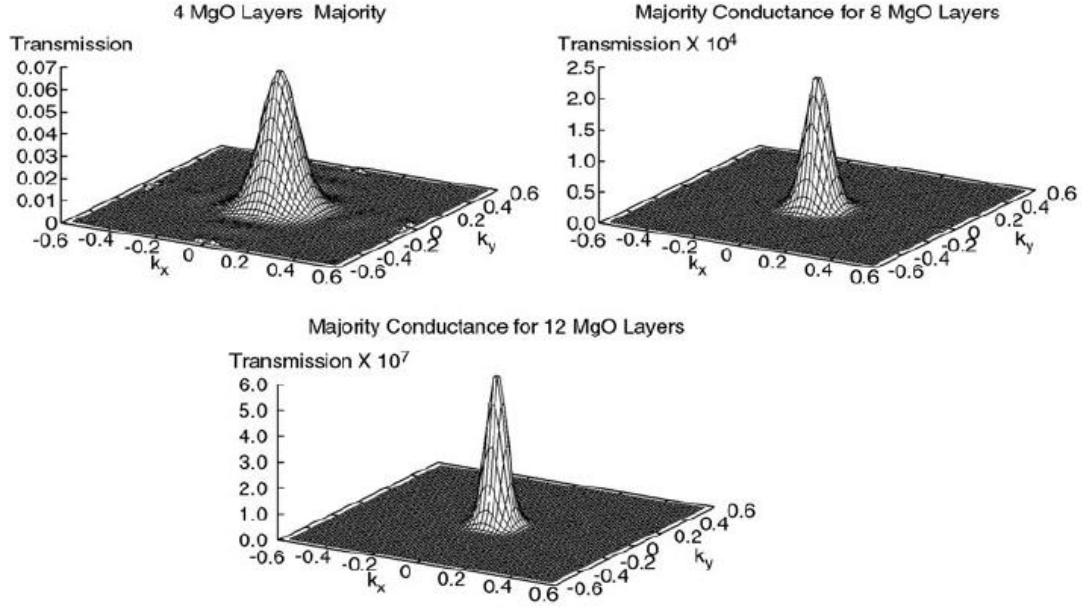


Figure 3.6 Majority conductance for 4, 8, 12 layers of MgO, calculated by Butler et al. Referred from [15]

The following figures show the calculated results of each tunneling case. The transmission conductivity for the majority spin channel is described on the \mathbf{k}_{\parallel} -space in figure 3.6, for the case of four, eight, and twelve layers of the MgO barrier. Regardless of the thickness of the barrier, it is clear that the conductance for the majority spin channel is concentrated at $\mathbf{k}_{\parallel}=0$. It is also noticeable that as the barrier becomes thicker, the transmission occurs closer to the center of $\mathbf{k}_{\parallel}=0$. These characteristics can be easily explained by using the simple free-electron model introduced in section 2.1. The tunneling current of free electrons decays exponentially through a barrier; i.e., it is proportional to $\exp(-2\kappa d)$ with the decaying factor of

$$\kappa = \sqrt{\frac{2m(V_B - E_F + k_{\parallel}^2)}{\hbar^2}}. \text{ Thus, for the thick insulating barrier, the transmission is}$$

dominant at $\mathbf{k}_{\parallel}=0$.

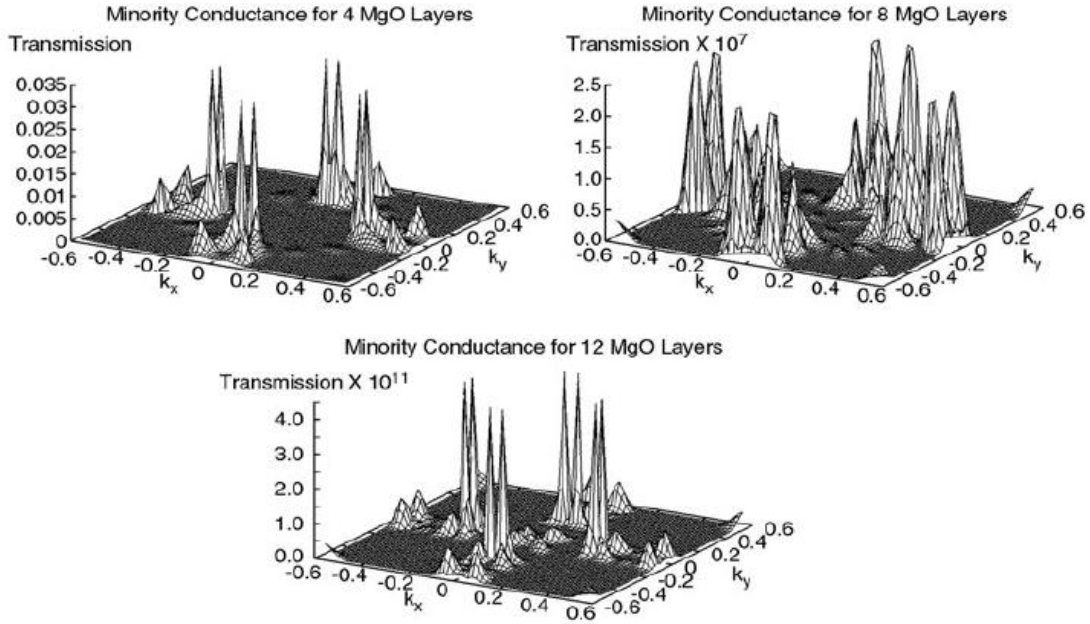


Figure 3.7 Minority conductance for 4, 8, 12 layers of MgO, calculated by Butler et al. [15]

The case of the minority spin channel comes in stark contrast to that of the majority channel. The calculated transmission conductivity is shown in figure 3.7, in the case of having four, eight, and twelve layers of MgO barrier. Unlike in the majority spin case, the current peaks are distributed circularly around the center of $\mathbf{k}_{\parallel}=0$. As the barrier layer gets thick, the overall tunneling current also becomes highly suppressed. The spikes in the conductance are found at particular \mathbf{k}_{\parallel} points, especially along the axis line of $k_x=0$ or $k_y=0$. These peaks are called interfacial resonance states (IRS), from the localized states near the interface coupled with the bulk states.

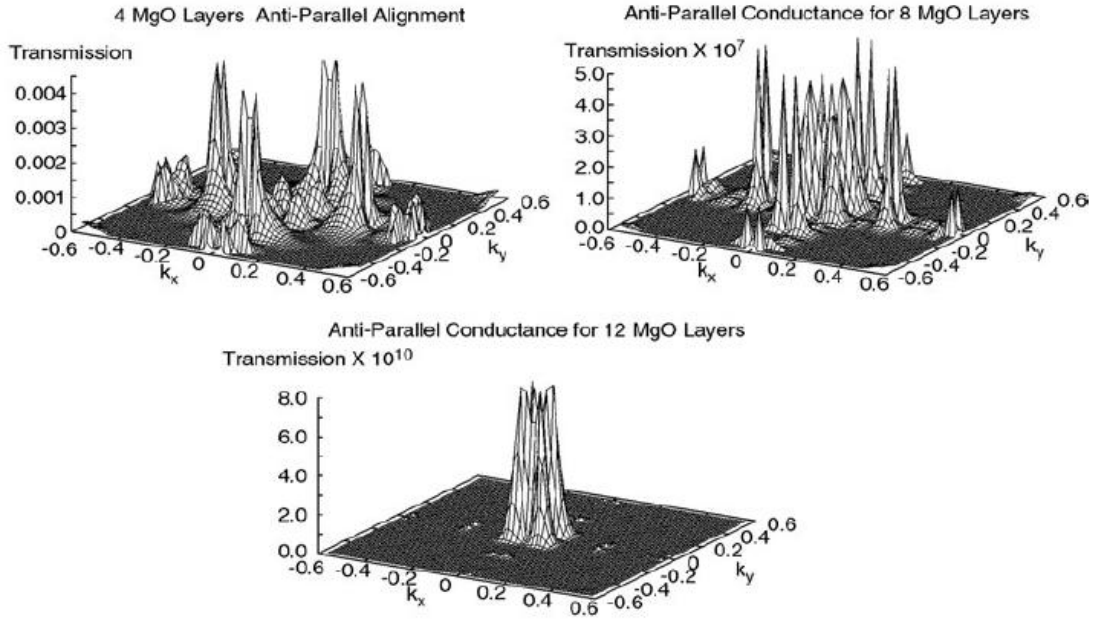


Figure 3.8 Conductance for the anti-parallel alignment of magnetic moments in the electrodes, calculated for 4, 8, 12 layers of MgO by Butler et al. [15]

In the case of the anti-parallel alignment, the calculated transmission conductivity is displayed in figure 3.8, which contains the features of the majority and minority conductance. Especially at a low barrier thickness, the conductance shows the combination of the majority and minority spin channels; it has high conductance near $\mathbf{k}_{\parallel}=0$, with sharp peaks from the IRS. As the barrier gets thicker, the conductance is more concentrated on the center of the two dimensional \mathbf{k} -space, implying a dominant contribution from the majority spin channel.

Based on these calculated results, the TMR can be roughly estimated by looking at the orders of magnitude. When we look at the case of 8 layers of MgO, the conductance of the majority spin channel is approximately 10^{-4} , and that of the minority spin channel is around 10^{-7} . Thus, the conductance for the parallel alignment is estimated to $10^{-4}+10^{-7}\approx 10^{-4}$, implying that the tunneling conductance is dominated by the contribution of the majority spin channel. Comparatively, the conductance for the anti-parallel alignment is shown to be around 10^{-7} . Therefore, the TMR, which is defined as the difference between the conductance for the parallel and anti-parallel alignments divided by the conductance for the anti-parallel alignment, is estimated to the order of 10^3 . Similar calculations can be made for the 4 and 12 layers of MgO. In the case of 12 layers of MgO, the conductance of the parallel alignment is about $10^{-7}+10^{-11}\approx 10^{-7}$ and that of the anti-parallel alignment is about 10^{-10} , which leads to a similar TMR with an order of 10^3 . However, the TMR value is somewhat less for the 4 layer case due to the fact that the summation of the majority and minority conductance is estimated to 10^{-1} , while the conductance for the anti-alignment is found to be greater than 10^{-3} .

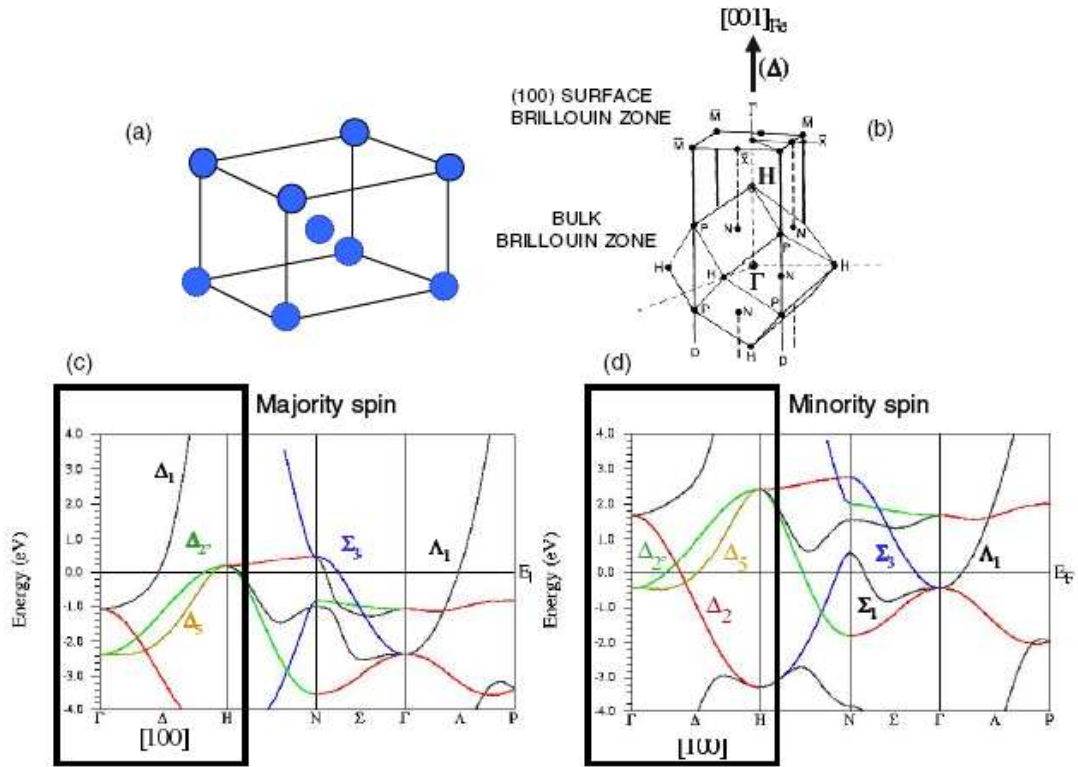


Figure 3.9 Density of states calculated for a bcc Fe (100) bulk, referred from [37]; (a) crystal structure of a bcc Fe, (b) reciprocal lattice structure in Brillouin zone, and DOS for majority spin (c) and minority spin (d)

3.4 The effects of symmetry in Fe/MgO/Fe (001) at $k_{\parallel}=0$

The high TMR theoretically predicted in a Fe/MgO/Fe (001) system can be understood in terms of the symmetry of the Bloch wavefunction. The influence of the Bloch states can be found both in the electrode and in the barrier. For a thick enough barrier, the tunneling is dominant along $k_{\parallel}=0$. Therefore, one must explore how these Bloch symmetries contribute the TMR on limiting the case to the tunneling at $k_{\parallel}=0$.

Firstly, depending on its symmetry, the Fe electrode has different emitting and receiving rates of electrons. This filtering effect can be understood by looking at the bulk band structure of bcc Fe shown in figure 3.9. As previously stated, because penetration along the [100] direction is dominant, the point of interest is in the band structure along the direction $\Delta = \Gamma-H$ in the reciprocal space. According to the band diagram in figure 3.9, at the Fermi level, the majority spin electrons can have four Bloch states: a Δ_1 state (spd-like character), two degenerate Δ_5 states (pd-like character), and Δ_2 state (d-like character), while the Δ_1 state is replaced by Δ_2 state for the minority spin electrons. Because there is no Δ_1 state for the minority spin, due to the exchange splitting, the Fe works as half-metallic in terms of the Δ_1 symmetry. Therefore, in a Fe/MgO/Fe structure, the difference in the existing symmetries and their momentum at the Fermi level makes for a different efficiency in spin injection and extraction at the interface between the ferromagnetic metal and the insulator.

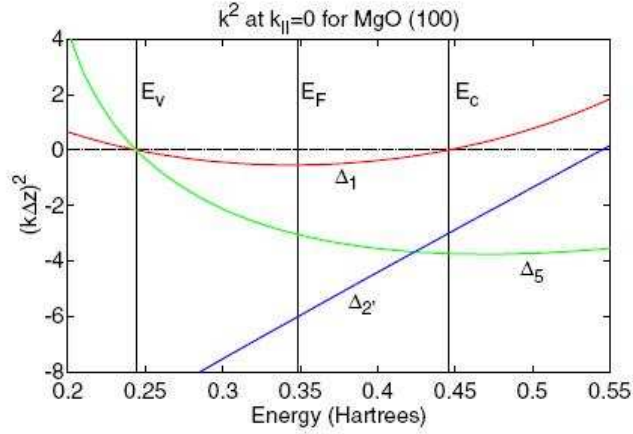


Figure 3.10 Dispersion $k^2(E)$ for MgO in the range of the bandgap along the [100] direction. E_V is top of valence band, and E_C is the bottom of the conduction band. Referred from [15]

Another spin-filtering effect can be found in the MgO barrier that each Bloch states have different decay rates. This property can be confirmed by considering the dispersion relationship within the bandgap energy of the barrier. The complex bands in the vicinity of the gap are plotted in figure 3.10, in which k^2 was calculated by the LKKR method with the potentials of the MgO bulk. In the figure, the relationship of $(k\Delta z)^2$ and energy is shown for the three symmetries of Δ_1 , Δ_5 , and Δ_2' (cf. for the Δ_2 symmetry, the smallest value of $-(k\Delta z)^2$ is around 31.5, far beyond from other symmetries), where Δz is the interplanar spacing for MgO (100) and k is along the [100] direction. The negative values of k^2 indicate exponential decay in the barrier, with a rate of $\exp(-\kappa\Delta z)$, where $\kappa\Delta z = \sqrt{-(k\Delta z)^2}$. The plot shows that the slowest

decay rate is for the Δ_1 symmetry, with a decay constant of $\kappa\Delta z \approx 1.47$, and the next slowest decay is for the Δ_5 symmetry.

The Bloch states in the Fe electrodes are coupled with the evanescent states in the MgO barrier: the Δ_1 state of Fe is coupled with the Δ_1 state of MgO, the Δ_5 state of Fe is coupled with the Δ_5 state of MgO, while the Δ_2 state of Fe is coupled with the Δ_2' state of MgO, and the Δ_2' state of Fe is coupled with the Δ_2 state of MgO because the MgO cubic cell is stacked with 45 ° rotation of the Fe crystalline. The calculated tunneling DOS for each spin alignment is plotted in figure 3.11 based on the Fe(100)/8 layers of MgO/Fe(100) structure. It is noticeable that the upper panels in the figure indicate the tunneling DOS of the two spin channels for the parallel alignment, and the lower panels indicate the anti-parallel alignment of two electrodes. Remarkably, when MgO has a great enough thickness, the tunneling conductance for the parallel alignment is governed by the Δ_1 state, and is much higher than that of any other state because the Δ_1 Bloch state exists only for the majority spin and has the slowest decay rate. Therefore, based on the spin filtering effects of the Fe electrode and the MgO barrier, the TMR is expected to be very high in this system.

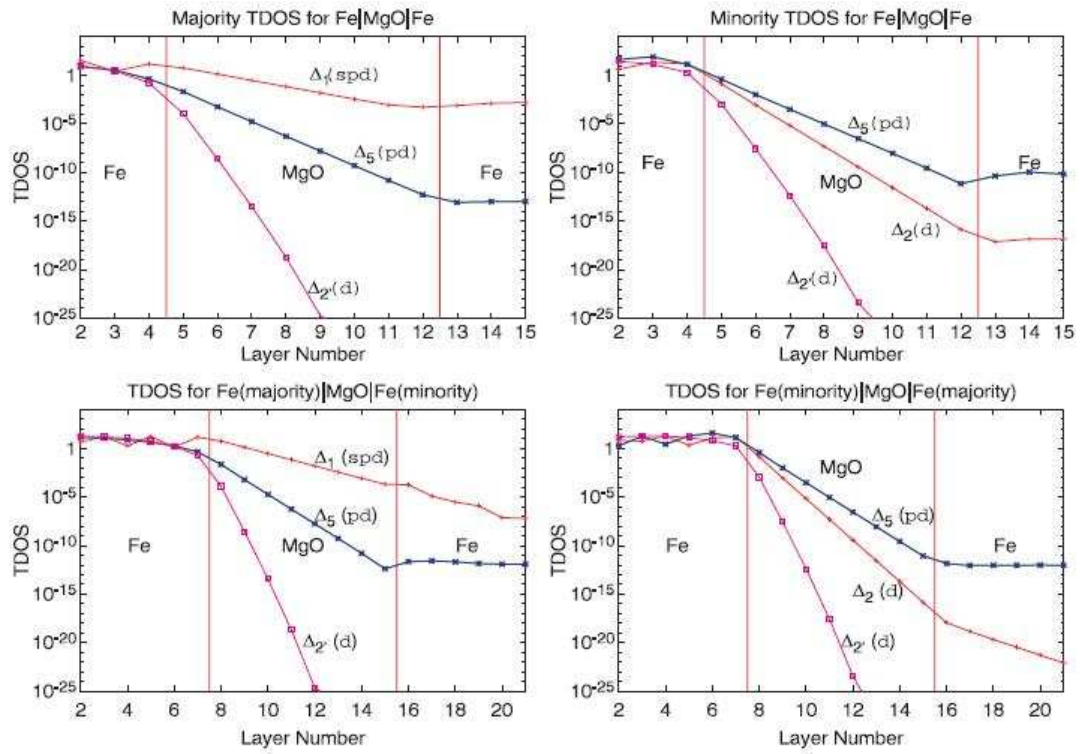


Figure 3.11 Tunneling DOS for $k=0$ for Fe/8 layers of MgO/Fe (100). Referred from [15]

Chapter 4

Overview of Scanning Probe Technique

4.1 Overview of Scanning Tunneling Microscopy/Spectroscopy

Scanning tunneling microscopy (STM) and spectroscopy (STS) are powerful techniques for studying solid surfaces down to the atomic level. The main premise of their operation is that the magnitude of the tunneling current between a sharp metal tip and a sample is extremely sensitive to the distance of separation. This allows for a high resolution imaging capability, ultimately leading to the observation of atomic registry and various surface morphologies. In addition, the tunneling current includes information about the local electronic density of states (DOS) of the surface, because the DOS at an energy of a few eV relative to the Fermi level is directly related to the amount of available tunneling electrons at the bias voltage of V . Thus, STM/STS can be used for measuring the structural, electronic, and chemical properties of the sample surface. This chapter draws on available literature to provide a review on the general operating principles of STM and STS, including the tunneling phenomenon [16, 38-43]

I-D electron tunnel Junction

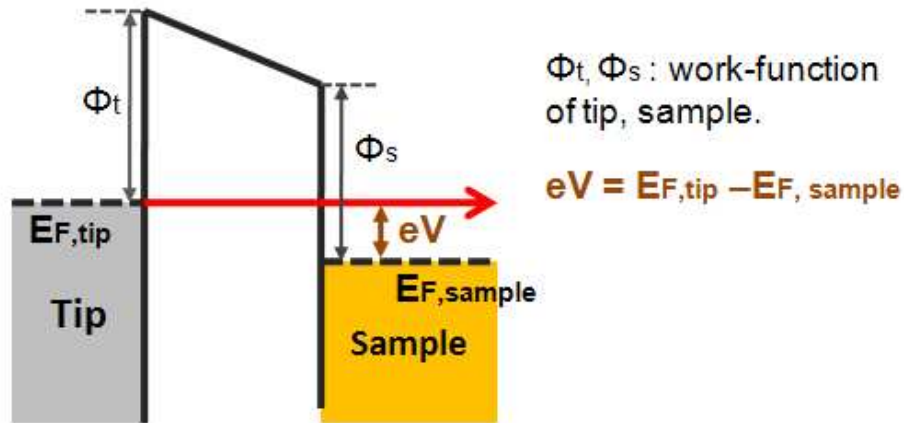


Figure 4.1 Simple diagram of a one-dimensional electron tunnel junction, which can be applied to the STM setup as a tip-vacuum sample structure. Applied bias voltage (eV) makes the shift of the Fermi level between tip and sample.

4.1.1 Tunneling phenomenon

Classically, a particle cannot penetrate through a region if its potential energy is higher than the total energy. But according to quantum mechanics, a particle with very small mass, such as an electron, would have a considerable possibility of passing through a potential barrier. This phenomenon is called tunneling, and can be explained by considering the probabilistic wave-like characteristic of a given particle.

The simplest case of tunneling is one-dimensional tunneling with a rectangular potential, which was briefly explained in chapter 2.2.1. As shown in equation (2.4), the tunneling current decays exponentially with the product of the barrier width (d) and square root of the potential height (\sqrt{V}). This can be directly

applied to the STM setup of a tip-vacuum-sample structure. A 1-D diagram of the electron tunneling junction of STM is shown in figure 4.1, ignoring the transverse component of the momentum ($k_{\perp}=0$) so that the tunneling current can be simplified as:

$$I \propto |\Psi(z = d)|^2 \propto e^{-2\kappa d}, \quad \text{where } \kappa = \frac{\sqrt{2m(V - E)}}{\hbar} \quad (4.1)$$

Here, V is the potential energy of the barrier and E is the total energy of the tunneling electron. Since the tip and sample are generally different materials, an electron incident from one side encounters a different potential barrier than an electron from the other side. In the case of equilibrium, when the Fermi levels of the tip and sample are aligned, the potential height from either the tip or the sample to a vacuum can be expressed as the work-function of the tip or sample (Φ_t , Φ_s , respectively). For a small bias, this potential can be estimated as the average of the workfunctions of tip and sample ($\Phi = \frac{\Phi_t + \Phi_s}{2}$), which simplifies the decaying factor to $\kappa \approx \frac{\sqrt{2m\Phi}}{\hbar}$. Since the workfunction of most metals is around 5 eV, the tunneling current decreases by approximately one order of magnitude for the vertical change of 1 Å.

Beyond this simple approach, the actual description of tunneling is more complicated and depends strongly on the applied bias voltage (V) as it affects the corresponding densities of empty or filled states of tip and sample. In order to reflect this dependence, Tersoff and Hamann proposed a more sophisticated model applying Bardeen's tunneling theory to STM [44, 45]. Based on first-order perturbation theory, Bardeen's solution to the 1-D tunneling problem can be modified into the summation form below:

$$I = \frac{2\pi e}{\hbar} \sum \left\{ \underbrace{f(E_\alpha)[1 - f(E_\beta + eV)]}_{\substack{\text{Transmission} \\ (\alpha \Rightarrow \beta)}} - \underbrace{f(E_\beta + eV)[1 - f(E_\alpha)]}_{\substack{\text{Transmission} \\ (\beta \Rightarrow \alpha)}} \right\} |M_{\alpha\beta}|^2 \underbrace{\delta(E_\alpha - (E_\beta + eV))}_{\text{Elastic tunneling}} \quad (4.2)$$

Here, $f(E)$ is the Fermi-Dirac distribution function, and the tunneling matrix is:

$$M_{\alpha\beta} = \frac{\hbar^2}{2m} \int d\vec{S} (\phi_\alpha^* \nabla \phi_\beta - \phi_\beta \nabla \phi_\alpha^*) \quad (4.3)$$

The first term in brackets corresponds to the product of the occupied states at the Fermi level and the unoccupied states at the energy of eV above the Fermi level. This relates the transmission of electrons from left to right, which we denote as $\alpha \Rightarrow \beta$. The second term in the bracket refers, conversely, to electrons traveling from right to left. In the case of elastic tunneling (that is, tunneling in which no energy dissipation occurs) with the bias voltage of V applied between two metals (α , β), the tunneling can be expressed in terms of the difference in transmission probability between two tunneling directions and the corresponding tunneling matrix. By using the Fermi-Dirac distribution, the transmission from metal α to β can be regarded as the product of the amount of filled states of metal α and of empty states of metal β with the difference of energy as eV . The tunneling matrix is an interface integral of the wavefunctions of two metals, which determines the transmission rate. In the STM setup, the two metals are the tip and sample. To simplify the model, Tersoff-Hamann considered a tip as having an s-like spherical wavefunction, which is relatively featureless in and of itself. Under the Wentzel-Kramers-Brillouin (WKB) approximation, this summation form can be changed into the convolution integral of

the local density of states (DOS) of the sample ρ_s , and of the tip ρ_t , and its weighting factor of the transmission probability T . The tunneling current can be expressed as,

$$I \propto \int_0^{eV} \rho_s(r, E) \rho_t(r, eV - E) T(E, eV, r) dE \quad (4.4)$$

Ignoring thermal perturbation and assuming that tip has a constant density of states, the tunneling current can be interpreted as the local DOS of the sample at the tip position r , integrated over energy up to the bias voltage (V). This expression implies that the STM image is not a real topography but instead a measure of the surface distribution of the local density of electrons. The maximum of the transmission coefficient $T(E, eV)$ was calculated by Feenstra *et al.* [46] as,

$$T_{\max}(eV) = \exp\left(-\frac{2z\sqrt{2m}}{\hbar} \sqrt{\frac{\Phi_s + \Phi_t}{2} + \frac{eV}{2}}\right) \quad (4.5)$$

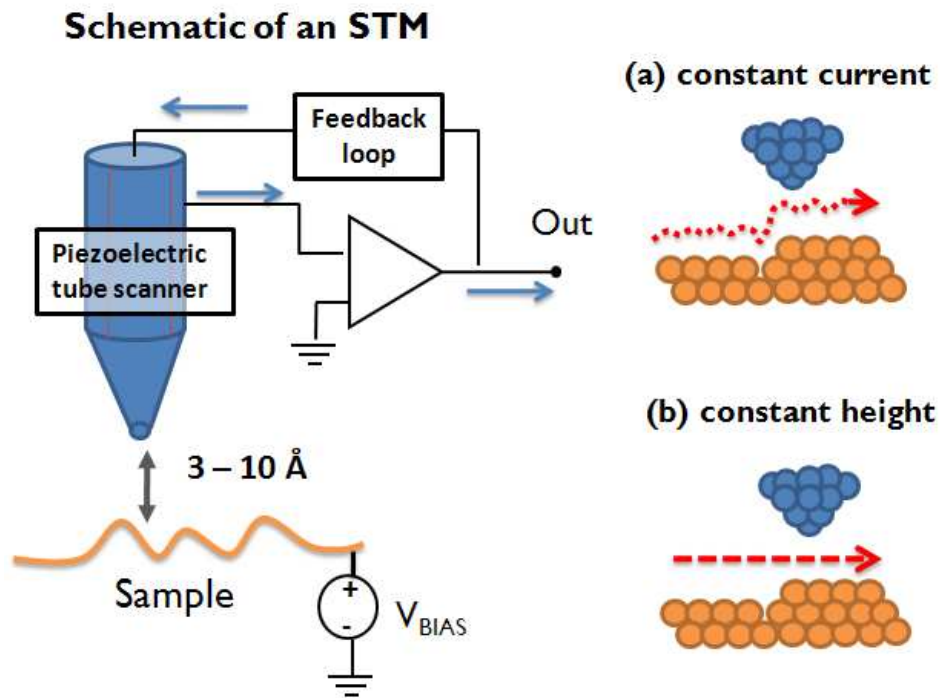


Figure 4.2 Schematic illustration of the STM operation. A sharp metal tip attached on a piezoelectric tube is brought close to a sample, and scans the surface features by maintaining (a) a constant tunneling current (with feedback loop) or (b) a constant tunneling height (without feedback). At constant current mode, the tip position is recorded for topography, while at constant height mode the measured tunneling current is translated into the topography.

4.1.2 Scanning Tunneling Microscopy (STM)

STM was invented in 1981 by Binnig and Rohrer, who were awarded the Nobel Prize in 1986 for this invention. In a typical STM operation, an atomically sharp tip (usually made of tungsten) is approached to within $3 \sim 10 \text{ \AA}$ of a surface and a bias voltage of less than 10 V is applied between the tip and sample. The corresponding tunneling current is in the range of a few tens to a few hundreds pico-Amperes. Again, an STM image is not the direct measurement of the geometric features of the sample, but the convolution of the LDOS of the tip and sample. That is, STM measures topography based on the electronic structure of the surface. Therefore, image interpretation requires a profound knowledge of the surface electronic structure and its relationship with the bias voltage. Virtual topographic effects such as variations in the measured heights can actually result from changes in the LDOS due to adsorbed atoms on surfaces [47-49].

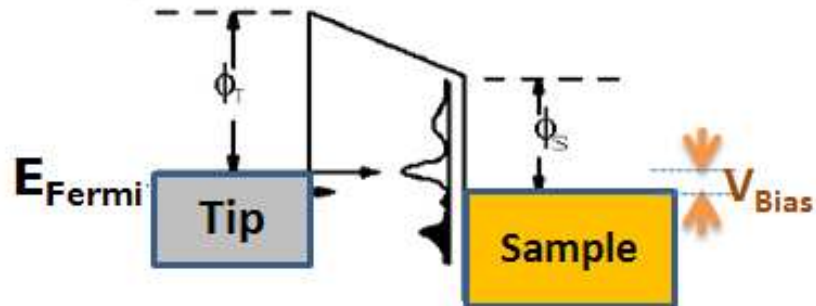
The STM runs in one of two modes: constant current or constant height. In constant current mode, as illustrated in figure 4.2 (a), a tunneling current is maintained as a set value by using a feedback loop. If the current changes, the feedback loop adjusts the tip height so the tunneling current remains constant. The height adjustment is made by applying the appropriate amount of bias voltage to the z- piezoelectric drive, which controls the vertical position of the tip. This voltage is recorded and translated into topographic information. Because of feedback, this approach reduces the chance of tip-sample crash and is therefore relatively safe. This mode is commonly used for imaging surface features with high precision and stability. The other alternative, the constant height mode, shown in figure 4.2 (b),

maintains the tip at a set distance from the sample, and the current is recorded during scanning. Since it does not use a feedback loop, it has much faster response time than constant current mode, increasing the scan speed and data acquisition time considerably. Thus, the constant height mode can be used for ‘real-time’ observation of atomic-scale surface dynamics such as surface diffusion. This mode is insensitive to low frequency distributions, such as mechanical vibrations, electronic noise, and low-frequency noise. However, the fast measurement without feedback increases the chances of tip-sample crash, which limits the scanning to atomically flat surfaces.

4.1.3 Scanning Tunneling Spectroscopy (STS)

Figure 4.3 schematically shows how the local DOS of the sample can affect the tunneling current based on the simple potential model of a tip-vacuum-sample junction. It is assumed that the local DOS of the tip varies very slowly with regard to the bias voltage, or that tip has a constant energy spectrum. This is a reasonable assumption for a tip made from tungsten, platinum, or iridium. Under this condition, the tunneling current is related to the number of contributing electronic states on the transmission, and represented by the local DOS of the sample. For example, when a positive bias voltage is applied to the sample, electrons move from the tip to the sample. That is, tunneling moves from the occupied states of the tip to the unoccupied states of the sample as shown in figure 4.3 (a). By increasing the bias voltage, more available states contribute to the tunneling. With the assumption of a featureless DOS of the tip, the current can be represented as the accumulation of the unoccupied states

(a) positive bias: unoccupied LDOS of sample



(b) negative bias: occupied LDOS of sample

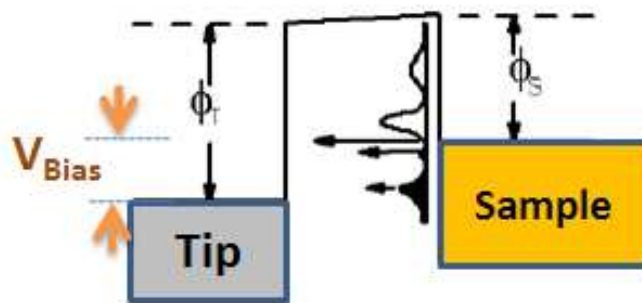


Figure 4.3 Energy diagram of a 1-D tip-vacuum-sample structure. Assuming that the tip has a featureless DOS, the DOS of the sample can only contribute the tunneling current as the function of the applied bias voltage. (a) At the positive bias voltage, the tunneling current can be proportional to the summation of the unoccupied states of the sample from the Fermi level to the bias, while (b) at the negative bias voltage, the current is the summation of the occupied states of the sample from the bias to the Fermi level.

of the sample from the Fermi level to the bias voltage. Therefore, the local DOS or the electronic property of the sample can be obtained by measuring the differential conductivity (dI/dV) of the tunneling current.

Mathematically, this relationship can be derived from the equation (4.4) as being differentiated.

$$\frac{dI}{dV} \propto \rho_s(r, eV)\rho_t(r, 0)T(eV, eV, r) + \int_0^{eV} \rho_s(r, E)\rho_t(r, eV - E) \frac{dT(E, eV, r)}{dV} dE \quad (4.6)$$

Typically the tunneling probability T is only weakly dependent on the bias voltage, even though the exact relationship is hard to compute. Nevertheless, a simple estimate of its tunneling effect can be estimated by using the maximum value of T in equation (4.5). This implies that an increase of an order of magnitude in the current is expected when the bias voltage increases 1 V. Since the tunneling probability T increases smoothly and monotonically with the bias (V) at a given location, the second term in equation 4.6 can be neglected as a background variation. Therefore the differential conductivity (dI/dV) can be expressed in terms of the local DOS of the sample (ρ_s) at a fixed location.

$$\therefore \frac{dI}{dV} \propto \rho_s(eV)T(eV) \quad (4.7)$$

Because $\rho_s(eV)$ changes more significantly than $T(eV)$, the STS can be used for characterizing the electronic properties of surfaces and absorbed materials.

Among several STS operation modes, a constant tip-sample separation mode is the most common [46]. In this mode, after the tip-sample height is stabilized by maintaining a fixed tunneling current, the feedback loop is turned off and the bias voltage (V) is swept, while the tunneling current $I(V)$ is recorded. At the same time,

another channel is used to measure the differential conductance (dI/dV) with a lock-in amplifier by adding a small amplitude of modulation voltage to the bias and detecting corresponding changes in the current. Feenstra *et al.* [50] demonstrated that the normalized differential conductivity $\{dI/dV/(I/V)\}$ for this method of operation exhibits the electronic density of states by minimizing the tip-sample effects. Feenstra *et al.*'s claim is also supported by the calculation of Lang [48] based on the adatom-on-jellium model.

The STS can also be performed using alternative operation modes, such as varying the tip-sample separation with a linear ramp of the bias voltage [51], or maintaining constant gap resistance [52] or current [53]. While convenient, extracting the LDOS information is more difficult since it involves the convolution of the DOS and the vertical location of the tip relative to the sample.

4.2 Overview of atomic/magnetic force microscopy (AFM/MFM)

Soon after the invention of the STM, it became evident that another related technique could be developed to image non-conducting surfaces. The earliest implementation was developed by in 1986 Binnig, Quate and Gerber [54], who invented the technique atomic force microscopy (AFM). Since then, AFM has evolved into a highly sophisticated yet easy-to-use surface imaging tool. It has proven to be versatile enough to be used not only for imaging topographic features but also for imaging magnetic and electric field distributions on the surface. The following sections will review some of the basic concepts of AFM and related techniques.

4.2.1 Interacting Forces between tip and sample

At very short-length scales, there are several forces that come into play between a tip and a sample. First is the combination of the Pauli repulsion and the Van der Waals attraction, which can be expressed numerically by using the Lennard-Jones potential:

$$F_{LJ} = \frac{2}{3} \pi^2 \varepsilon \rho_T \rho_S R \sigma \left(\frac{\sigma^2}{z^2} - \frac{\sigma^8}{30z^8} \right) \quad (4.8)$$

where ε is the dielectric constant, ρ_T and ρ_S are the density of electrons in the tip and sample, R is the radius of the tip, and σ is the decay length of the interaction. At the equilibrium position ($z=z_0$), force is equal to zero. If the distance is less than the equilibrium position ($z<z_0$), the Pauli repulsion is dominant, while at a distance greater than the equilibrium ($z>z_0$), the Van der Waals attraction is dominant. Because this Van der Waals force decays as fast as $1/z^8$, it is called a short-range force which governs the topographic image of the AFM.

Secondly, there is the electrostatic force between a tip and sample, as expressed below:

$$F_E = \frac{U^2}{2} \frac{\partial C}{\partial z} + \frac{q_T q_S}{\varepsilon z^2} \quad (4.9)$$

For a conductive tip and a conducting sample, the electrostatic force can be modeled as a simple capacitor, and the change of capacitance by distance can induce an additional force (the first term in the equation). In addition, if the tip and sample contain local charges, they exert Coulomb interaction each other, as reflected in the second term in equation.

Lastly, in the case of a magnetic tip and sample, a magnetostatic interaction, induces an additional force. Because the force can be obtained from the gradient of the potential energy, one must first calculate the magnetostatic potential between a tip and sample.

$$E_M = -\int \vec{M}_T \cdot \vec{H}_S dV_T = -\int \vec{M}_S \cdot \vec{H}_T dV_S \quad (4.10)$$

The potential can be interpreted in two ways: either the magnetization of the tip (\vec{M}_T) is interacting with the magnetic stray field of the sample (\vec{H}_S), or the magnetization of the sample is interacting with the stray field of the tip. Using the former interpretation, one can approximate the magnetic moment of the tip as a simple dipole (\vec{m}_T), and the force can be expressed as:

$$\vec{F}_M = \nabla E_T = \nabla(\vec{m}_T \cdot \vec{H}_S) = (\vec{m}_T \cdot \nabla)\vec{H}_S + \vec{m}_T \times (\nabla \times \vec{H}_S) \quad (4.11)$$

At equilibrium and steady state, the second term can be ignored, because according to Maxwell's equation the term $\nabla \times \vec{H}_S$ is related to the electrical current on the grounded sample. In general, the scanning rates are very slow to induce dynamical effects, which can be negligible. Similarly, the design of the sensing probes restricts the movement to the z-axis direction only, so the interacting force between a tip and sample can be simplified to the vertical component of the force in equation (4.11).

$$F_M^Z = \hat{z} \cdot (\vec{m}_T \cdot \nabla)\vec{H}_S = m_x \frac{\partial H_x}{\partial z} + m_y \frac{\partial H_y}{\partial z} + m_z \frac{\partial H_z}{\partial z} \quad (4.12)$$

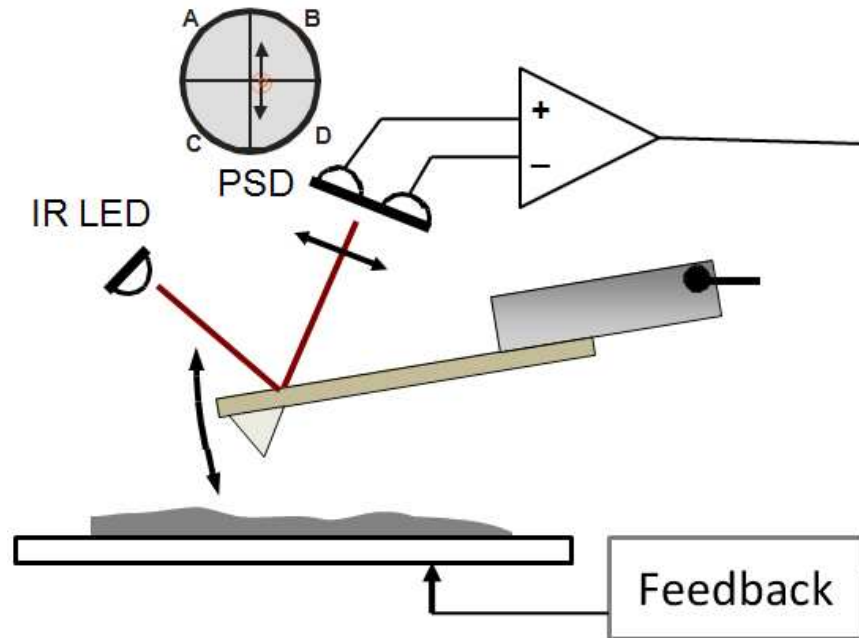


Figure 4.4 Schematic view of AFM detection: the deflection of cantilever is detected by the laser beam (IR LED), which is bounced on the rear side of the cantilever and then projected onto the position sensitive detector (PSD).

4.2.2 Atomic Force Microscopy (AFM)

AFM maps the topography of the surface by measuring the force (mainly Van der Waals force) or force gradient between a small sharp tip and a sample. AFM was invented by Binnig *et al.* [54] who using a hybrid STM/cantilever probe. This setup utilized an STM tip mounted on top of a cantilever to measure its deflection. Today, the technique for deflection has been significantly simplified. Generally, the displacement of the cantilever is now measured using laser beam deflection, in which a laser beam is focused on the reflecting rear side of the cantilever and the direction of the reflected beam is detected by a position-sensitive detector. The magnitude of the displacement of the cantilever is the input parameter to a feedback loop that

changes the tip-sample separation to maintain the set condition of cantilever deflection (force) or oscillation frequency (force gradient). The overall schematics are illustrated in figure 4.4.

AFM operates in either contact mode or non-contact mode. In contact mode, the force acting on the tip is directly measured as proportional to the deflection of the cantilever, according to Hook's law ($F = c \times d$, where c is the spring constant and d is the displacement). The amplitude of the detectable force is fundamentally limited by the thermal excitation of the cantilever, i.e. the thermal vibration energy is equal to the total energy of the cantilever ($\frac{1}{2}k_B T = \frac{1}{2}c \cdot d_{\min}^2$). By contrast, in non-contact

mode, the cantilever is harmonically oscillated by applying AC voltage. Its resonance frequency is expressed as $f_0 = \frac{1}{2\pi} \sqrt{\frac{c}{m_{eff}}}$, where m_{eff} is the effective mass of the

cantilever. When the force is applied, the vibrating frequency is shifted into

$f = \frac{1}{2\pi} \sqrt{\frac{c - (\partial F / \partial z)}{m_{eff}}}$, and the frequency shift is related to the force gradient, not to

force itself. The relative frequency shift is expressed below:

$$\frac{\Delta f}{f_0} = \frac{f - f_0}{f_0} = \sqrt{1 - \frac{(\partial F / \partial z)}{c}} - 1 \quad (4.13)$$

For a small amount of force gradient, the equation is simplified by using the Taylor expansion to the 1st order.

$$\frac{\Delta f}{f_0} \rightarrow -\frac{\partial F / \partial z}{2c} \quad (4.14)$$

This equation indicates that the detection of the relative frequency shift infers the direct information of the force gradient of the sample. The amount of the frequency shift is commonly measured by two methods: amplitude demodulation (AM), and frequency demodulation (FM).

4.2.3 Magnetic Force Microscopy (MFM)

MFM, first implemented by Martin and Wichramasinghe in 1987 [55], is used to detect the magnetostatic interaction between a magnetic tip and sample, and provides information on the magnetic domain configurations of the sample. Similar to the setup of AFM, a tip is located at the end of a cantilever, and force or force gradient is measured. As the tip is brought near the sample, it is influenced by the stray field of the sample, and the magnitude of its interacting force is shown in equation (4.11). The tip is magnetized vertically along the z direction by orienting its magnetization direction with a strong external magnet. The other components of the magnetic dipole of the tip can then be ignored, i.e., $m_x = m_y = 0$, so that the force further simplifies to:

$$F_M^Z = m_z \frac{\partial H_z}{\partial z} \quad (4.15)$$

This equation tells us that if the tip is prepared accordingly, the MFM can only detect the out-of-plane component of the magnetization of the sample. If the sample is magnetized in-plane, then the MFM can only detect magnetic domain walls that possess a strong vertical component, instead of the domain itself.

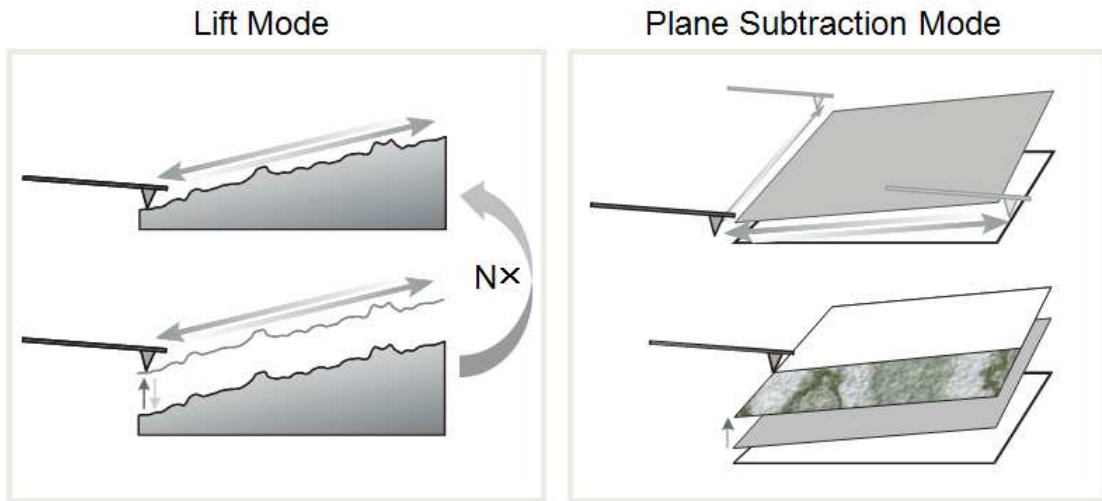


Figure 4.5 Schematic of the lift mode and plane subtraction mode: the lift mode has two consecutive scans. The first lift mode scans the topography, and the second scans again with a constant tip-sample height based on information from the first scan. The plane subtraction mode determines the slope of the sample plane along two sides, and then scans the surface following the measured plane slopes. This figure is the design of Dr. Michael Dreyer.

In order to separate the magnetostatic force from the other interactions, MFM relies on the fact that the magnetic force is long-range. At a tip-sample separation of 10 to 100 nm, this force becomes more dominant than the other short-range interactions that determine the topography. Like magnetism, the electrostatic force is long range, so for cases that have magnetic and electrostatic components, it may be hard to interpret data. However, one common trick used to minimize the electrostatic force is the application of a bias voltage with a balance of the contact potential between the tip and sample. Its influence can now be distinguished easily from the magnetic contrasts. To remove the background and topography, the MFM operates either in the lift mode [56] or in the plane subtraction mode [57], described in figure 4.5. In the lift mode, two sequential scans are performed on the same line of the sample. The topography is measured first, and then the MFM rescans the same line, following the prerecorded topography by maintaining a constant distance between the tip and sample. This method is the most commonly used, but it has some disadvantages including the fact that the sample can be modified by a strongly magnetized tip during the first pass, and that the strong magnetic interaction may be included in the topography measurement and thus the magnetic signal may be compensated and be weakened during the second scan. Alternatively, the plane subtraction mode compensates only for the overall tilt between the tip and substrate. Prior to the MFM scan, the slopes of two scan lines, one in x-direction and one in y-direction, are measured in order to define a plane parallel to the sample surface. This method has a rapid scan speed, but is only recommended for use on relatively flat surfaces.

Chapter 5

Study of Fe Ultrathin Films Grown Epitaxially on MgO

(001)

5.1 Introduction

The recent discovery of tunneling magnetoresistance exceeding 180% in Fe/MgO/Fe magnetic tunnel junctions has spurred interest in MgO-based systems as potential building blocks for spintronic devices such as non-volatile magnetic random access memories, magnetic sensors, resonant transistors, and logic devices [6, 7]. There is general agreement that the large magnetoresistance in these magnetic tunnel junctions is attributable to coherent spin-polarized tunneling between epitaxial interfaces with appropriate wavefunction symmetry [8]. The atomic registry, purity, and crystallinity of the layers are crucial factors that determine the magnitude of TMR. Thus, studies that involve the relationship between surface morphology and magnetic characteristics at the smallest possible length scales are crucial in advancing TMR technology. Some investigations of MgO on Fe and Fe on MgO have been reported in the literature [28-31], and some even predate the discovery of TMR [8, 26]. MgO on Fe grows layer-by-layer [32], while Fe on MgO proceeds by island formation and coalescence (Volmer-Weber) [28]. It is also known that crystallinity improves by post annealing. Similarly, the macroscopic magnetization curves representing the gross properties of the films have also been measured and explained.

However, despite extensive efforts, effects such as the increase in coercivity with growth temperature, uniaxial anisotropy, secondary switching in the magnetization curves, and many others, have yet to be fully understood. In particular, there is no direct link between the actual growth of the film and its magnetic structure at the local level.

This work was designed to study evaporated Fe thin films grown on MgO (100) under the cleanest possible conditions. The principal methods for analysis were scanning tunneling microscopy and magnetic force microscopy, performed under ultra-high vacuum conditions (UHV). UHV ensured that the surfaces were free of contamination and prevented the oxidation of iron films. It also improved magnetic imaging resolution [58]. The ultimate goal of this research was to synthesize a qualitative understanding of the relationship between growth modes and the magnetism of these films, thereby improving the development of spintronic devices. This was the first study of its kind.

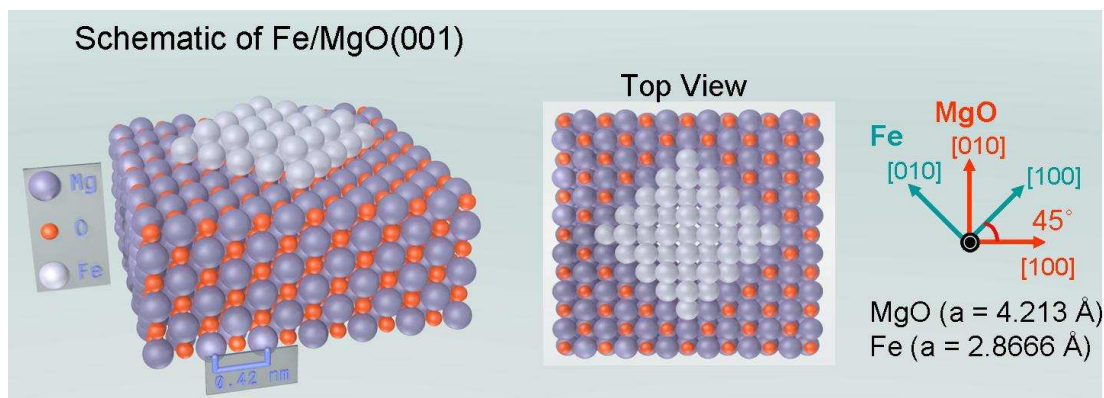


Figure 5.1 The Schematic of Fe growth on MgO (001) substrate. MgO has a NaCl-like face-centered cubic (fcc) structure with a lattice constant of 4.213 \AA , and Fe has a body-centered cubic (bcc) structure with a lattice constant of 2.8666 \AA . Thermodynamically, when Fe is deposited on MgO (001) crystal, Fe atoms rest on top of the O-site, which leads a good lattice match with a 45° rotation.

5.2 Experiments

The experiments were performed on an Omicron surface analysis system equipped with low energy electron diffraction (LEED), Auger electron spectroscopy (AES), a scanning probe system with atomic/magnetic force microscopy (AFM/MFM), and scanning tunneling microscopy (STM) capabilities. The analysis chamber was connected by a gate valve to a preparation chamber having an Ar⁺ sputtering source for sample cleaning, two electron beam evaporation guns, and a heatable substrate holder. The background pressure in both chambers was lower than 10^{-10} Torr.

The starting samples were single crystal MgO(100) substrates. They were prepared by several cycles of sputtering and annealing up to $950 \text{ }^\circ\text{C}$. Ar⁺ ions with

kinetic energy slightly higher than 1 keV were used to bombard the sample surface, removing the top layers of the substrate. This was followed by further annealing to make the surface smooth and healed the sputtering damage. Several repetitions of this step were required to not only remove the contaminants that initially covered the surface, but also to diminish the amount of residue contaminants that had migrated onto the surface from the bulk. The appearance of the surface after sputtering and annealing is shown in figure 5.2. Sputtering yielded a roughened surface, which was then smoothed annealing. The crystalline structure was further examined by observing the pattern of the Fourier transforms on the annealed image.

To find the optimized annealing temperature, several sputtered MgO substrates were heated at various temperatures and followed by AFM measurement. The results are shown in figure 5.3. Annealing at a temperature of less than 800 °C did not appear to improve the roughness of the surface, which continued to be more than 1 nm. However, at 900 °C the surface improved somewhat, and the roughness was reduced to around 0.6 nm despite some deep lingering defects on the surface. At temperatures between 930 ~ 960 °C, the surface improved significantly and a clear periodicity emerged from the Fourier transform shown in figure 5.2. The temperature range around 950 °C appears to be a sweet spot, since at higher temperature above 1000 °C, the surface again roughened significantly, presumably due to the evaporation of magnesium oxide. Thus, the temperature around 950 °C was found to be optimal for producing smooth MgO surfaces.

While annealing smoothens out the surface, the elevated temperature also increases the mobility of the dissolved carbon in bulk MgO. As a consequence,

carbon migrates from the bulk to the surface. The presence of carbon was monitored in the experimental sample by Auger electron spectroscopy, in which the carbon AES peak at 272 eV was observed until it fell below the noise level. Figure 5.4 shows a typical spectrum for a clean sample, clearly indicating very strong oxygen (512 eV) and Mg signals in comparison to the barely perceptible carbon peak. Once the MgO surface was prepared, the experiment focused on the deposition of Fe. Due to the unavailability of an in-situ thickness monitor, the Fe deposition rate was calibrated using a shadow mask on a dummy sample and measuring the thickness as a function of e-beam deposition time at a fixed evaporation current and voltage. This calibration procedure revealed a deposition rate of 1 Å/min.

Next, crystallinity was evaluated by measuring the LEED patterns. Low energy electron diffraction (LEED) patterns correspond to the reciprocal lattice of the surface and can be regarded rather loosely as the Fourier transform of the crystal plane. The figure 5.5 shows a representative LEED pattern for a 5 nm thin Fe at 400 °C. The (01) and (11) index beams are shown in (a) and (b) respectively, and their combination is shown in (c). These spots correspond to the bcc structure, which implies successful epitaxial growth of Fe on MgO (001).

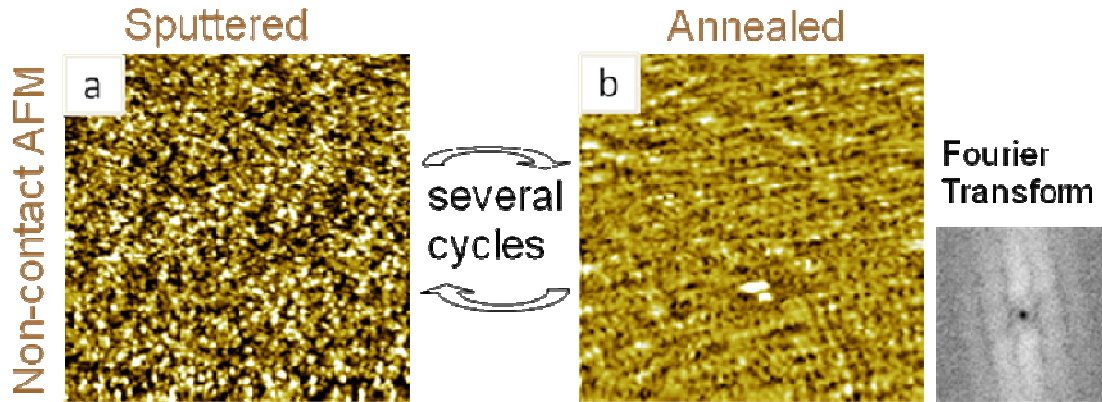


Figure 5.2 The preparation of MgO (001) substrate prior to Fe evaporation. The substrate was prepared by repeated cycles of sputtering with the energy of 1~1.5 keV and annealing up to 950 °C. The surface roughness (RMS) degraded with sputtering, and improved with annealing. The final surface state had an RMS roughness of less than 0.6 nm and a clear periodicity, as shown in the image of its Fourier transform (far right).

Two types of samples were prepared for this study: one with the substrate at room temperature (RT), and the other with a substrate at 400°C (HT) during growth. The high-temperature growth was chosen at 400°C to be consistent with earlier reports on Fe/MgO/Fe and similar spin filter devices [6, 7]. The following sections present results obtained on two Fe thicknesses, 4 nm and 14 nm, and a comparison and contrast of these results.

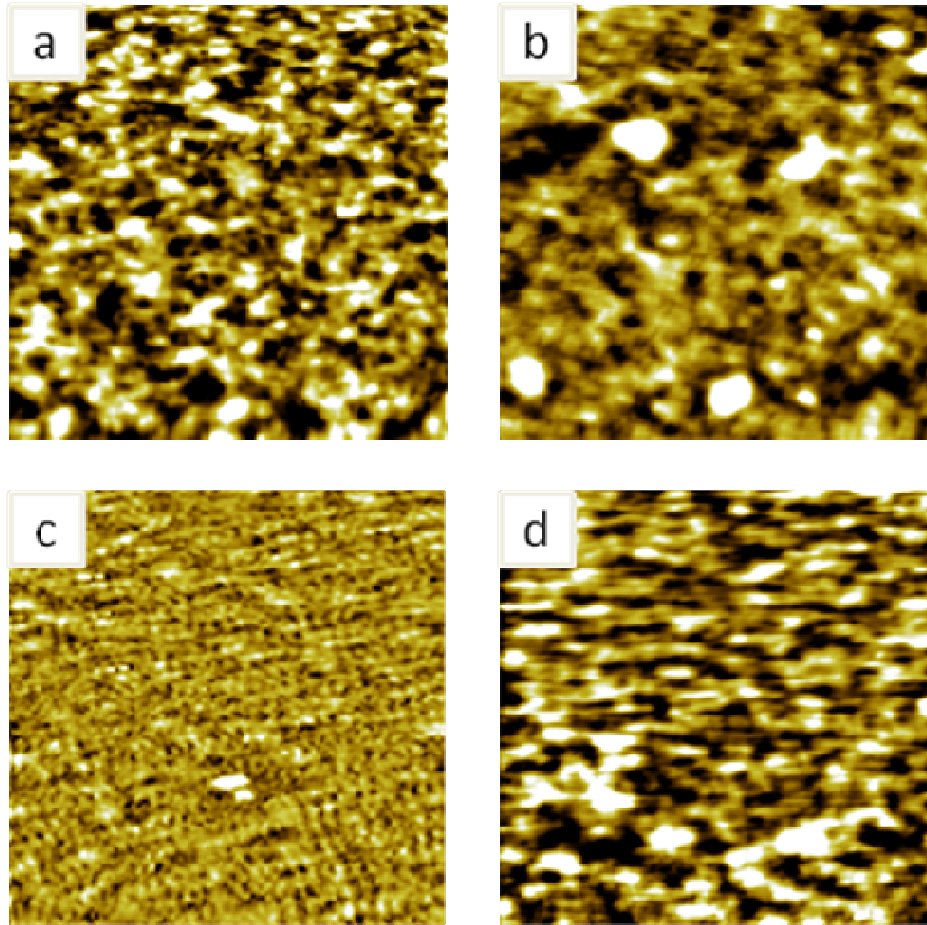


Figure 5.3 The effect of the annealing temperature on MgO (001) substrate. The AFM images describe the surface state after applying various temperatures of annealing, such as (a) less than 800 °C, (b) around 900 °C, (c) 930 ~ 960 °C, and (d) more than 1000 °C. Based on the improvement of roughness and periodicity, the optimized annealing temperature is found to be around 950 °C.

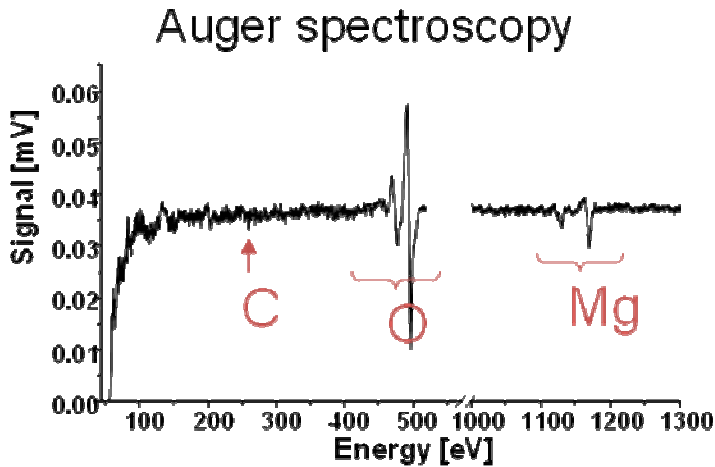


Figure 5.4 The Auger spectroscopy (AES) graphs onto the well prepared MgO (001) substrate. It shows clear peaks at an energy of around 500 eV and around 1150 eV, which correspond to the oxygen and magnesium peaks, respectively. Noticeably, the carbon, which is the main contaminant in bulk MgO, is not apparent on the graph. While carbon was initially detected on AES, it disappeared under the noise level after repeated cleaning process.

Low Energy Electron Diffraction (LEED)



Figure 5.5 Low energy electron diffraction (LEED) images on an ultrathin Fe film grown at 400 °C on MgO (001) substrate. The diffraction energy for each of these images is (a) 40 eV, (b) 65 eV, and (c) 78eV. These images show the bcc crystalline structure of the Fe film, indicating a good epitaxial growth.

Fe on MgO at room temperature

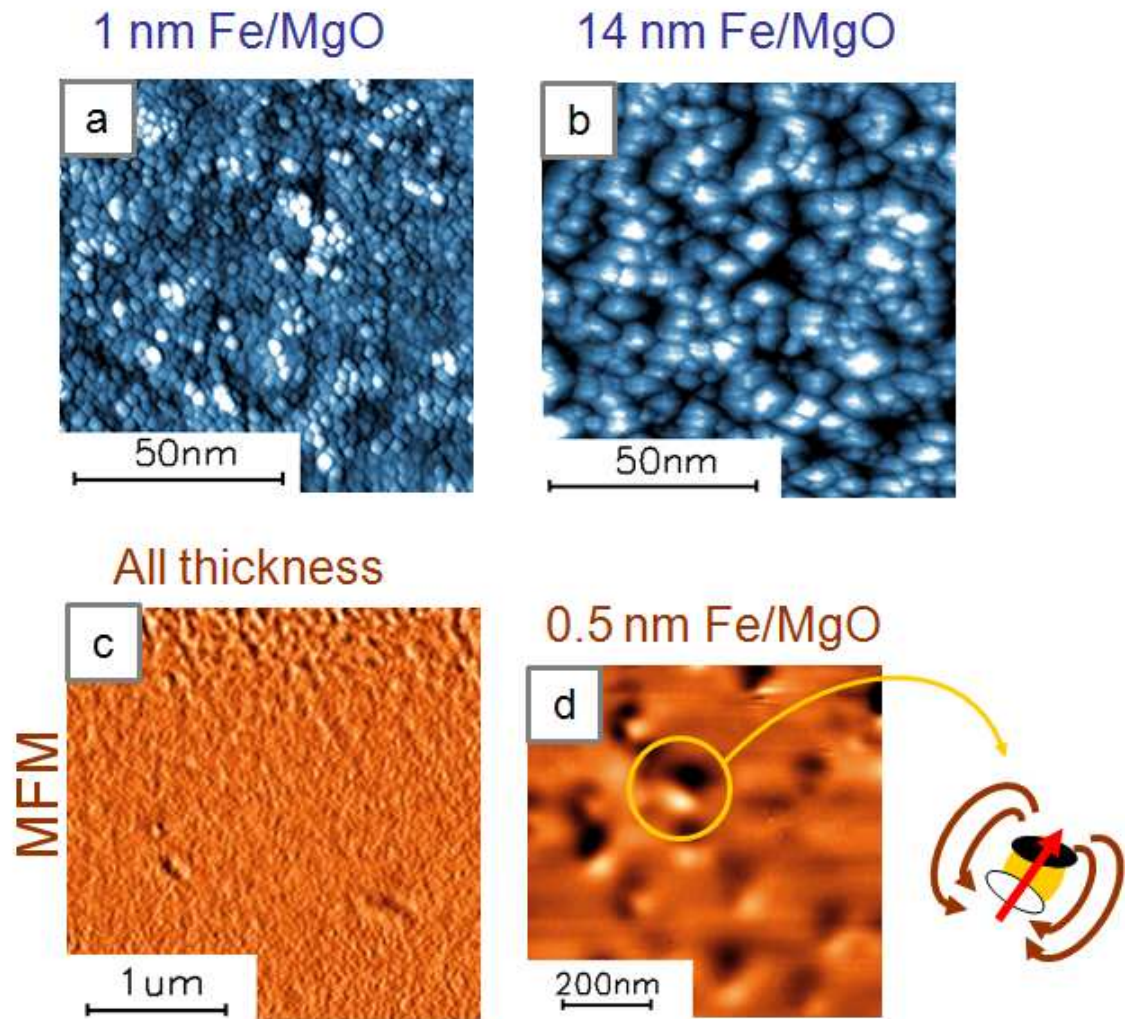


Figure 5.6 A thin Fe film grown on a MgO (001) substrate at room temperature. STM images of (a) 4 nm thick and (b) 14 nm thick film show that Fe grew as a random crystallite with overlapped round mounds. (c) The MFM image does not reveal any clear local magnetic variation, regardless of the thickness, except on a certain area that includes small magnetized particles, as shown in the image (d) (the MFM image of (d) is taken when Fe film is 0.5 nm thick).

5.3 Results and Discussions

Figures 5.6 - 5.8 show the representative images of the topography obtained using STM, and the magnetic structure observed using MFM. It is important to note that the length scales are very different, using tens of nanometers in the case of topography, and micrometers in the case of magnetic images. These images reveal a number of important experimental observations.

5.3.1 Effect of temperature on morphology

The first observation is the profound influence of deposition temperature on the growth of Fe film. Figure 5.6 (a) and (b) show the STM images of 4 nm and 14 nm thin Fe film deposited at the room temperature, while figure 5.7 (a) and 5.8 (a) describe 4 nm and 14 nm thin films grown at 400 °C.

At room temperature, shown in figure 5.6, Fe grew into a distribution of small grains with rounded edges. With the exception of a few fortuitous islands, there were no characteristically defined edges along the [110]-directions of the underlying MgO crystal. The grain size was scaled for thickness such that 2~3 nm diameter grains formed a 4 nm thickness film, and 5~10 nm diameter grains formed a 14 nm thick film. The rms surface roughness also changed from 0.46 nm to 0.80 nm, as did the corresponding peak-to-valley depth from 3.5 nm to 6.1 nm, respectively. We can also conclude from the images that the islands were interconnected, which formed a continuous Fe coating across the surface.

Fe growth at elevated temperatures came in stark contrast to the RT results. A high deposition temperature of 400°C induced Fe film into well-defined

crystallographic islands comprised of atomic terraces. This phenomenon is depicted in figures 5.7 (a) and 5.8 (a). Each terrace in these images is separated by steps, and the islands resemble the Ziggurat pyramids of ancient Mesopotamia. Careful analysis of the step profile of the images shows that the steps were mostly one single atom high, although in some regions the steps were in bunches. There were an average of 3 – 5 steps from the plateau to the base of each grain for the 4 nm film, and about 12 steps per pyramid for the 14 nm film. The trenches were about 1.7 nm deep. The four-fold symmetry is clearly evident from the shapes of the topmost plateaus. The same four-fold symmetry also appears in the Fourier transform of larger size STM images. Because the islands are interconnected and unevenly shaped, it is hard to put a firm number on the average dimension of the grains. Nevertheless, the average crystallite size was 30 nm for 4 nm film, and 50 nm for 14 nm film.

Compared to the room-temperature sample, the high-temperature sample showed a significant improvement in the surface roughness, which was about 0.21 nm and 0.34 nm for 4 nm and 14 nm thick films, respectively. This represents a factor of 2 improvement in smoothness relative to RT growth. One notable distinction in the 4 nm thin film is that the islands formed big crystalline grains of roughly 200 nm in size, but were not all connected. This can be observed on the 3-D image rendering in Figure 5.7 (b). By analyzing the surface roughness and peak to valley depth of the scans, one may conclude that in these relatively thin films, there were areas depleted of Fe between the islands. These observations are consistent with the large scale observations of others [59]. These results also established that below 1.5 nm, the islands have not sufficiently coalesced to allow for STM imaging.

4 nm Fe on MgO at high temperature (400 °C)

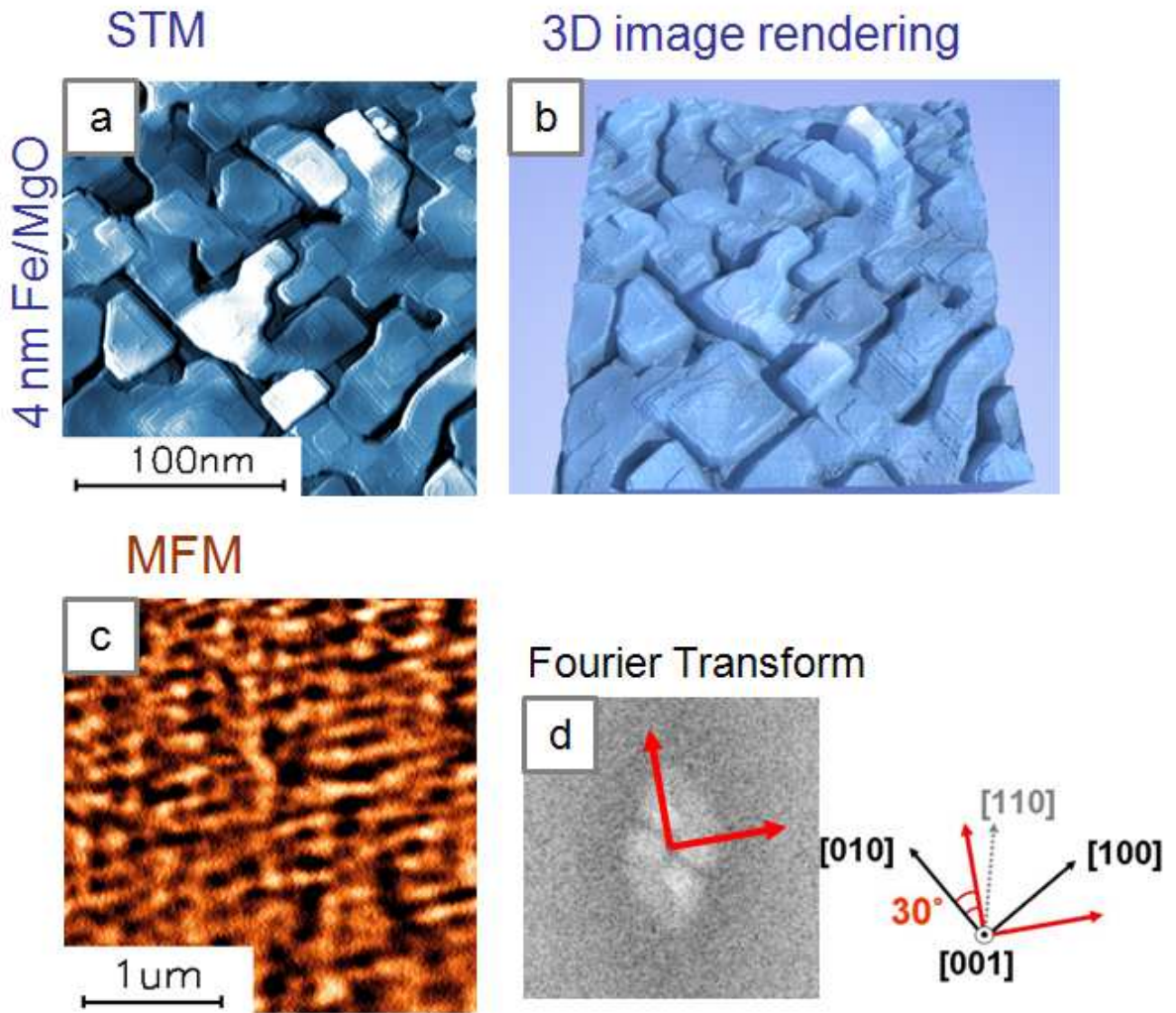


Figure 5.7 STM/MFM images of 4 nm Fe thin film grown on a MgO (001) at 400 °C: (a) an STM image, (b) its 3-D implementation, (c) an MFM image and (d) its Fourier transform. According to the scan images, the Fe grew into pyramid-like islands with well-defined atomic terraces, and had a complex magnetic structure, which implies weak magnetic coupling.

5.3.2 Magnetic configurations

Next, this research explored the change in magnetic structure as function of deposition temperature and film thickness. Figure 5.6 (c) shows the MFM image for the room-temperature sample, while figure 5.7 (c) and figure 5.8(c) are for high-temperature samples with 4 nm and 14 nm thicknesses. Again, the STM images are about 1/15 the size of the MFM images. In the case of room-temperature growth, Fe film at any thickness within the range from 0.5 nm to 14 nm showed little or no magnetic contrast as measured by MFM. This implies that the local magnetic variations or $(-\nabla \cdot \vec{M})$ were too small to be observed. Also, domain walls on this sample were not observed in UHV because of instrumental limitations in scan size. Subsequent results established the existence of domains that were several hundreds of micrometers apart using ex-situ MFM. Interestingly, for 0.5nm thin film, the results showed localized areas that appeared to be due to small magnetized particles or asperities on surface. As shown in figure 5.6 (d), these particles have bright and dark contrast on MFM, which indicate the magnetization direction.

By comparison, the magnetic structure of the 4 nm film grown at high temperature exhibited striped and checkerboard patterns, as shown in figure 5.7 (c). Without resorting to complex micromagnetic tools, it is difficult to determine the exact origin of the magnetic structure, including the question of whether the domains are in-plane or out-of-plane. However, a Fourier transform of the MFM image, shown in figure 5.7 (d), reveals a clear 4-fold symmetry. This strongly suggests that the observed magnetic patterns were correlated with individual islands. Incidentally, the average size of the magnetic structures was similar to the grain sizes, further evidence

that the complex magnetic image resulted from a distribution of crystallites that were randomly magnetized in-plane along the crystalline easy axes. The shape anisotropy of the islands may also have played a role.

At the thickness of 14 nm, the complex local patterns previously seen at 4 nm were replaced by long range magnetic ordering. In figure 5.8 (c), a rare domain wall and distinct magnetic ripples within both domains were imaged. The directions of the average magnetization can be unambiguously drawn from the ripples, from which it can be inferred that the wall is a 90° Néel wall. As in the thinner film, the characteristic size of the magnetic ripples was comparable to the size of the plateaus of the crystallites. The crystallites were smaller in this case than in the 4 nm-thick film. This is supported by the Fourier transform of the MFM image, which showed a four-fold symmetry similar to the 4 nm case, but contained significant high-frequency components. This indicates that the ripples themselves were formed by the crystallites.

The 90° wall itself is quite interesting. As shown in figure 5.8 (d), the measured peak-to-peak width of the Néel wall is about 60 nm so that the domain wall width was less than 40 ± 1 nm, assuming an arctangent magnetization profile. This provides a stark contrast to the results in [60], which reported a 180° Bloch wall with a 210 ± 40 nm width for a Fe single crystal. The origin of this difference is still under study, but the data presented here may reflect a reduction of the effective exchange interaction because of the presence of Fe-depleted regions that separate the crystallites.

14 nm Fe on MgO at high temperature (400 °C)

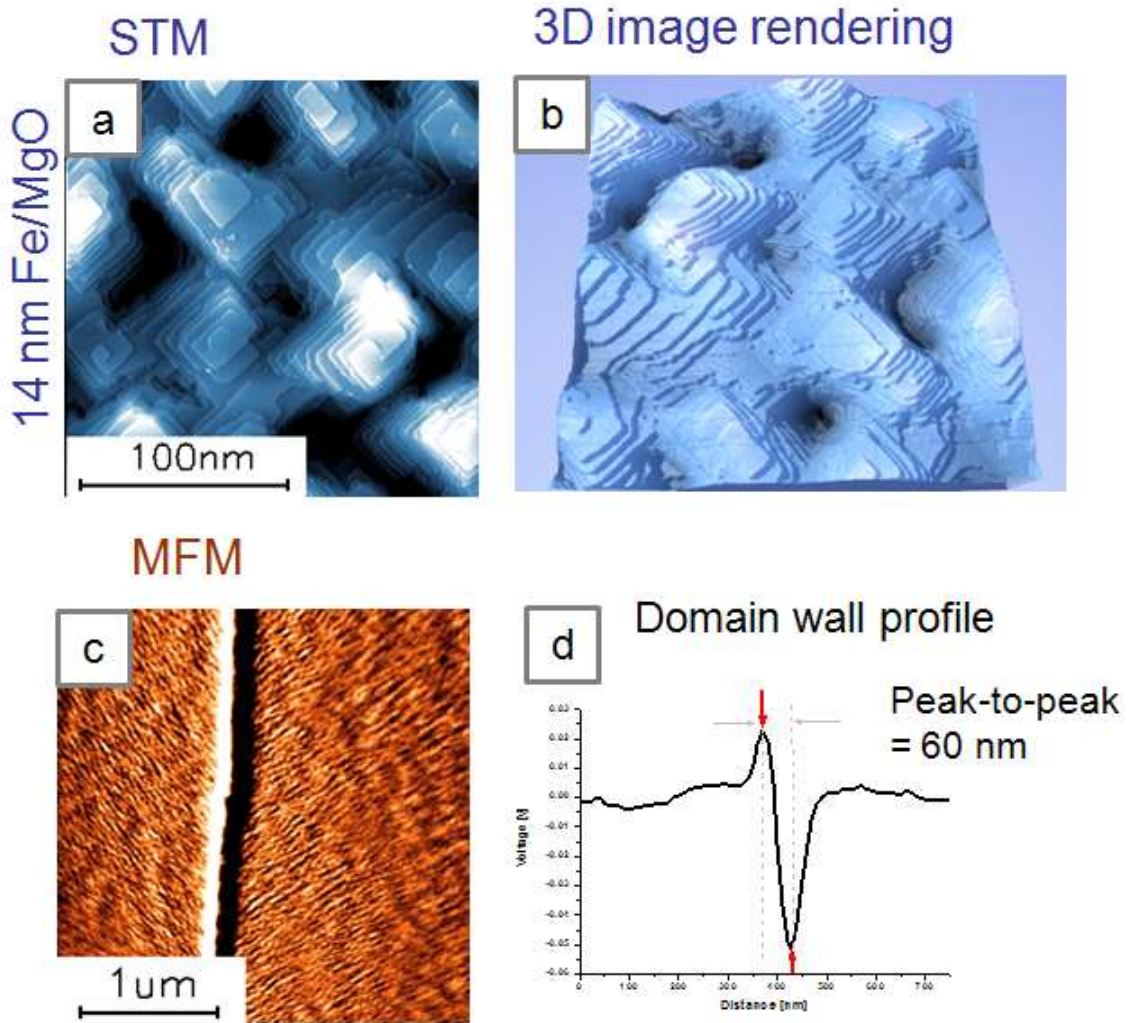


Figure 5.8 STM/MFM images of 14 nm Fe thin film grown on MgO (001) at 400 °C: (a) STM image, (b) its 3-D implementation, (c) MFM image and (d) the cross-section across the domain wall. 14 nm thick Fe formed pyramid-like islands, similar to the thin film. Magnetically, however, it had distinct features such as magnetic ripples apparent along the magnetic easy-axis of bulk Fe. These ripples show long range magnetic ordering, implying stronger coupling. A 90° Néel wall was also found in MFM.

Magnetic images with ex-situ MFM

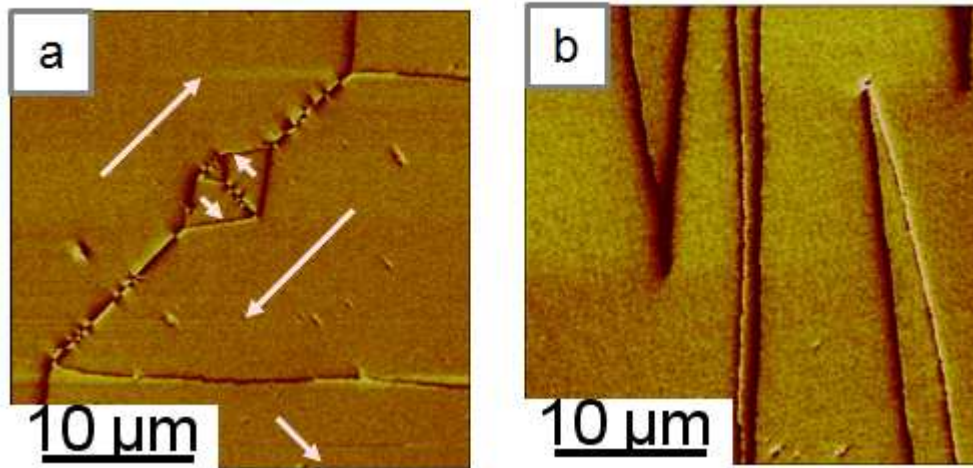


Figure 5.9 MFM images measured in ambient condition on 14 nm thick Fe films, which are grown (a) at room temperature and (b) at high temperature of 400 °C. The room temperature sample showed a variety of magnetic domain walls such as Néel, Bloch, and cross ties, while the high temperature sample had a much simpler configuration.

5.3.3 Magnetic images with ex-situ MFM

This section focuses on the large scale characteristics of the domain walls. Figure 5.9 shows MFM scans in the air of both the room-temperature and high-temperature samples of 14 nm film thickness. These images were obtained near the sample edge, where the density of domain walls was highest. The difference in complexity between the two images is obvious. In addition to Néel and Bloch walls, the room-temperature sample also formed cross-ties and Bloch lines. Néel walls are identified by distinct pairs of bright and dark contrast, while Bloch walls are

uniformly dark, and cross-ties are high-contrast triangles that emanate transverse to a Néel wall. The presence of cross-ties may be attributed to some deviations in the orientation of grains grown at room temperature, which allowed magnetization along directions transverse to the crystal easy axis. Similarly, in the room-temperature sample, domain walls were also formed along the hard axis directions, which resulted in the very prominent 4-domain diamond configuration shown at the center. Interestingly, there seems to be a systematic order in the type of walls that appeared along the hard axis. Néel walls were favored along roughly the $[110]$ direction, while Bloch were favored along the $[1\bar{1}0]$. This may be symptomatic of an uniaxial anisotropy along the $[1\bar{1}0]$ direction, which favored the creation of Néel type walls. The exact origin of this asymmetry is unclear but probably arose from the unintended texturing caused by a slight off-normal incidence of the Fe beam during deposition.

The high-temperature sample was significantly simpler. The lack of cross-ties in the high temperature growth can easily be understood by recalling the improved crystallinity of the films, which suppressed magnetization in directions other than the $[100]$ and $[010]$. Also, the domain walls depicted in the image were not straight and did not form fixed angles with one other. This implies that strained walls formed on the sample, which may be attributed to the fact that the surface was comprised of crystallites as opposed to a perfectly flat film. The image also reveals a double wall, comprised of Bloch and Néel combinations, on the right side of the image. Double walls are hard to sweep away with applied magnetic fields because of the canceling effects of the similarly oriented domains on either side. Thus, the double wall remained stationary with an applied field. The presence of these walls may explain

the observed increase in the coercivity of these films, as well as some of the artifacts such as the knee [59] in the magnetization curves.

5.3.4 Post-annealing effect

Lastly, this section will explore the effects of post-annealing. Thin Fe film less than 4 nm was deposited on a well-prepared MgO (001) substrate at room temperature and then annealed at 400 °C for 30 minutes. In figure 5.10 (a), the topography image exhibits a well-oriented crystalline structure with 4-fold symmetry. Atomic steps are also apparent in STM. The MFM image of (b) reveals complex magnetic structures with checker board patterns. These characteristics are more similar to the high temperature sample than to the room temperature case. Therefore, one can conclude that the post-annealing had an effect on morphology similar to that of the deposition temperature.

Post annealing effect

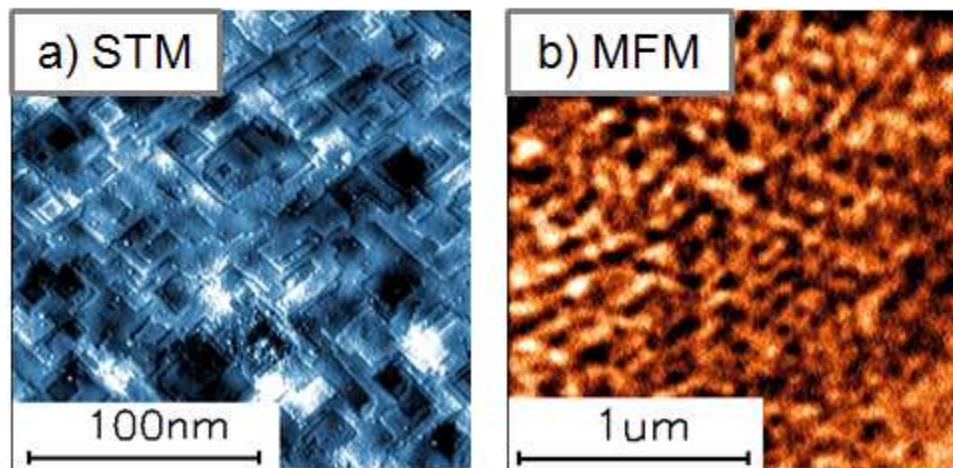


Figure 5.10 STM and MFM images on the Fe thin film (< 4 nm thick), which was grown on MgO (001) substrate at room temperature and then annealed at a high temperature of 400 °C for 30 minutes.

5.4 Conclusions

To summarize, the experimental results presented here related the magnetic structure of Fe (001) grown on MgO(001) with the topography at atomic length scales. This suggests that high temperature growth provides energy for the Fe atoms to organize into highly crystalline pyramids with plateaus on the order of 50 nm. At low coverage, less than 30 monolayers or 4 nm, the magnetic coupling between the islands is weak, which leads to complex magnetic patterns with an in-plane magnetization. With increased thickness, the stronger cooperative coupling among the grains causes a film to exhibit very large domains with magnetic ripples that follow the crystallographic easy axis. There is no evidence to suggest that domain

walls are formed within the individual islands. By contrast, low temperature growth produces a random distribution of grains that allows domains to form along the off-axis directions. Such domain walls are comprised of a rich variety of Néel, Bloch and cross-ties with interesting characteristics. By extension, these results could explain the observed differences in coercivity and magnetization curves with sample preparation as well as the increased tunneling magnetoresistance with annealing. Hence by judicious sample preparation, it may be possible to tune the local magnetic properties such as switching fields and current induced local magnetization reversal. Control of these properties, after all, is the key to making functional spintronic devices.

| Fe film grown on MgO (001) | | STM | MFM |
|----------------------------|--------------------------|--|--|
| Room Temperature | Thickness of 0.5 – 14 nm | Small grains with random crystalline distribution | Little or no magnetic contrast |
| High Temperature (400 °C) | Thin film (4nm) | Well-defined crystallographic islands with atomic terraces | - Weak magnetic coupling |
| | Thick film (14nm) | | - Complex patterns with an in-plane magnetization - Stronger cooperative coupling - Very large domains with magnetic ripples along the easy axis |

Table 5.1 The summary of the salient features from our observations.

Chapter 6

STM/STS Study on the growth of Fe-MgO-Fe system on MgO(001) substrate

6.1 Introduction

Since tunneling magnetoresistance (TMR) up to 180% was reported in a single crystal Fe/MgO/Fe system in 2004 [6, 7], magnetic tunneling junctions (MTJs) based on MgO have been actively investigated. Among the longstanding problems in this investigation has been the discrepancy between the predicted TMR (>1000%) [8] and observations that fall well below the prediction, at <200%. Several possibilities that may account for the large discrepancy include the possible existence of structural defects or vacancies within the barrier [6], Fe oxides at the interface [61], and the existence of non-coherent tunneling channels due to oxygen deficiency in the MgO layer [62]. These potential problems are further aggravated by the growth mode of Fe on MgO. From this and other research [28, 63], it has been established that Fe grows on MgO in the Volmer-Weber manner; that is, the Fe film forms grains, which leads to complex morphology on the surface. Because of the inhomogeneity, the system contains a variety of structural defects, as well as chemical impurities that can cause electron scattering, lowering the TMR effect. The purpose of this work is to examine the relationship between the topography and the local density of states (LDOS), in order to explain the electronic inhomogeneity of Fe/MgO and MgO/Fe. This study

uses the STM as a tool for simultaneously imaging the surface topography and measuring the spectroscopy with a spatial resolution at the Angstrom level at various stages of growth.

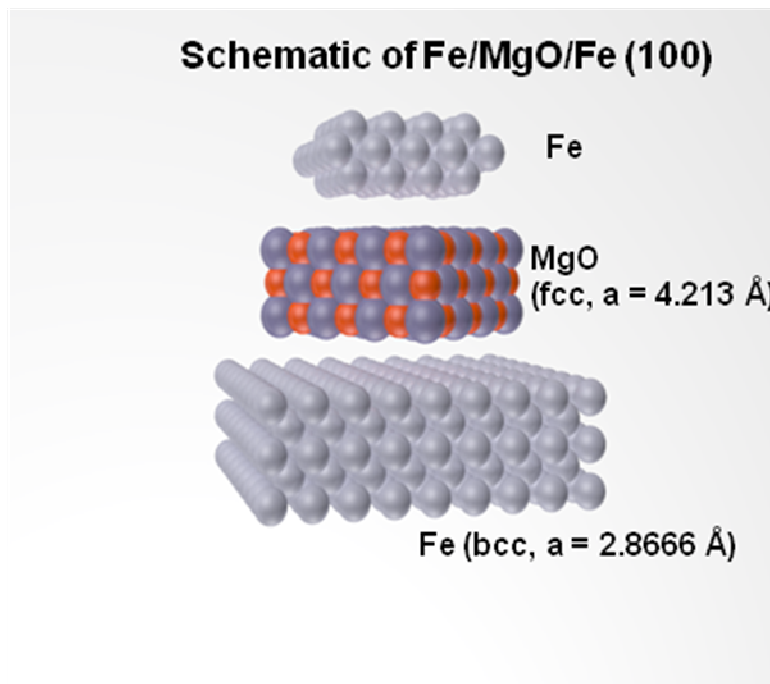


Figure 6.1 The schematic of the Fe/MgO/Fe (100) epitaxial system. Fe has a bcc structure with a lattice constant of 2.86 Å and MgO has a NaCl-like fcc structure with a lattice constant of 4.21 Å. A thin MgO film is sandwiched by two Fe structures, with a good lattice match (less than a 6 % mismatch).

6.2 Experiments

The experiments discussed in this chapter were performed in a dual chamber Omicron Surface Analysis system with base pressure lower than 4×10^{-10} Torr. The analysis chamber was equipped with a low energy electron diffraction (LEED), Auger electron spectroscopy (AES), a scanning probe system with atomic/magnetic force microscopy (AFM/MFM), and STM/STS. The preparation chamber was connected by a gate valve, and included an Ar⁺ sputtering source, electron beam evaporators with Fe and MgO sources, and a sample heating stage. A single crystal MgO (100) was used as the starting substrate, and subjected to several cycles of sputtering and annealing at up to 950 °C until the Auger carbon peak was below the noise level and the surface roughness (rms) as measured by AFM was less than 0.6 nm (the details of sample preparation is described in chapter 5.2). Based on chapter 5, the Fe thin film was grown at the substrate temperature of 400 °C and at a slow rate of 1 Å/min. For any given surface, the current (*i*) and differential conductivity (*di/dv*) were measured against bias voltage (*v*) curves at the same time with topographic imaging. All measurements were performed at room temperature using cleaned, electrochemically etched tungsten tips. In obtaining the STS data, the tip height was first stabilized with feedback by setting the tunneling current at 0.3 nA at a bias voltage of 1 V. Once stable, the feedback was turned off as the current (*i*) and differential conductivity (*di/dv*) were measured within the voltage range of +/- 1 volt at increments of 2 mV at each of the 90,000 (300 × 300) data points that comprised each STM image. A lock-in amplifier with 40 mV modulation was used to obtain the differential conductivity.

STM Topography

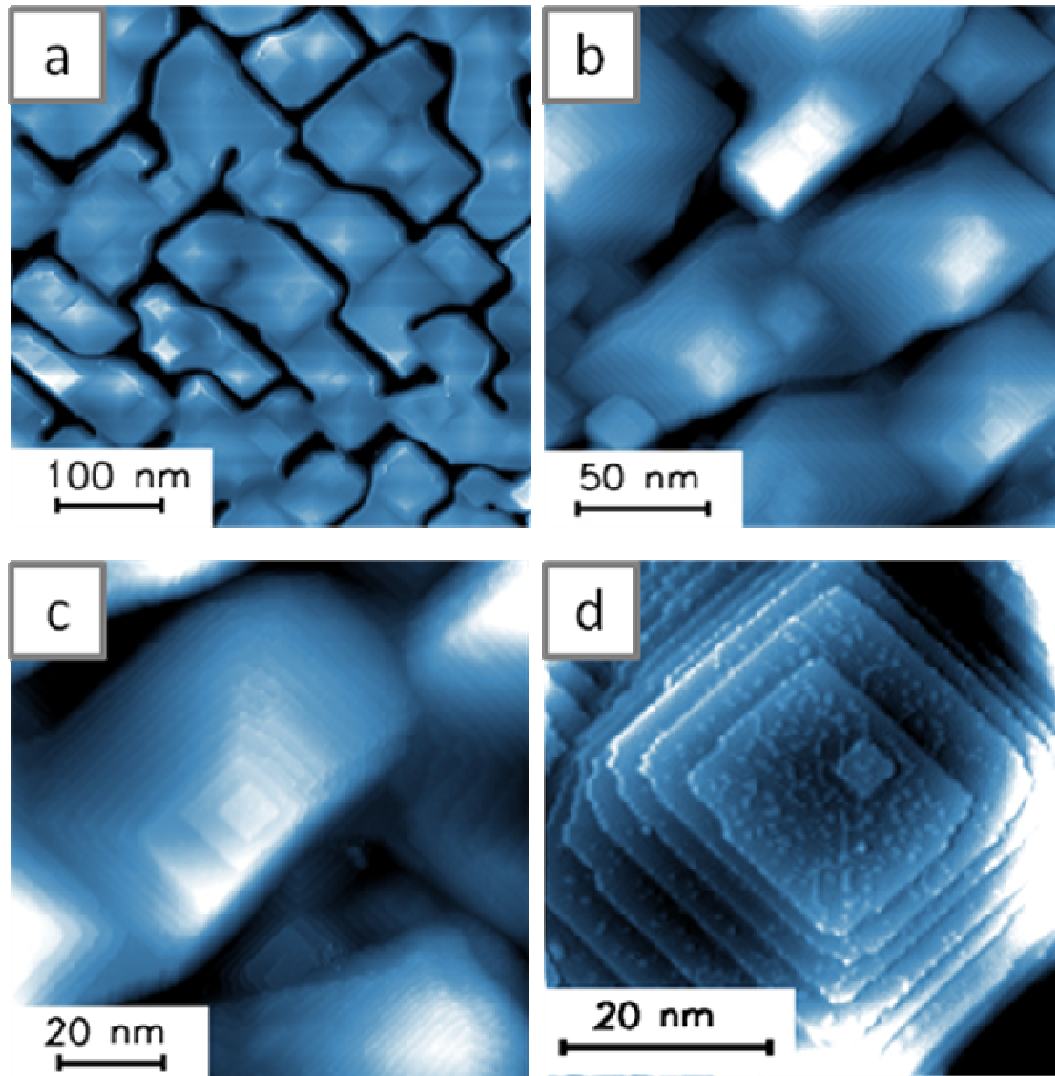


Figure 6.2 STM images on a 25 nm thick Fe film grown on a cleaned MgO (001) substrate at a deposition temperature of 400 °C. The Fe grew into pyramid-like grains, which have crystallographic registry with the underlying MgO single-crystal. The scan areas were (a) $500 \times 500 \text{ nm}^2$, (b) $200 \times 200 \text{ nm}^2$, (c) $100 \times 100 \text{ nm}^2$, and (d) $50 \times 50 \text{ nm}^2$.

6.3 Results and Discussion

6.3.1 STM/STS study of Fe film on MgO (001)

The thin Fe films on MgO (100) grew into pyramid-shaped grains formed by terraces separated by single atom high steps [28, 63]. The grains were preferentially rectangular, reflecting the 4-fold crystalline symmetry along $\langle 100 \rangle$ directions. These topography features are presented in figure 6.2. Large area STM images such as those in figure 6.2 (a) and (b) reveal that the top plateaus on islands vary between 10 to 50 nm in width, and that the islands are separated by trenches that are several nanometers deep. Single atomic steps with 0.14 nm heights are resolved clearly on the small area scan images of (c) and (d). In particular, the terraces of figure 6.2 (d) are generally flat but roughened somewhat by local variations less than the step height. This is probably due to slight dislocations of Fe atoms because they have similar voltage dependence on the spectra. The widths of the terraces vary from tens of nanometers (the first few terraces) to negligibly narrow widths with very steep slopes formed by step bunching. A very deep trench is also visible at the bottom right corner of the image.

STM and STS were measured simultaneously in the same area of figure 6.2 (d). As revealed in figure 6.3 (a), the STM image shows a variety of surface features such as the flat terraces, single steps, step-bunches and a deep trench. All of these features exhibit their own unique conductance spectra. Indeed, the corresponding STS reveal the highly non-homogenous local electronic density of states of the surface. Within the field of view, one can identify five areas that can be considered to have distinct conductance properties. The conductance (di/dv) map in figures 6.3 (b) and

(c) show clear differences in contrast at various locations on the surface, which themselves depend on the applied bias voltage. For example, at +400 mV (figure 6.3 (b)), the terraces (T) are bright, the bottom of a trench (B) is very dark, and the single step edges (SE) and step-bunched slope region (SL) have intermediate contrast. By comparison, for 1 V bias voltage (figure 6.3 (c)), the opposite contrast exists: namely, the terraces are dark, and bottom of a trench is very bright. It is also possible to identify a region (W) that has a clear voltage-dependent conductance, yet displays no distinctive topographical features.

To better understand the aforementioned differences, the current (i) and conductance (di/dv) curves were measured as a function of sample bias. From these, it was informative to derive the normalized conductance $\{di/dv/(i/v)\}$ curve by dividing these two curves. The normalized conductance curve is commonly associated with the local density of states [41, 64], discussed in chapter 4. The salient information is summarized in figure 6.4. Each curve depicts the average of several hundred curves at the equivalent points on the surface. Specifically, the curve (T) was obtained by averaging all of the spectra curves for all points on the terraces, while (SE) was obtained on the average of all step edges, which are outlined with a red line in figure 6.3 (a). The (B), (SL) and (W) devote areas are bounded by the perimeters drawn in the image. The variations in the conductance can be attributed to the local density of states of the Fe surface, since tungsten, which has a featureless density of states near the Fermi level, was used as a tip.

In the images, the spectrum at the terrace region (T) shows a pronounced peak at +0.3 eV bias, which implies an enhanced density of unoccupied states at this

energy above the Fermi level. This peak is generally attributed to the surface state of the bcc Fe (100), despite some disagreement regarding the exact position of the peak [31, 65-69]. The spectrum at the step edges (SE) is similar to the terrace, except that the peak is reduced and the width is slightly broadened. At the sloped region (SL), where step bunching occurred, the Fe surface state peak disappeared altogether. These observations agree with the findings of Bischoff *et al.*, which showed that surface states are quenched at the steps [70].

There are regions on the surface that appear to be highly depleted of Fe. In particular, the bottom of the trench in figure 6.3, denoted as region B, appears to be one of those areas. The spectra, which were taken to the right of the step-bunched (SL) region, exhibit markedly different electronic behavior from Fe. They exhibit a bandgap. Since $i=0$ at the gap, the normalized differential conductance diverges, which is why it was omitted in the $\{di/dv/(i/v)\}$ plots. The current and conductance graphs in figure 6.4 (a) and (b) show a semiconductor-like band gap of about 1 eV. The width is much smaller than the bandgap of bulk MgO, which is about 7.8 eV, so it is unlikely that the curve corresponds to the MgO substrate. However, while the exact origin of this gap remains unclear, it is likely to be due to the oxidation of Fe, which is similar to the semiconductor-like behavior observed in crystalline magnetite (110) [71]. Similarly, the influence of chemistry may be responsible for the $\{di/dv/(i/v)\}$ curve in region W. In this case, the current and conductivity spectra appear to be intermediate between the terrace and bottom cases. This suggests the formation of iron oxides, possibly giving rise to magnetically dead layers in this area.

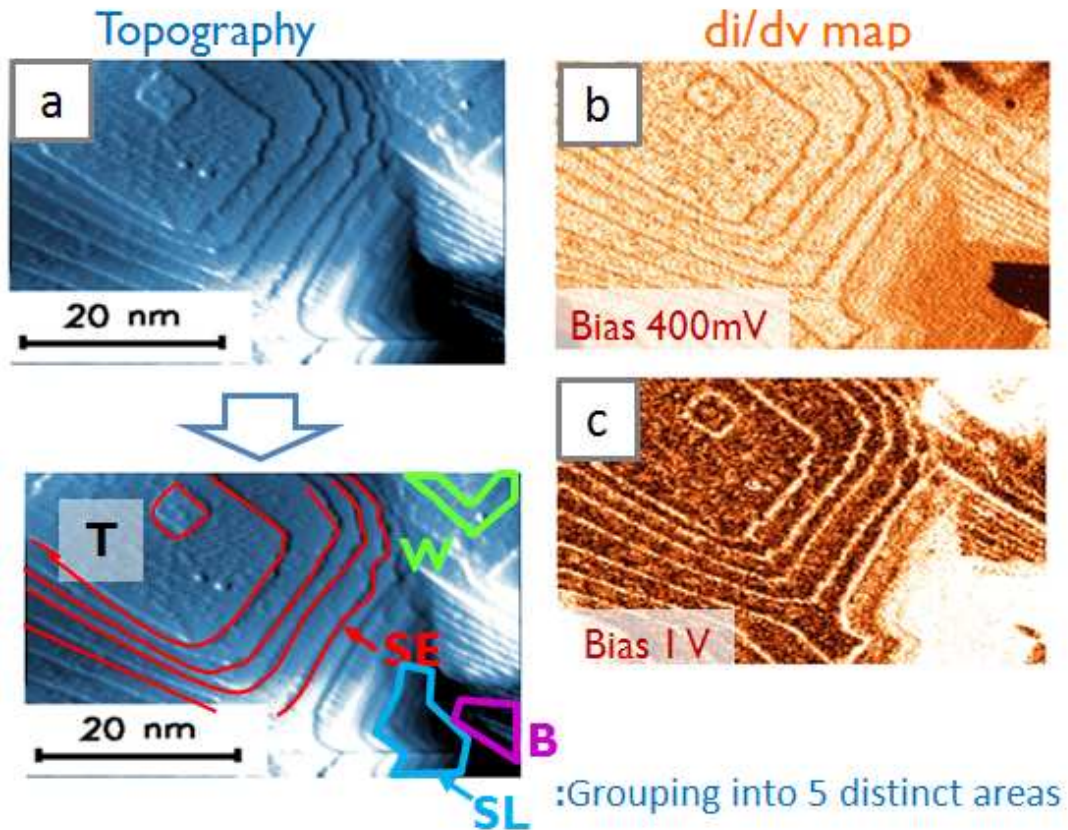


Figure 6.3 Simultaneous measurements of STM and STS on 25 nm thick Fe film grown on MgO (001) at 400 °C: (a) STM topography and the corresponding STS images (b) at +400 mV and (c) at 1V bias voltage. The STS conductivity maps have clear contrast differences in various regions. These regions can be sorted into 5 groups: terraces (T), step edges (SE), slope region (SL), upper right-handed area (W), and the bottom of a trench (B), which are labeled in the lower left-handed image.

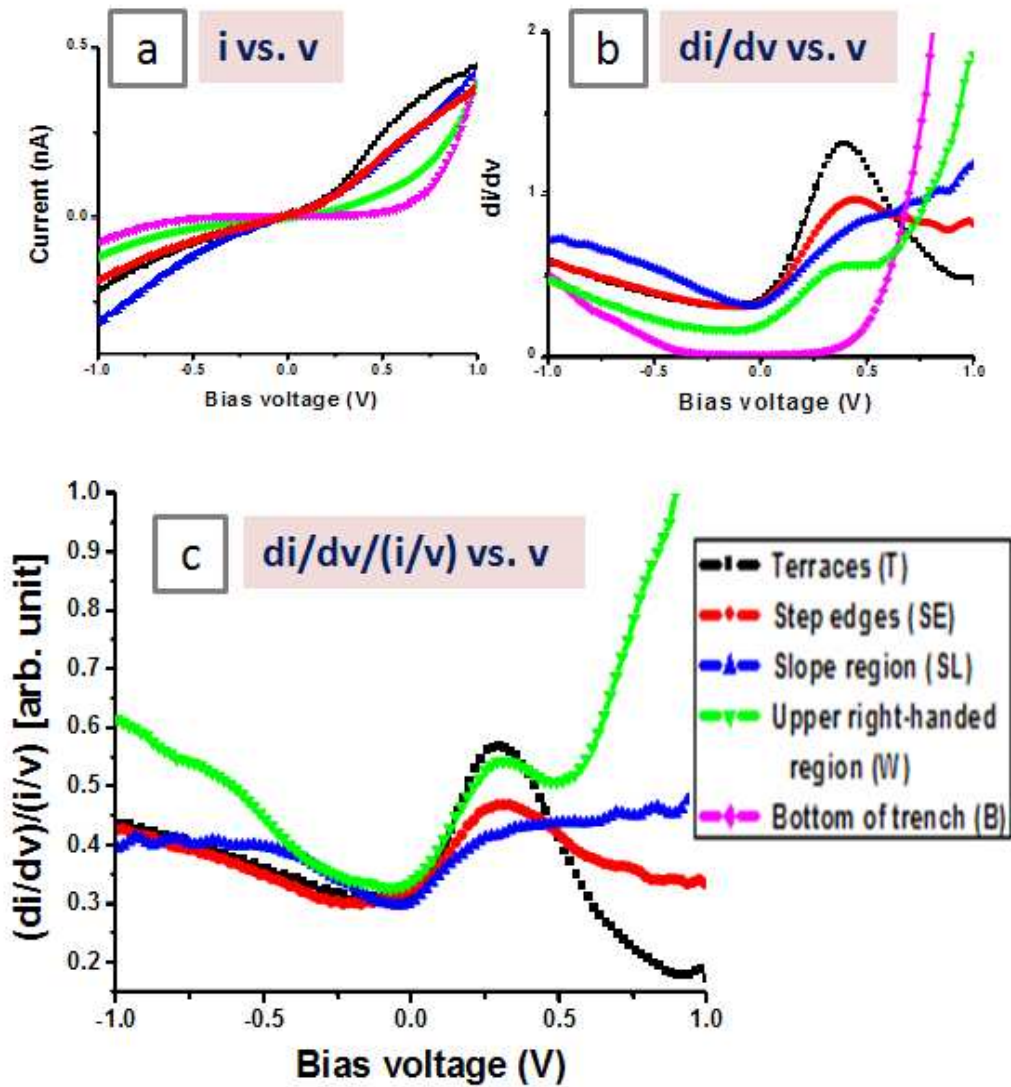


Figure 6.4 The corresponding STS data in various regions identified in figure 6.3: (a) current(i), (b) conductivity(di/dv), and (c) normalized conductivity($di/dv/(i/v)$) versus bias voltage(v) spectra.

6.3.2 MgO film on Fe thick film (001)

After establishing the properties of Fe growth on MgO, the experiment focused next on the case of MgO on Fe, using the same samples studied previously, upon which the STM and STS data was obtained. Figure 6.5 (a) shows that at ultra-thin coverage level (<0.2 ML), MgO formed small ‘droplets’ that are on the order of 1 nm diameter and about 0.1 nm thick. Larger grains formed preferentially at the step edges, although smaller diameter droplets formed on the wide terrace. The inset shows a high resolution image of the droplets on flat terrace, revealing that they formed along $\langle 100 \rangle$ crystalline directions of the underlying Fe surface, which implies epitaxial growth of MgO. As coverage was increased, more droplets formed with an additional MgO deposition that eventually coalesced to form a continuous layer. This situation is shown in figure 6.5 (b) at coverage just under 1 ML. This growth is consistent with the Stranski-Krastanov or layer-by-layer growth mode. Further deposition of MgO increased the surface roughness, and for coverage > 5 ML, the MgO obscured the underlying structure (figure 6.6 (a)). Annealing to 450 °C, however, improved the crystallinity and smoothed the film somewhat. This is evidenced by clearer periodicity in the Fourier transform of the STM image of figure 6.6 (b).

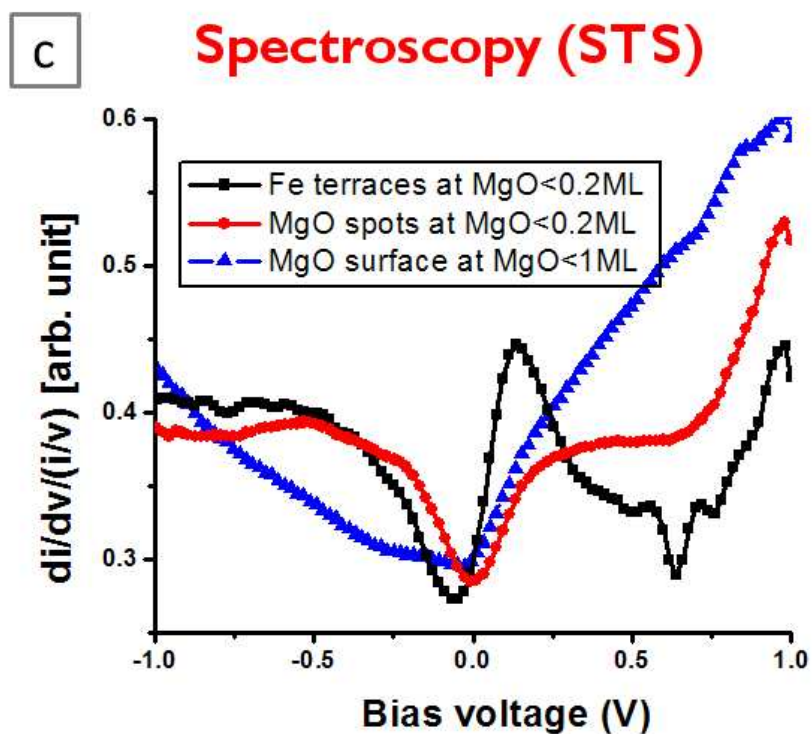
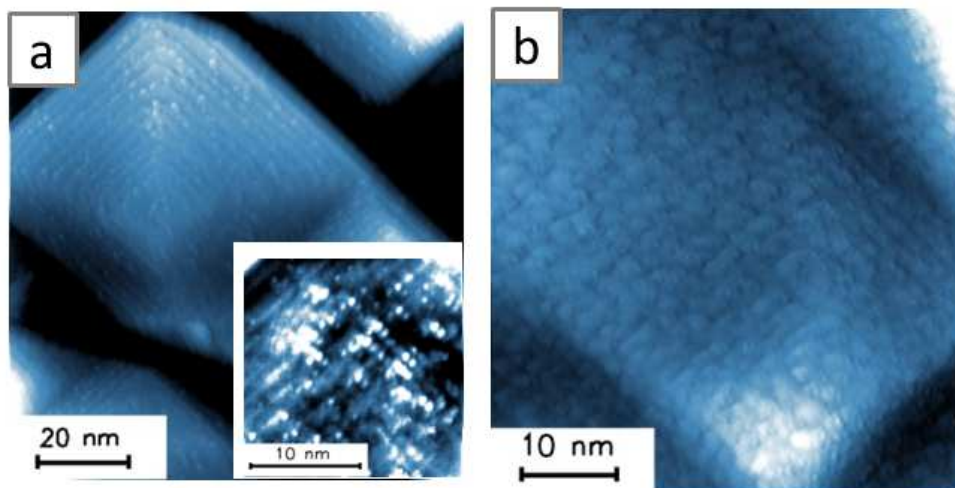


Figure 6.5 Submonolayer of MgO deposited on thick Fe (001) film: STM topography at (a) less than 0.2 ML coverage (inset: zoomed image on a top flat terrace) and (b) slightly less than 1 ML coverage, and (c) corresponding spectroscopy data.

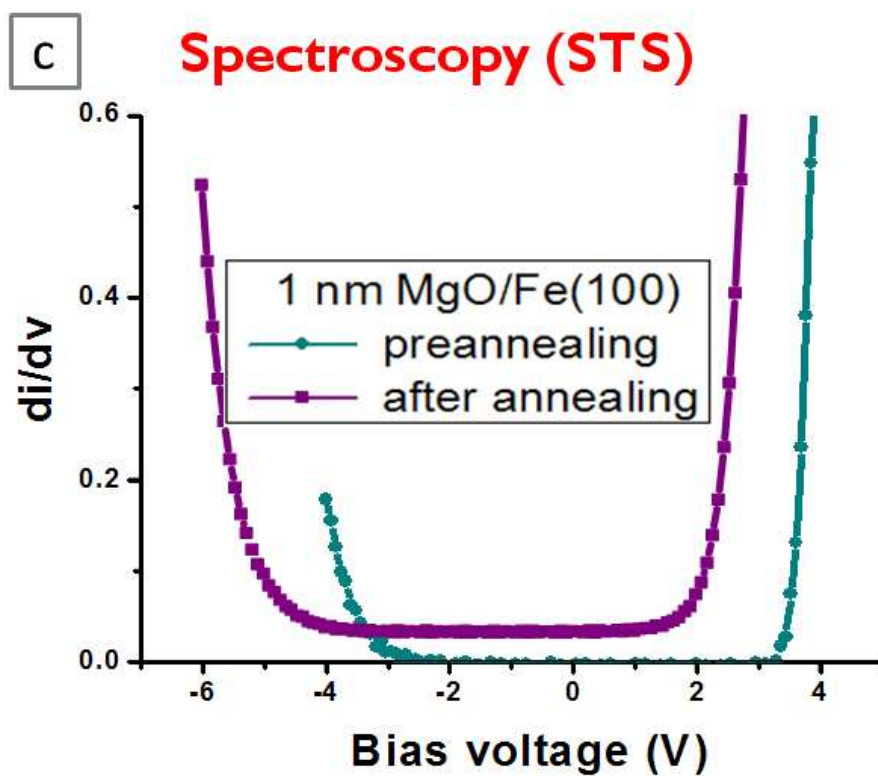
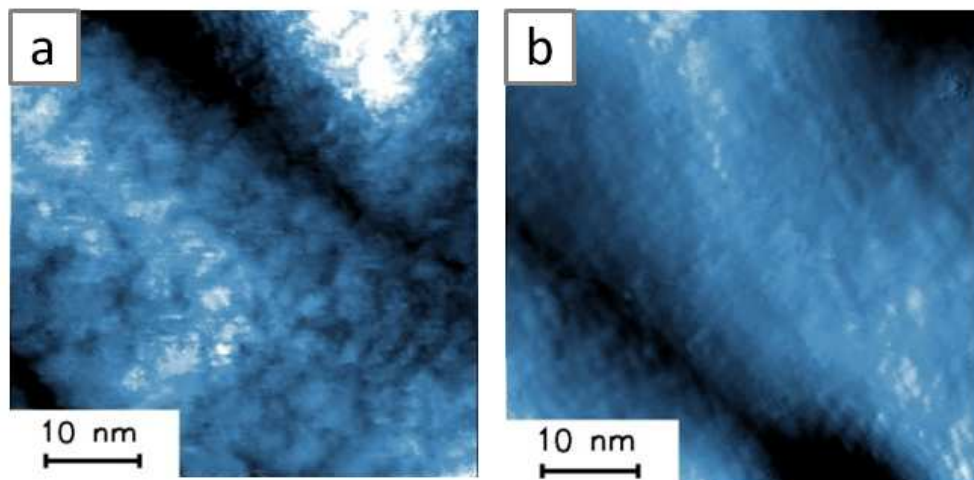


Figure 6.6 STM images on 1 nm thin MgO layer deposited on thick Fe (001) film (a) at room temperature and then (b) annealed at 450 °C, and (c) the corresponding spectroscopy data.

The corresponding STS data is shown in figure 6.5 (c). For very thin MgO (<0.2 ML), the spectra on top of the uncovered Fe atoms on the terraces showed a distinct Fe peak similar to the previous case, except that it shifted downward from 0.3 eV to 0.2 eV. The reason for the shift is not clear, although it is likely that it was simply due to tip effect [70]. Nevertheless, the surface peak diminished in the spectra taken on top of the MgO cluster on the sample surface. It was replaced by a shoulder at 0.3 eV, showing that the spectra are extremely sensitive to MgO coverage. Indeed, with additional MgO, a total coverage of slight less than 1 ML, the Fe surface state completely disappeared and what used to be a shoulder became a nearly linear increase in the states above the Fermi level. Information in the literature on the effects of submonolayer coverage of MgO on Fe is sparse, and the origin of this behavior is still under study. Yet, is the phenomenon observed in this experiment was clearly an intermediate state of the MgO from the extremely low coverage to bulk. The bulk property of MgO is shown in figure 6.6 after several monolayer coverage. Figure 6.6 (c) clearly shows the characteristic bandgap in the conductivity curves at an MgO thickness of 1 nm. The characteristics of the bandgap depend upon the crystallinity of the surface and would be affected by annealing. For this reason, the STS was compared before and after annealing. What used to be a bandgap of about 6 eV in the pre-annealed sample increased to about 6.5 eV after annealing to 450 °C for 30 minutes. This measurement is consistent with the known MgO (001) surface interband transition 6.2 eV [72] and with the observation of others that bulk-like MgO energy gap is fully established for 3 nm thick films [73] corresponding to 3ML [74]. Further annealing caused an offset of about -1 volt. This may be due to annealing

effects on the Fermi level pinning, and the shift may be induced by a change in the interfacial oxides, oxygen deficiency, and intermixing between layers.

6.3.3 Growth of Fe/MgO/Fe junction structure

As a last step in this experiment, a complete magnetic tunnel junction was fabricated using Fe/MgO/Fe (001) layers grown on a cleaned MgO (001) substrate. The first Fe layer of 35 nm thick was deposited at 400 °C, followed by the evaporation of MgO up to 3 nm thick at room temperature. The structure was annealed up to 450 °C for 30 minutes. Finally, a small amount ($< 0.5 \text{ \AA}$) of Fe was deposited on top at room temperature. The high resolution STM image of the surface of the finished 3-layer structure is shown in figure 6.7 (c). As examined previously, the first thick Fe film (35 nm) formed well-oriented grains with large flat plateaus, which are shown as large background islands surrounded by deep trenches. The second MgO layer (3 nm) covered the Fe surface more or less uniformly, and rounded the sharp edges of Fe islands, which is clearly exhibited in the large area scan images such as figures 6.7 (a) and (b). In the image in figure 6.7, the MgO layer is shown as aligned stripes separated by around 6 nm width. These stripes seem to be aligned along the [110] direction of the underlying Fe crystal, because some of the topmost Fe islands have a pyramid shape with defined edges along [100] and [010], crystalline directions, and MgO stripes form 45° rotation from the edges. Thus, the stripe patterns support the layer-by-layer growth of MgO indirectly. The topmost Fe layer ($< 0.5 \text{ \AA}$) formed a distribution of oriented grains with an average size of 5 nm and a size distribution from 3 to 10 nm. The STM image shows two varieties of the topmost

Fe grains: one is the small pyramid-like crystalline structure, and the other is a rounded grain with a slightly larger size. Regardless of shapes, most of the grains are well separated and are thus electrically and magnetically decoupled. Since the first Fe thick film was deposited, the MFM shows the same magnetic patterns with large multi-domains and strong magnetic ripples, as shown in figure 6.7 (d), which is similar to the images in Chapter 5. This reveals that a small amount of the MgO layer and the topmost Fe layer do not affect the strong magnetic configuration of the first Fe layer. Lastly, in order to get the information of surface chemistry and tunneling states, the STS measurement was taken from the top of this surface, but no distinct spectra were found between on topmost Fe islands and the bare MgO surface. This is due to the MgO insulating barrier forming a semiconductor-like behavior on spectra, such as a large bandgap with a rapid increase above/beyond the energy of the bandgap.

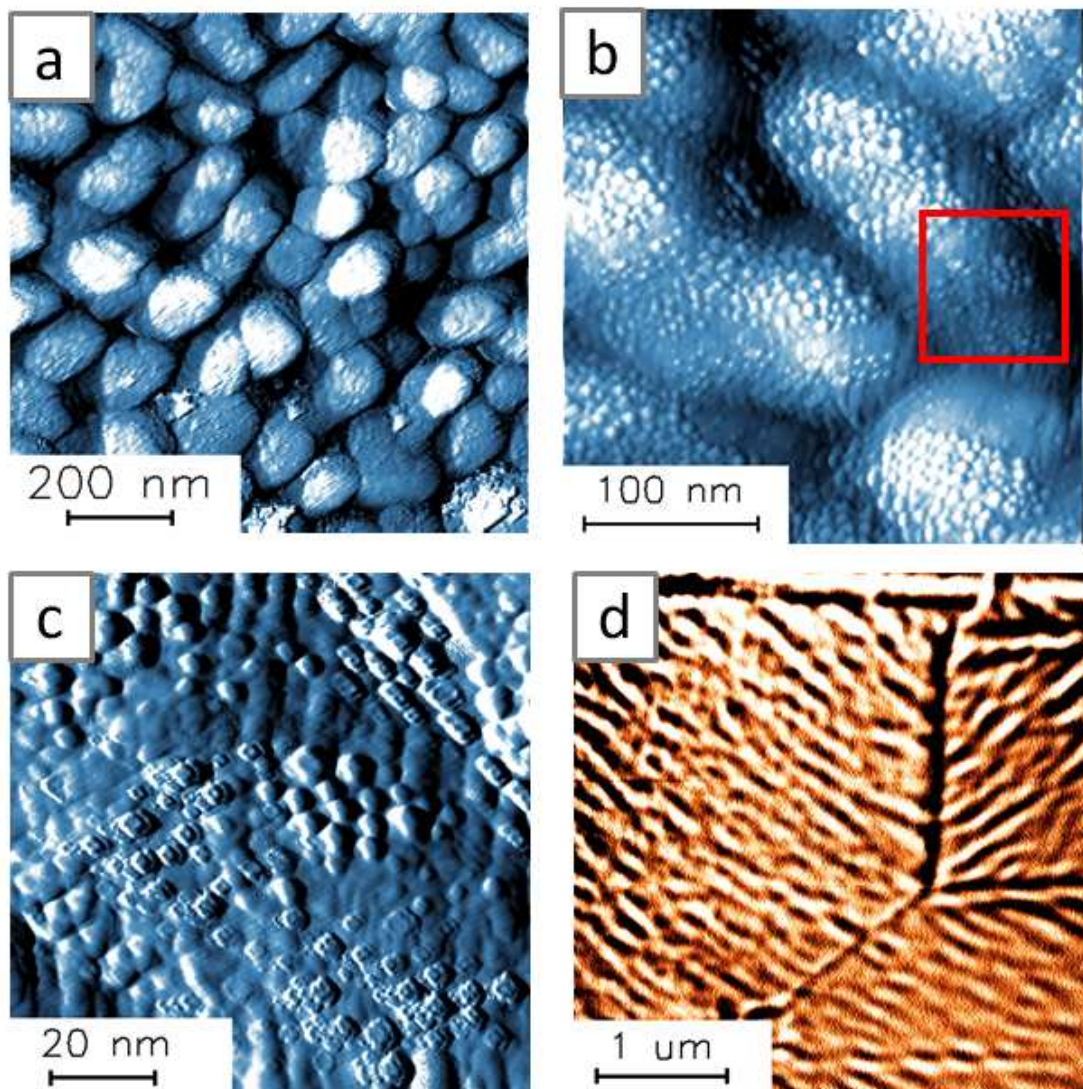


Figure 6.7 STM/MFM study of Fe ($< 0.5 \text{ \AA}$)/ 3nm MgO/35 nm Fe structure grown epitaxially on MgO (001) substrate. STM images with increasing resolution: (a) in large area of $1\mu\text{m} \times 1\mu\text{m}$ and (b) $300\text{nm} \times 300\text{nm}$, and (c) a high resolution image of $100\text{nm} \times 100\text{nm}$ which is the zoomed scan of the square mark on (b). The high resolution image (c) clearly shows rectangular-shaped islands on the topmost Fe film. (d) MFM reveals multi-domain structures with well-ordered ripples, which were formed from the bottom thick Fe film but not influenced by MgO and the topmost Fe films.

6.4 Conclusions

Using scanning tunneling spectroscopy and microscopy, local density of electronic states were correlated with the topography of Fe on MgO and MgO on Fe. The growth of Fe on MgO was Volmer-Weber or island formation that led to an electronically inhomogeneous surface. Fe (100) electronic surface states were observed on flat terraces, which diminished at the step edges, and bandgaps were observed in some deep trenches that separated the islands. MgO on Fe (100), on the other hand, grew in the simpler layer-by-layer mode. The electronic states evolved as a function of thickness from less than one to several monolayers. The bulk-like MgO behavior with more than 6 V bandgap was found for the thickest films (~1 nm). However, the spectra for very thin MgO depended upon whether it was measured on top of Fe atoms or on the MgO grains. At one monolayer, the measured density of states was different from either the very thick or very thin MgO, which suggests the possibility of an interfacial layer distinct from the Fe (100) or MgO (100) surfaces. The observed local inhomogeneity may account for the reduced TMR of these systems.

Chapter 7

Implementation of Spin-polarized Scanning Tunneling

Microscopy on single-crystal chromium (001)

7.1 Introduction

Spin-polarized scanning tunneling microscopy (SPSTM) is a technique for observing magnetic structures down to the atomic level [75]. Unlike MFM, which detects the stray magnetic field from the sample, SPSTM directly measures the abundance of an electron's specific spin orientation at a specific point on the surface. Thus, MFM is an extremely valuable tool not only as a means to image magnetic structure at atomic length scales, but also a means to map out the majority and minority spin status on the surface. In practice, MFM uses a magnetically oriented tip on the conventional STM setup. The tunneling current measured using this device includes the filtering effect associated with the electron spin variation between tip and sample. However, while potentially useful, SPSTM is non-trivial and requires very stringent conditions to operate. By its nature, it is extremely sensitive to the exact condition of the tip and sample, and the results are thus often convoluted by non spin-related influences on the electronic structure, such as from step edges or submonolayer contaminations. Thus, SPSTM experiments are valid only when conducted under ultrahigh vacuum conditions and on well-characterized substrate

surfaces free of impurities. Because of their difficulty, SPSTM measurements have been performed in only a handful of laboratories in the world, most notably at the Weisendanger lab in the University of Hamburg. The aim of this work was to develop this capability in the lab and integrate it with the Omicron system. This research focused on the well-known surface chromium (001), and later excelled these measurements to Permalloy.

The (001) surface of single crystal chromium is an ideal sample for implementing SPSTM because of several attributes that make the observation of atomic-scale spin variations somewhat easier. Chromium is a topological antiferromagnet, which means that the magnetization lies within the surface plane and changes direction by 180° between adjacent terraces separated by a monoatomic step [76]. This type of magnetic structure offers several important benefits. First, the magnetization of one layer is cancelled by the next, so it produces no stray field due to the antiferromagnetic configuration. Conversely, there is no dipolar interaction between tip and sample that can destroy the intrinsic domain structure of the sample. Second, the magnetic domain size is determined by the terrace width of the sample. On the wide steps, for example, the domain width is commonly around tens of nanometers, and easily detectable by STM. Third, because of its alternating magnetization between adjacent planes, the sample surface provides an unambiguous magnetic background structure to immediately test the magnetic tips. Spin polarized tips would reveal alternating bright and dark contrast as they scan across adjacent monolayer step terraces [77].

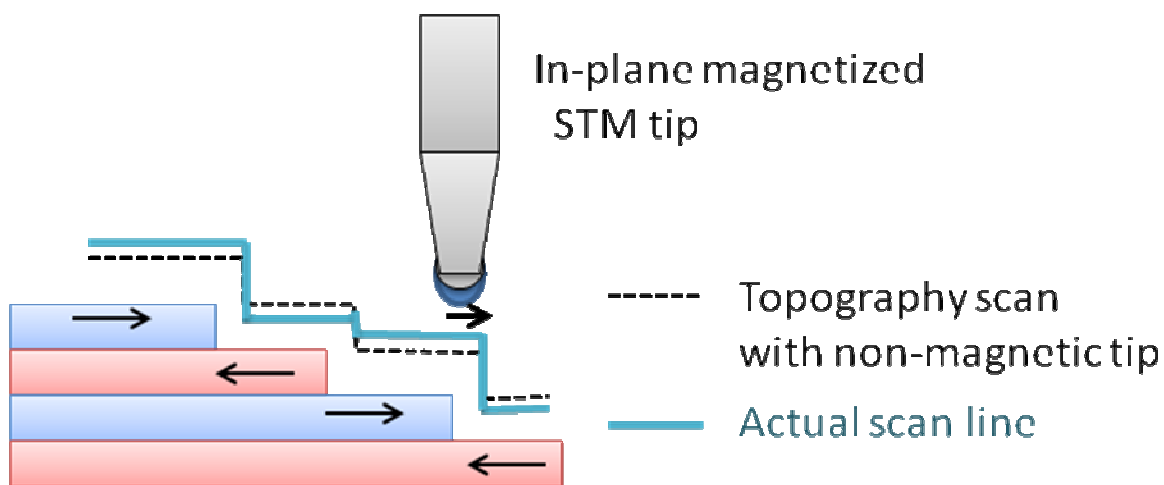


Figure 7.1 Overview of how spin-polarized STM works on a topographically layered antiferromagnetic sample such as chromium by using the difference between spin polarized and non-polarized tips. With a non-magnetic, non-polarized tip, the height of each single step would be identical (in the case of chromium, height of 1.4 \AA) since the tip does not distinguish between the alternating antiferromagnetic alignment of all the layers. However, with a spin-polarized tip, the tunneling current is modulated by the spin orientation between the probe and surface, so that terrace with favorable (parallel) spin orientation appears closer than those that are antiparallel. This difference in the tunneling current induces a vertical shift as an imposed feedback loop in order to maintain the set current while scanning.

However, the advantages of Cr (001) come with at the price of extensive surface preparation procedures. Oxygen and nitrogen are the main contaminants of the system and come from either the surface or migrate from the bulk. It requires significant effort to prepare the surface with a sufficiently low impurity level and high crystalline order to make it suitable for spin-polarized STM. Therefore, an essential point of this study is to provide the detailed protocols for making Cr (001) surfaces suitable for SPSTM while demonstrating spin-polarized tunneling on this sample.

7.2 Spin-polarized STM

As explained previously in Chapter 4, the tunneling current for two ideal metals separated by a thin insulating barrier can be approximated as:

$$I = \int_{-\infty}^{\infty} dV |\mathbf{M}(E)|^2 \rho_T(E - eV) \rho_S(E) [f(E - eV) - f(E)], \quad (7.1)$$

where f is the Fermi function, V is the bias voltage, \mathbf{M} is the tunneling matrix element and ρ_T and ρ_S are the density of electron states (DOS) of the tip and sample, respectively. In the limit of low temperature and low bias voltage, the equation is simplified to:

$$\frac{dI}{dV} \propto |\mathbf{M}|^2 \rho_T(E) \rho_S(E) \quad (7.2)$$

For spin-polarized metals at low bias voltage (less than a few eV), the tunneling current is dominated by elastic processes. The electron spin is preserved and spin-flip processes are suppressed during tunneling. Therefore, spin-polarized tunneling can be separated into two independent processes for spin-up and spin-down electrons.

$$\frac{dI}{dV} \propto \rho_T^\uparrow(E)\rho_S^\uparrow(E) + \rho_T^\downarrow(E)\rho_S^\downarrow(E) \quad (7.3)$$

In spin-polarized tunneling, the current depends on the relative orientation of the quantization axes of both metals. In the simplified Stoner ferromagnet model, shown in figure 7.2, the spin-up band is shifted energetically with respect to the spin-down band due to the exchange interaction. This leads to a low density of electron states for the majority spin electrons at the Fermi level, and high density of states for the minority electrons. If the two metals have the same magnetic orientation, the product $\rho_T^\uparrow(E)\rho_S^\uparrow(E)$ will be relatively small, but $\rho_T^\downarrow(E)\rho_S^\downarrow(E)$ will be large, so that the latter will dominate the tunneling current. On the other hand, if the two metals have opposite magnetizations, both products would be small, which will lead to a low tunneling current. Therefore, by measuring the dI/dV signal, one can infer the relative magnetic orientation of the tip and the sample, which strongly depends on the respective DOS.

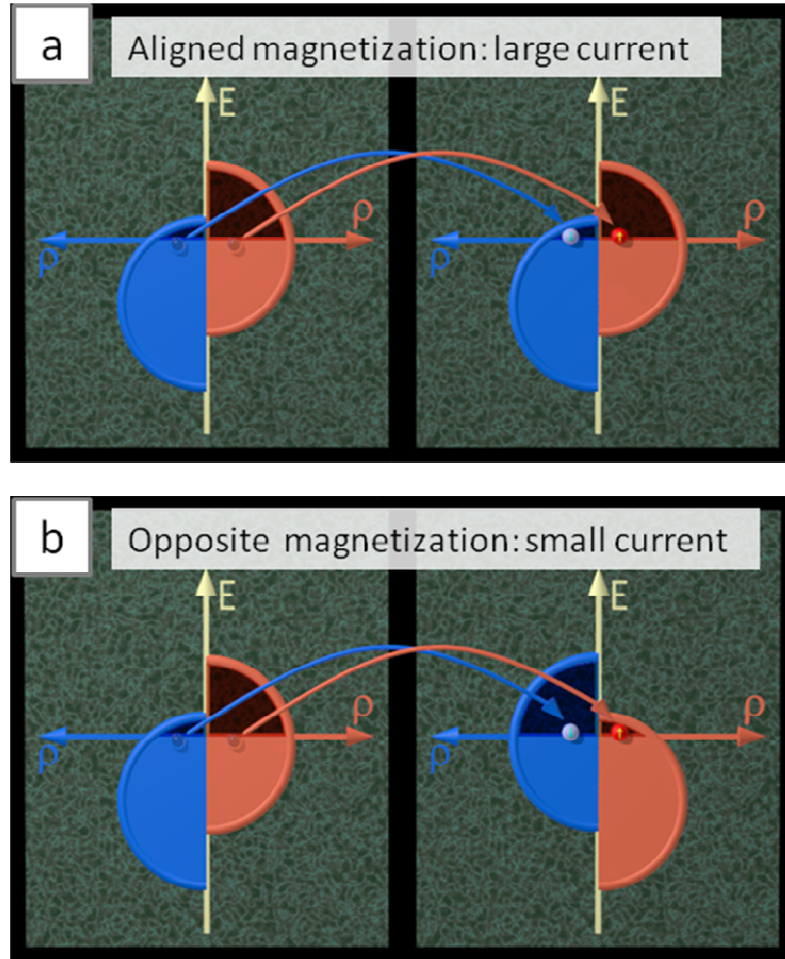


Figure 7.2 Simplified Stoner ferromagnet model for spin-polarized tunneling: the tunneling current is proportional to the product of the density of states (DOS) of a tip and sample for each spin. When the tip and sample have same magnetization, the tunneling current is represented as $\rho_T^\uparrow(E) \rho_S^\uparrow(E) + \rho_T^\downarrow(E) \rho_S^\downarrow(E)$ and induces large amounts based on the product of both high densities. By contrast, when tip and sample are magnetized oppositely, the tunneling current is $\rho_T^\uparrow(E) \rho_S^\downarrow(E) + \rho_T^\downarrow(E) \rho_S^\uparrow(E)$, in which both terms are small because of the product of high and low densities. (ρ_T (or ρ_S) is the density of electron states (DOS) of the tip (or sample).)

7.3 Experiments

7.3.1 Preparation of spin-polarized STM tips:

The key for implementing SPSTM is to properly prepare the spin-polarized tips, preparing one tip with an apex atom exhibiting a high spin polarization, and one which does not produce a strong magnetic field. Earlier tips were made from polycrystalline bulk materials such as ferromagnetic wires [78, 79], but these tips have a strong stray field and are hard to cleanse of bulk impurity contamination. To circumvent those problems, this work employed an alternative technique of using the normal STM tips coated in UHV with a magnetic thin film.

The STM tips were made from tungsten wire by electrochemical etching using a KOH solution. Each tip was heated by electron beam bombardment in UHV, at a temperature high enough to remove oxides and other contaminants without melting the apex. The tips were then coated with 5 nm of iron.

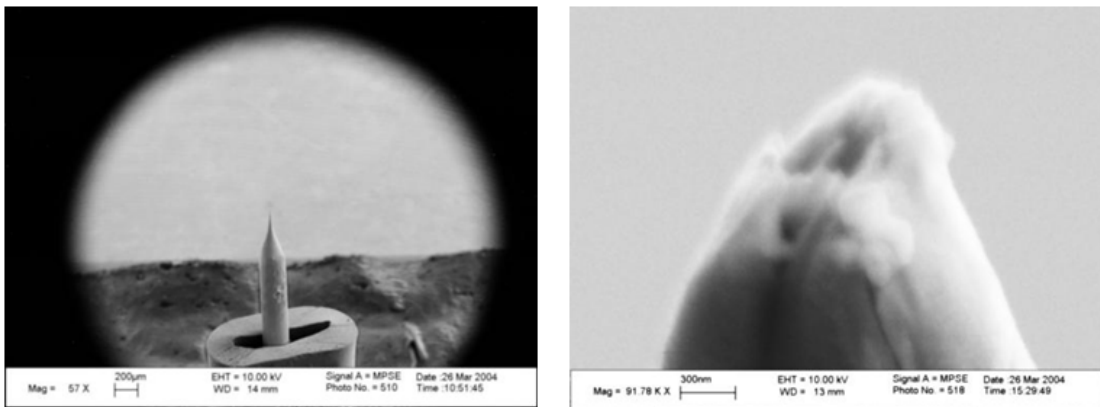


Figure 7.3 Secondary electron microscopy (SEM) images of e-beam heated and Fe-coated STM tip.

7.3.2 Preparation of the Cr (001) sample

The procedure used in this research for creating atomically clean surface of a Cr crystal is depicted in figure 7.4. For SPSTM to work, it is essential that the quality of the surface be very good and devoid of any contamination, and surface reconstruction can induce inelastic scattering of tunneling electrons and some distortions of spin information. The successful spin-resolved STM image was also obtained.

The series of AFM images in figure 7.4 show the detailed morphological evolution of Cr (001) at various stages of the preparation. The main contaminant was oxygen, which formed chromium oxide. After removing the native oxide by sputtering, new oxide grains appeared on the surface after annealing. These extra oxygen atoms came from dissolved oxygen that segregated from the bulk onto the surface. This is similar to the observations of others on Fe (100) [80]. Fortunately, these oxides can be removed by extensive sputtering and annealing until the bulk oxygen has been nearly completely exhausted. This subsequently leads to a clean chromium surface with visible single-atom steps in STM.

Prior to any form of cleaning, the AFM image of (a) was taken in air. The image shows the surface roughness and the polishing lines quite prominently. The surface at this point was covered by the native oxide, and the rms roughness corresponding to the average variation in height was 53 Å. The polishing lines were approximately 153 nm deep.

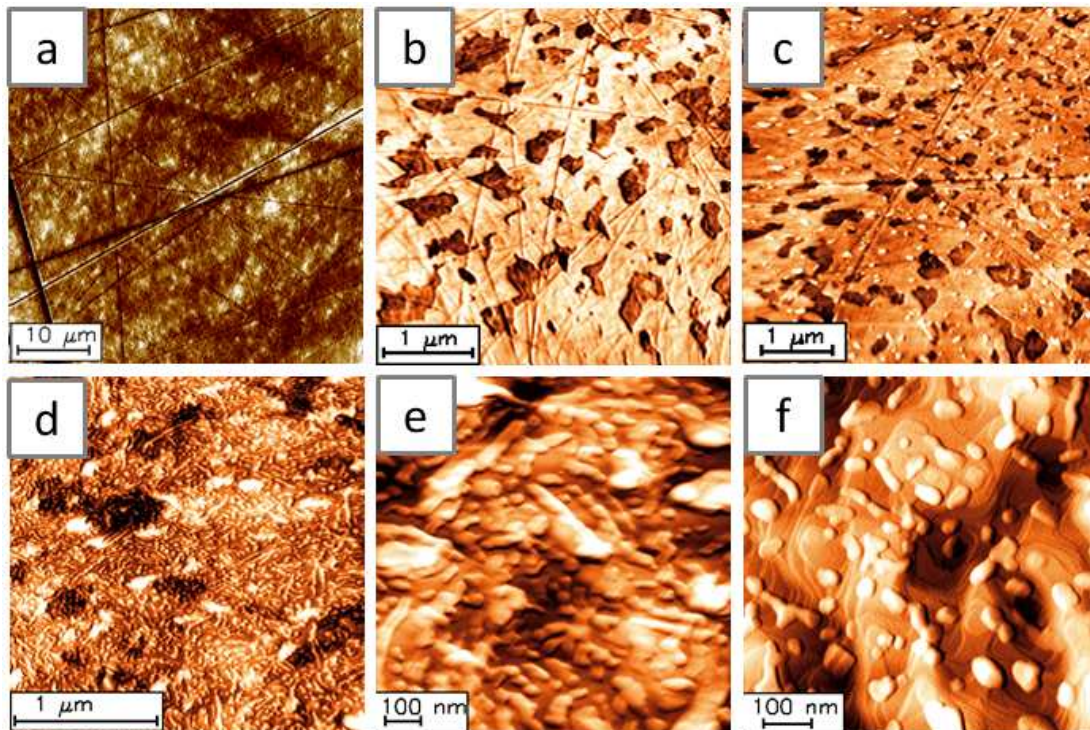


Figure 7.4 Evolution of chromium crystal surface with cleaning preparation: AFM images at various stages of repeated cycles of sputtering and annealing. (a) Initial state before any cleaning, measured using AFM in ambient condition. (b) UHV measurement after one cycle of sputtering (1.2 keV) and annealing, (c) after 2 additional cycles of sputtering and high temperature annealing (600 °C), and (d) after a total of 10 cycles at various combinations of annealing temperature, duration, and sputtering power. (e) high resolution image of (d), (f) after additional cleaning with high energy (2 keV) sputtering for 7 hours at room temperature, followed by rapid annealing (~ 10 min) at 600 °C.

Next, the sample was loaded into the UHV system and was sputtered with low energy (750 eV) Ar^+ ions. The sample was bombarded with a low current (6.6 μA) plasma for four hours and then annealed at ~ 200 °C for an hour. The AFM image in figure 7.4 (b) shows some improvement in surface quality, particularly the reduction of the depth of the polishing lines down to 2 \sim 5 nm. However, pits that were about several hundred nm wide and 5 \sim 10 nm deep were left on the surface. These were presumably remnants of the native oxide that initially covered the surface but did not show up due to the low resolution of AFM. The pits were probably a consequence of the sputtering damage. After two additional cycles of cleaning with high temperature annealing (~ 600 °C), the polishing lines were significantly diminished (\sim 1nm deep) and the oxide pits were similarly reduced (figure 7.4 (c)). However, after this step one can now observe the appearance of small grains with bright contrast peppering the surface. These grains increased in lateral dimension with longer annealing times, which strongly suggests that they were caused by miniscule amounts of oxygen that segregated to the surface from the bulk. These have distinctive features and can easily be distinguished from the original oxide, some of still persisted on the surface and were discernible at intermediate contrast. After 10 cycles of sputtering and annealing, the AFM image of (d) exhibits that much of the native oxide had been removed and the polishing lines had completely vanished. However, after this step, the density of the oxide grains from bulk diffusion had significantly increased.

Auger electron spectroscopy was used to establish the chemical makeup of the surface. The corresponding Auger electron spectroscopy showed a significant peak at the oxygen KLL electron energy, which strongly indicated the presence of residual

amounts of chromium oxide. The zoomed image, figure 7.4 (e), provides a more detailed look at (d), and it shows the fine features of these granular oxide. The height of the grains was around 10 to 20 nm, and the size varied from 50 nm to 300 nm on the long side of some of large grains. Finally figure 7.4 (f) shows the surface after more cycles of cleaning to deplete the bulk oxygen supply. After approximately 12 cycles of high energy sputtering (2 keV) for 7 hours and flash heating to 600 °C, the grains had diminished in density and the underlying Cr structure began to appear. Cr is characterized by single atomic steps and flat areas on the valleys between the oxide rounds, and flat areas of chromium were visible in the valleys between the oxide grains.

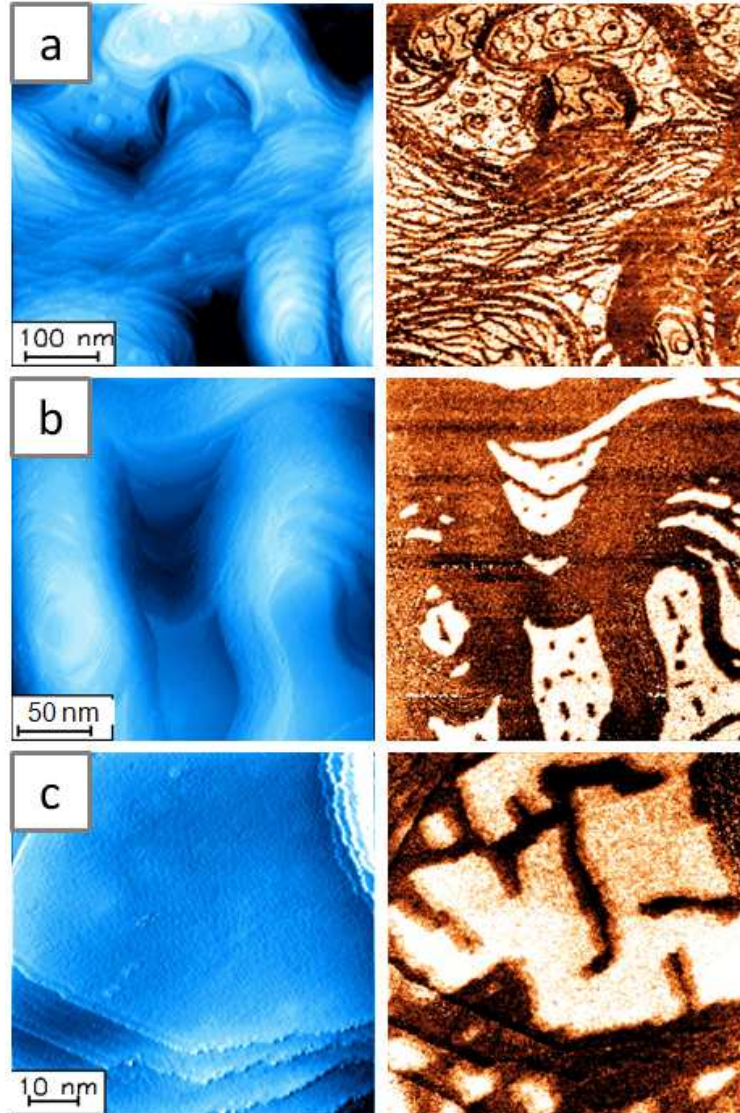


Figure 7.5 Composition of topography and local conductance of a clean Cr surface. The following images were taken after 20 cycles of sputtering and annealing to remove oxides, including the native oxide and bulk segregated types. Left panel: STM topographic images on a clean Cr (001) surface, measured on the same sample with increasing resolution. Right pane: the corresponding local conductance images, which were taken at the bias voltage of (a) -100 mV, (b) -200 mV and (c) -100 mV.

7.4 Results

7.4.1 Morphological and chemical influence on the local electronic structure of a clean Cr surface

A clean chromium surface was achieved after the removal of the surface oxide by more than 20 cycles of sputtering and annealing. Clean Cr surfaces were manifested by the presence of regions with flat terraces separated by single atom steps as well as the absence of contaminants as verified by Auger electron spectroscopy. The next step was to investigate the local surface electronic distribution that is independent of magnetic properties. We anticipated the local electronic density of states would vary across the surface, as it depends upon the morphology (steps and terraces). Likewise it was expected that the LODS would be affected by the presence of minute amounts of contaminants that caused a reconstruction of the surface atoms. Towards this goal, the experiment simultaneously measured the surface topography and the local conductance (dI/dV).

A synopsis of the results is shown in figure 7.5. The STM-acquired topographic images are arranged on the left panel from (a) to (c) with increasing resolution and the corresponding map of the electronic densities of states, obtained by lock-in technique at the bias voltage of -100 to -200 mV, are shown on the right. The influence of the surface morphology on the local density of states is evident. In figure 7.5 (a), the flat terrace areas are predominantly bright while the steps and step bunches are dark. Since the tunneling conductance (dI/dV) corresponds to the local density of electronic states of surface, this observation is reasonable since atoms on

steps have less nearest neighbor coordination than those at terraces. In addition to this gross difference, the figure 7.5 (b) shows fine structures in dI/dV in the form of localized dark contrast spots that pepper the otherwise uniformly bright flat terraces. These could not have been from local asperities taller than an atom as these would have shown up in the topographic image. Instead these were probably due to localized chemical defects such as interstitial substitution. Alternatively, these stark variations in the conductance could also have arisen from the surface reconstruction. The highest resolution image (c) supports this interpretation. From the STM image, we can clearly resolve the steps, which are around 1.5 \AA high. At the center is a flat terrace with an average roughness of less than 0.6 \AA . Interestingly despite the relative flatness of the terrace, the conductance image shows a mosaic pattern with dark and bright features. Unfortunately, in this experiment the tip sharpness was insufficient to reveal the individual atoms atomically. Nevertheless in the next section it will become clear that these variations were due to surface reconstructions which are presumably caused by the presence of nitrogen. In particular, there are two phases in which the nitrogen lattice coexisted on Cr (001). One had a $c(2 \times 2)$ structure and the other a $p(1 \times 1)$ on Cr (001). The difference in the nitrogen lattice leads to the perceived difference in the local conductance.

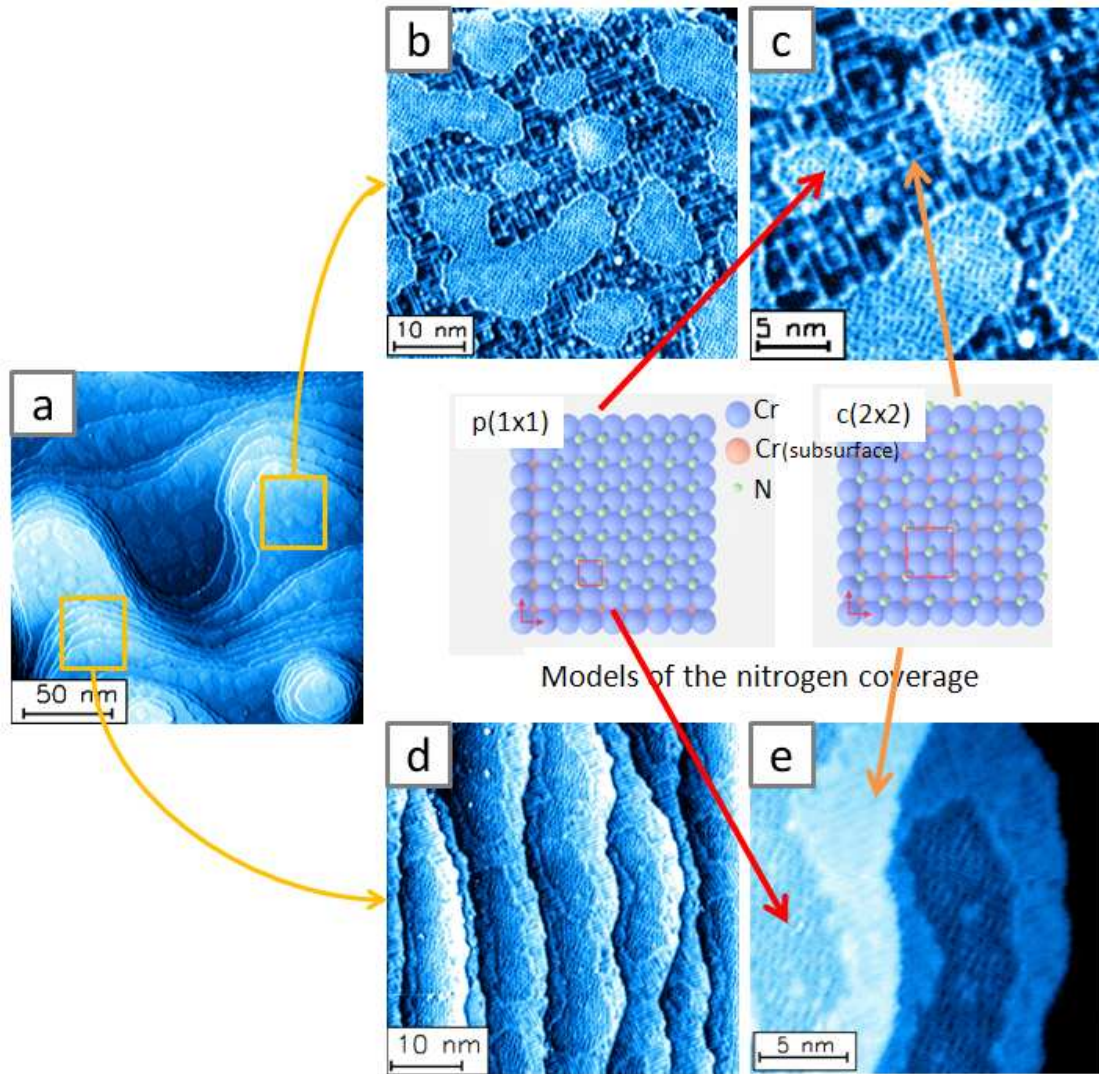


Figure 7.6 Atomically resolved STM images of nitrogen reconstructions on a cleaned chromium. (a) The topography on 200 nm by 200 nm area shows relatively flat areas between steps. High resolution images on a top flat terrace ((b),(c)) and on wide steps ((d),(e)) show the atomic corrugations with two different phases. The nitrogen, which has migrated from the bulk, takes the interstitial sites at the surface and induces two kinds of reconstructed structure. The corresponding models are suggested in the middle of the figure, which are the $p(1 \times 1)$ and $c(2 \times 2)$ phases.

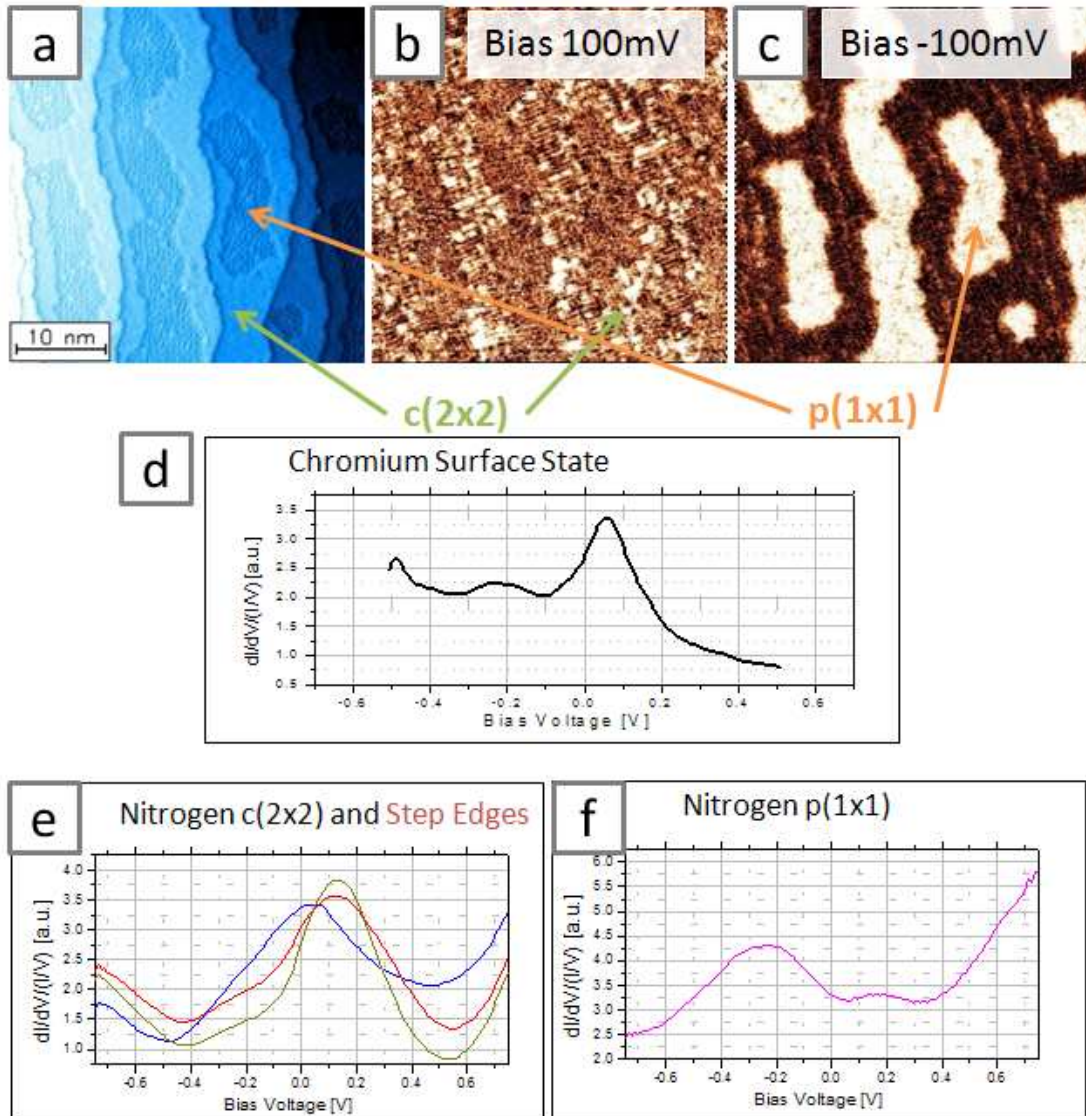


Figure 7.7 STM/STS measurement on Cr(001) shows the nitrogen contamination with $p(1 \times 1)$ and $c(2 \times 2)$ phases. (a) STM topography and dI/dU map at (b) 100 mV and (c) -100 mV bias voltage, which reveals a clear contrast difference on nitrogen reconstruction area. Graphs below show the full STS data on (d) Cr surface, (e) step edges and N-induced $c(2 \times 2)$ state, and (f) $p(1 \times 1)$ state.

7.4.2 Nitrogen reconstruction on a clean Cr surface

Figure 7.6 shows images of the clean surface taken with an extremely sharp tip to reveal the fine structures of the surface. To put the images into context, we included a large area scan (a) to show the surface topography. The high resolution STM images were taken on the top terraces as well as on some of the terraces. It is evident that there were two types of domains that formed on these surfaces, which could be distinguished by the density or spacing of the corrugations. More precisely, there were patches with highly ordered atomic features scattered over a background with less order and longer corrugation wavelength. A clearer distinction between the two phases can be seen on the terraces particularly in image (f). Similar domains have been observed by others using quantitative LEED analysis [81, 82] and electron spectroscopy [83]. These are believed to be superstructures formed by dissolved nitrogen atoms that have migrated into the surface and have taken up interstitial sites during the annealing process. From the energy considerations [81-83], there are two kinds of surface reconstructions, namely $p(1 \times 1)$ and $c(2 \times 2)$. The models are presented in figure 7.6 (d), to illustrate how the N atoms reside on all four-fold hollow interstitial sites on the Cr lattice for $p(1 \times 1)$ Cr and on every other site in the case of $c(2 \times 2)$.

More importantly, these N superstructures affected the electronic density of states in a very profound way. This is illustrated in figure 7.7 by showing the di/dv map corresponding to the topography on the terraces. The contrast distinction between the phases was apparent at the -100 mV bias. Bright areas in the di/dv curves

that correspond to high density of filled electronic states at 100 mV below the Fermi level characterize the p(1x1) phase.

The local density of states around the Fermi level on representative areas of the surface were measured, and the average spectra on each case are presented in (d). To obtain these curves, the current (I) and conductivity were measured simultaneously with the corresponding topography. The differential conductivity spectra ($dI/dV/(I/V)$) was then normalized and averaged hundreds of data points having similar behavior. The spectra show that the c(2x2) phase had a similar peak as the chromium surface state, except for a small shift of the peak energy from 0.06 eV to 0.12 eV. For the sake of comparison, the spectra at the step edges were also examined and found to be at a slightly lower peak intensity. By contrast, the p(1x1) surface spectra had completely different electronic behavior. It had a very large density of states at negative voltage especially around -200 mV. This was the source of the bright contrast on the dI/dV map in (c).

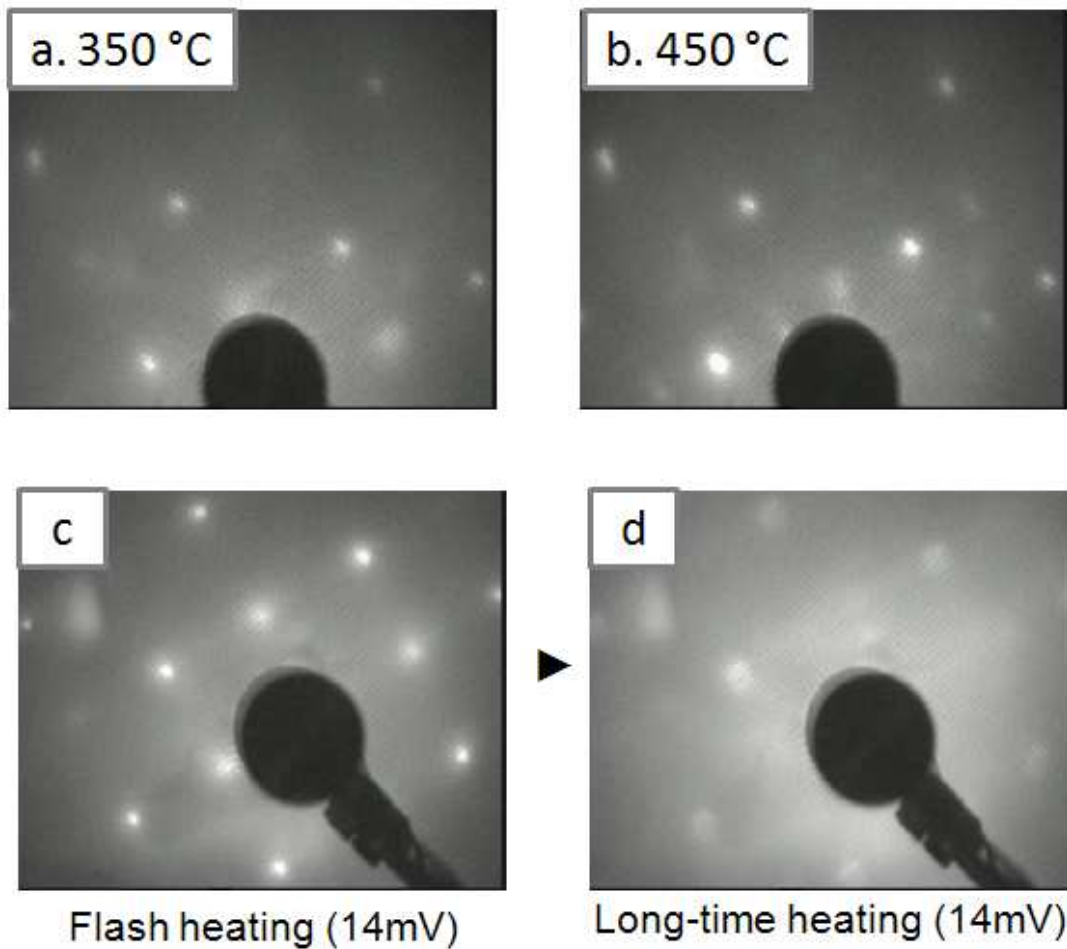


Figure 7.8 Low energy electron diffraction (LEED) measurement, as the function of the annealing temperature and duration. The LEED images were taken at the energy of 209 eV and recorded by using CCD camera. (a) At the temperature up to 350 °C, LEED showed a clear pattern, while in image (b) it has some additional spots at higher temperature of 450 °C. In addition, (c) the flash heating induced a much clearer pattern being diffused by longer heating, as shown in (d). Thus, the best annealing condition based on LEED measurement was the flash heating at 350 °C.

7.4.3 Preparation conditions for having a cleaned, less-damaged surface

Since the goal of this experiment was to demonstrate spin polarized tunneling, the presence of nitrogen will negate this effect, since the spins will depolarize at the nitrogen – Cr interface. Thus, in order for SPSTM to be successful, it was necessary to ensure a surface that was free of nitrogen contamination. We found that preparing the optimal surface was a balance between nitrogen migration and the surface roughness. Low level annealing using short duration heating at low temperature was a sufficiently good solution for suppressing nitrogen, but was less effective in healing the surface. The temperature was kept a low level to cause appreciable mobility of the surface atoms which left the surface rough and defect filled. Nevertheless, it was necessary to employ a procedure in which tolerated a certain degree of roughness in exchange for diminished nitrogen contamination.

The surface was then examined using low energy electron diffraction (LEED) and correlated the LEED patterns with annealing temperature. The LEED patterns were representations of the reciprocal space lattice, and the electron mean free path at the energy used in the measurements (~ 200 eV) was only a few nanometers. It was extremely surface sensitive and very effective in revealing any surface reconstruction and disorder. Figure 7.8 demonstrates the influence of the annealing temperature on the surface structure. Figure 7.8 (a) was taken after a one-hour 350°C annealing case. It shows a clear square pattern characteristic of the (001) face of the fcc crystal structure. However, when the temperature was raised to 450°C , faint yet discernable extra spots emerged on the pattern, an indication that a superlattice had formed on the surface. Since annealing to 450°C caused excessive nitrogen surface accumulation, it

is clear that 350 °C was the better annealing temperature. To complete the studies, the influence of annealing duration on the patterns at the fixed temperature of 350 °C was also assessed. Figure 7.8 (d) shows that annealing for a long time led to more diffused LEED spots, suggesting a variation of the spatial dimension of lattice. It also suggests increased disorder on the surface, which may have resulted from the increased number of nitrogen atoms. Based on the aforementioned results, the final step was adapted to incorporate a shortened anneal time at a temperature lower than 400 °C for less than 5 minutes after sputtering.

To summarize, a two step process for surface preparation was used. The first step was to deplete the residual contamination from the bulk. More than 10 cycles of high energy (~ 2 keV) sputtering were performed for several hours and followed by high temperature (about 600 °C) annealing for two hours. The second step, performed immediately prior to imaging the sample, was a low energy (600-800 eV) sputtering for 30 minutes followed by the quick annealing at 350 °C. This left the surface with very little or no nitrogen and with less defects. This is shown in figure 7.9 (a)-(c) with increasing resolution. The corresponding conductance measurement (figure 7.9 (d)) at the bias voltage of -200 mV validated the nitrogen-free surface as evident from the absence of any contrast change. Lastly, the sample at 300 °C was annealed for 15 minutes, and a flat surface with the reduced density of defects was obtained, as shown in (e). This surface proved to be sufficient to allow spin polarized STM investigations to be carried out.

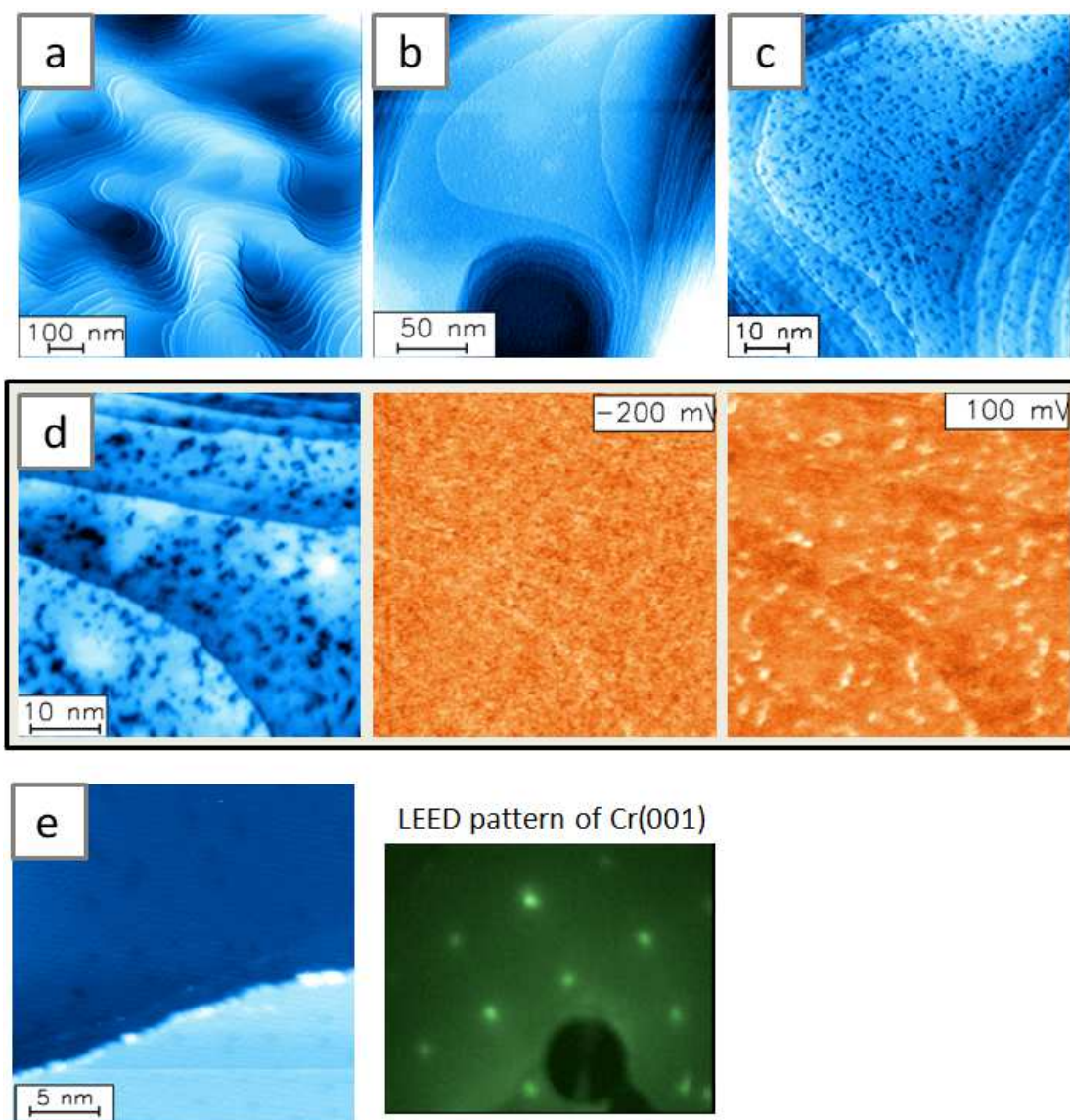


Figure 7.9 (a)~(c) STM images with different scan size on a cleaned Cr surface, which show no nitrogen reconstruction and less sputtering damages. These were obtained by low energy (600-800 eV) sputtering with subsequent annealing at 350 °C, after the amount of residual contamination was reduced by more than 10 additional cycles of cleaning. (d) Topography and the corresponding dI/dV maps taken at the bias voltage of -200 mV and 100 mV. (e) After additional annealing to 600 °C for 15 min, the STM showed a well-prepared surface with clear LEED pattern.

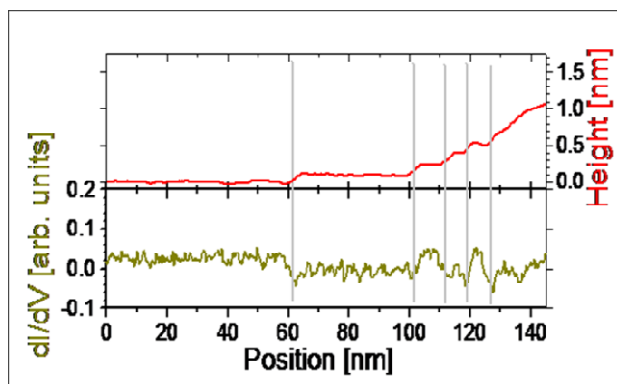
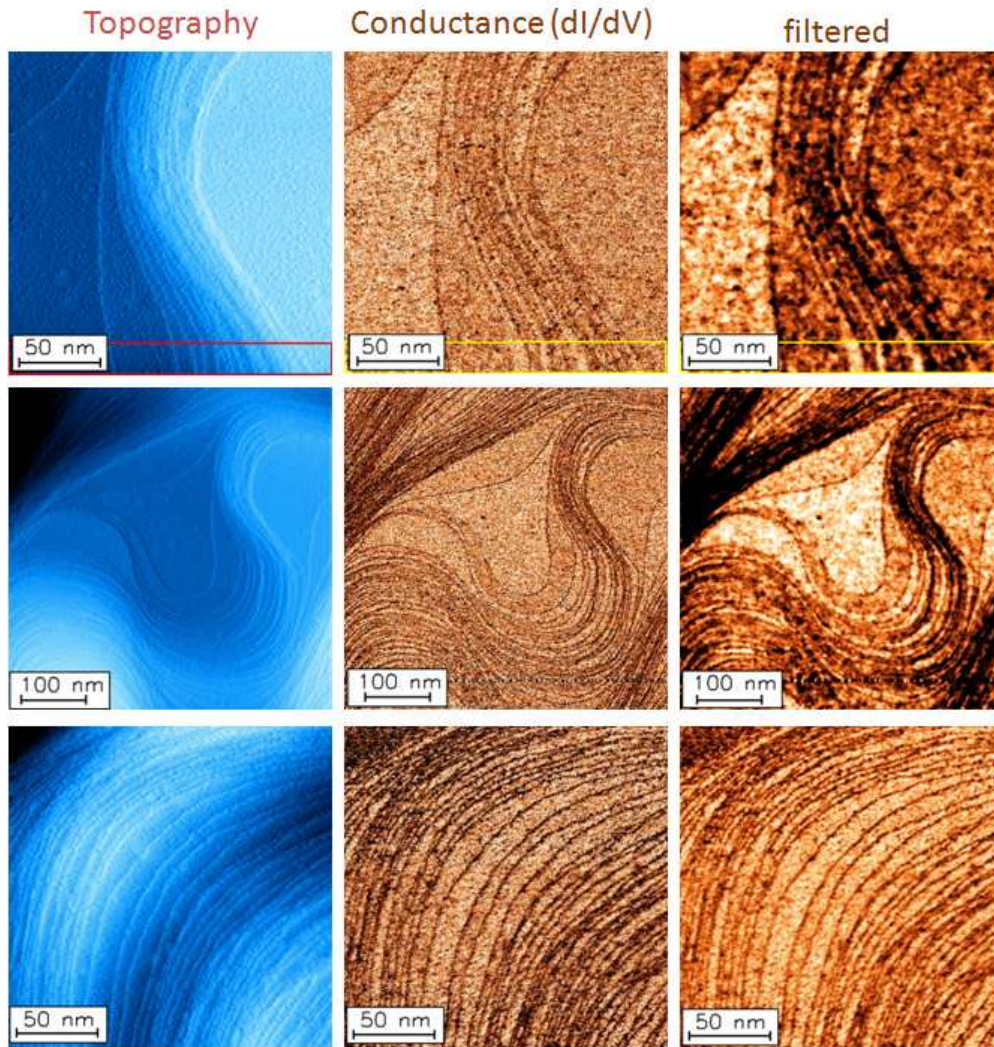


Figure 7.10 Spin-polarized STM measurement on antiferromagnetic Cr (001): Topographic images (first column) and corresponding dI/dV maps at -250 mV bias voltage (second column: row data, third

column: filtered). The cross sections on rectangular segments are plotted on the first row.

7.4.4 Implementation of spin-polarized STM on a Cr (001) crystal

On an adequately prepared Cr (001) surface, the alternating conductance levels across monoatomic steps, due to the spin-polarized tunneling, were observed. These variations were also observable on less than optimized samples, as long as there were regions where the crystallographic terraces were free of contamination. Of course, the tips would have to be properly coated with spin polarized ferromagnetic material. After cleaning, the tip was coated with nominally 11 nm of Fe according to the calibration of the evaporator. Next, the tip was annealed at 285 °C for 20 min.

An example of SPSTM is shown in figure 7.10, where the surface condition was closest to the one displayed in figure 7.9 (e). Despite the roughness of the terraces, it is evident from the STM images on various areas (first column) that the surface was comprised of several monoatomic steps. As a visual aid, the profile of a small rectangular segment in the first image in figure 7.10 is drawn in the accompanying plot. Starting from the left, the profile shows two large terraces of more than 50 nm in width, followed by a series of closely spaced terraces. The terraces were separated by a height of 1.5 Å, which matched half the height of a unit cell of Cr. The second column images are the conductance or dI/dV map of the surface at $V_{\text{bias}} = -0.25$ V, and were obtained concurrently with the topographic images. They contain the information on spin polarization. Note with care that most of the steps coincide with a contrast change in the dI/dV map. Focusing on images on first row, for example, the first terrace on the left had a brighter contrast than the adjacent terrace. This is a consequence of the antiferromagnetic character of the Cr crystal. The contrast change is also evident in the cross section (graph in figure 7.10),

where the locations of the topographic steps are drawn. Indeed, the line profile of the conductance map reveal alternating bright and dark contrast as each monatomic step is crossed. The dark contrast marking the step edge is most likely a scan artifact. By comparing the bright and dark contrast, a value of the spin polarization of $P=10\%$ was obtained.

The observations presented here on spin polarized tunneling correlated with the topography are consistent with the theoretical predictions and other measurements. The magnetic configuration of Cr (001) surface was first calculated by Fu and Freeman [84] by using an *ab initio* density functional theory with the full-potential linearized augmented plane wave method. The computed surface density of states for the majority and minority spin of a seven-layer Cr (001) film proved that (001) surface of Cr is ferromagnetic while chromium bulk remains antiferromagnetic. This surface ferromagnetism stems from the sharp surface state peak near the Fermi level for the paramagnetic state. Further study made by Blügel *et al.* [76] suggested two possible models of spin arrangements on the Cr (001): one is the mixture of surface states comprised of p(1x1) state, which induces ferromagnetism and the c(2x2) which exhibits antiferromagnetic magnetic configuration. The other model is the so called ‘topological antiferromagnetism’ between ferromagnetic terraces separated by single steps. Based on the self-consistent total energy calculations, Blugel et al. found that the topological antiferromagnetism of the Cr (001) surface is energetically more favorable. This model can easily explain the discrepancies in other experimental results, such as the failure to detect magnetization by spin-resolved photoemission spectroscopy [85] despite the detection of spin-split surface states by

energy- and angle-resolved photoemission [86]. It turned out that due to some miscut of a Cr (001) crystal numerous terraces with opposite magnetization simultaneously exposed on the surface, a cancellation of magnetization was induced on the light spot of spin-resolved photoemission, while majority and minority spin states (such as d_{z^2} like surface states) inside each ferromagnetic terrace were detected by other photoemission methods. Which of these models actually corresponds to reality can be directly verified by the SPSTM measurements. In this case, the latter model of antiferromagnetic layers is readily supported by the observation of the alternating tunneling conductance on the adjacent layers in Cr (001), as shown in figure 7.10.

Our spin-polarized result, which was detected on the conductance map with the spectroscopic mode, was different from the previous measurement by Wiesendanger et al. [87] which was taken on the constant current mode. By using a CrO₂ STM tip, Weisendanger et al, found the periodic alternations of monoatomic step heights such as 0.12 and 0.16 nm apparent on the topography, while the single-step height of 0.14 nm was uniformly measured with a non-magnetic tungsten tip. Compared to this method, where the spin resolved information was involved in the topography signal, the SPSTM combined with spectroscopic data comes with the a strong advantage of a successful separation of topographic, electronic, and magnetic contributions on the tunneling current near Fermi level. The result presented here is also consistent with the measurement of local tunneling spectra for two spin directions [77], which indicate a clear difference of surface state intensity between two spin alignments close to the Fermi level. In this paper, the spin polarization of $P \sim 20\%$ is reported, which is more than the measurement with the value of $P = 10\%$.

This discrepancy is attributable to the less than optimal magnetic/spin structure of the tip, a possible misalignment of the tip magnetization of 60° with respect to the Cr magnetic moments, as well as some spin-resolved information included in the topography by the constant current mode being used for scan.

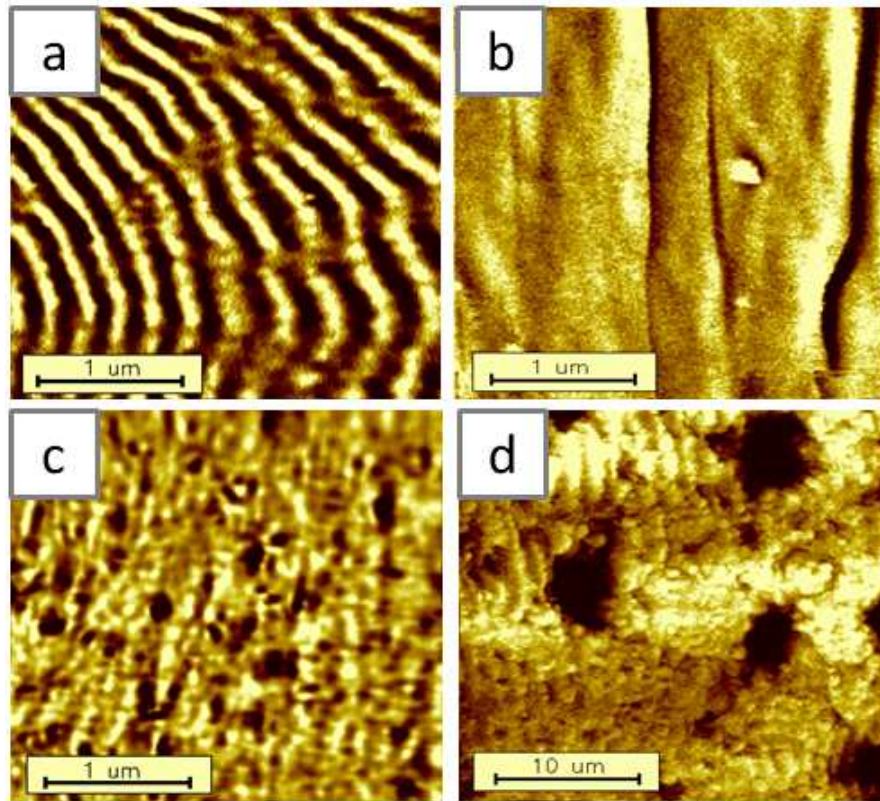


Figure 7.11 Changes of MFM images by annealing temperature of (a) 200 °C, (b) 300 °C, (c) 450 °C, and (d) 650 °C.

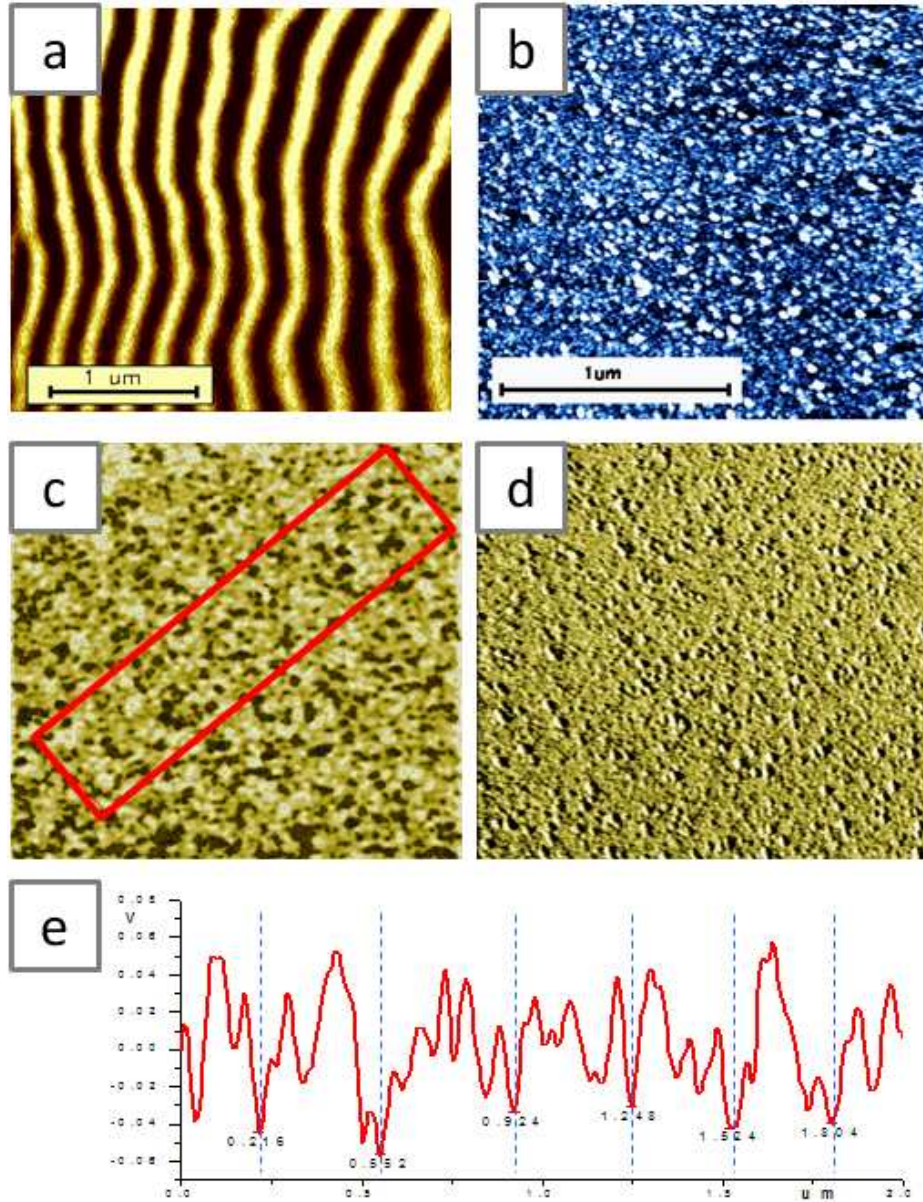


Figure 7.12 MFM and SP-STM measurements on a 200 nm thick Permalloy film. (a) MFM image shows out-of-plane stripe domain structures with the width of around 300 nm. (b) STM images on a cleaned permalloy film and (c)~(d) its simultaneous measurements of conductance at the bias voltage of 400 mV (forward scan mode) and -400 mV (backward scan mode), respectively. At the bias voltage of 400 mV (in case of (c)), slight contrast changes with stripe pattern are found while no contrast

difference is apparent at the bias voltage of -400mV (in case of (d)). This week pattern is better distinct in the cross section of the rectangle presented in the image (c). In (d), the cross section graph shows the periodicity of around 300 nm width, which is compatible with the MFM measurement.

7.4.5 Implementation of spin-polarized STM on a 200 nm thick

Permalloy film

A spin-resolved STM measurement was also taken on a 200 nm thick permalloy ($\text{Ni}_{80}\text{Fe}_{20}$) film. This film had out-of-plane magnetization with the stripe magnetic domain structure, which can be easily detected as repeated bright and dark stripes on contrast in MFM shown in figure 7.12 (a). The stripe domain was around 300 nm wide, and it was not correlated with any topographic features. This domain configuration was also observed in the STM conductance map, which was taken in UHV by using a Fe-coated STM tip. With a properly magnetized tip, SPSTM can be used for detecting out-of-magnetization on the polycrystalline film, as well as in-plane magnetization on a single crystal such as chromium.

The details of the experimental procedure are as follows. The film was grown on a silicon oxide substrate by a thermal evaporator at high vacuum range, and then transferred into the UHV system. Interestingly, the magnetic configuration changed significantly depending on the heating temperature, even at the temperature much below the curie temperature of 869K. This is well presented in figure 7.11. Domain boundaries begin to diffuse at the temperature of 200 °C, getting wider at the

temperature of 300 °C. In addition, at the temperature of 450 °C, the film was deformed topologically, inducing the complex magnetic configuration in the image of (c). This deformation became severe, with big pits and bumps apparent on the surface, which destroys the magnetic domain structure, as shown in image (d). Since the permalloy sample was loaded into UHV, it need to be sputtered (1 keV) in order to get rid of initial dust. This was followed by annealing at less than 200 °C due to the limitation of the temperature. Because this temperature was not high enough to be recovered from the sputtering damage, clean permalloy film with 15 nm thickness was added by a e-beam evaporator for making a smooth clean surface. Lastly, 10 nm iron was evaporated on the top of permalloy film to increase the stability of SPSTM, because a single material induces more stable and less noisy signal than the mixture of nickel and iron and iron (the following fragment does not fit grammatically with the sentence) is also the same material to the coating of SPSTM tip which can reduce the possibility of tip change during scanning. A Fe-coated STM tip was prepared by evaporating iron with 5~10 nm thickness onto a tungsten tip, followed by annealing at up to 470 °C for 20 min.

The SPSTM result is shown in figure 7.12. The STM image of (b) reveals that the permalloy grew with island formation, leading to a polycrystalline structure. The grain size was around 10 nm diameter and the surface was quite rough, with an rms value of about 17 Å. Its corresponding conductance maps were simultaneously measured with two different sets of bias voltage depending on the scan direction. At the forward scan with bias voltage of 400 mV, image (c) exhibits weak contrast changes periodically along the diagonal from lower-left to upper-right corner, while

the backward scan with a bias voltage of -400 mV has no apparent corresponding contrast. The averaged cross-section graph (e) of the rectangle area marked on the image (c) reveals this periodicity clearly. The dark points emphasized by dash lines are located at the relative position of 0.216, 0.552, 0.924, 1.248, 1.524, and 1.804 μm , which induced a lateral periodicity of about 300 nm. This is consistent with the magnetic stripe patterns measured by MFM. Despite the weak signal, this measurement makes an important contribution as the first measurement of spin-resolved information on a polycrystalline structure with more complexity than a single crystal, and as the first attempt to implement a Fe-coated STM tip magnetized out-of-plane.

7.5 Conclusions

To summarize, the spin-polarized tunneling on the terraces of antiferromagnetic chromium (001) was successfully observed. Details on the morphological and chemical composition were shown as a function of various stages of surface preparation, and protocols for obtaining Cr (001) revealing spin-polarized contrast were observed. With the successive iterations of sputtering and annealing, the oxide, including the native and bulk segregated types, was completely removed, and the nitrogen migration onto the surface was well controlled. On the clean crystal the chromium surface electronic states at the Fermi level was observed as well as the spectra of nitrogen-induced superstructures. The spin splitting of the state was measured with the spin polarization of 10% by using an iron coated tungsten tip.

Chapter 8

Future Work

The previous chapters provide details on the electronic inhomogeneity of the film surfaces, especially the existence of surface contaminations (Fe oxides) as well as a variety of structural defects at interfaces. This fact can explain the discrepancy between the experimentally measured TMR (~200 %) and the theoretically expected value (>1000%) by diffusing the spin-coherent tunneling on a significant area of the surface. Because of the intrinsic growth mode of Fe on MgO, it may not be a suitable candidate for developing devices with very high yields. Recently however, it was discovered that amorphous CoFeB film deposited on MgO could be re-crystallized and form epitaxial layers simply by annealing. Thus, this is a natural process to extend our investigations to an alloy with CoFeB in place of pure Fe as the electrodes.

For this purpose, I have upgraded the Omicron UHV system to be able to grow a CoFeB film and to build a complete magnetic tunnel junction structure with appropriate exchange biasing. Specifically I performed the following modifications in the Omicron system.

- a) Designed, built and introduced three new sputtering sources
- b) Designed, built and introduced a triple e-beam evaporation source
- c) Designed a sample holder in the Fast-Entry Lock
- d) Designed and fabricated a sputtering shutter

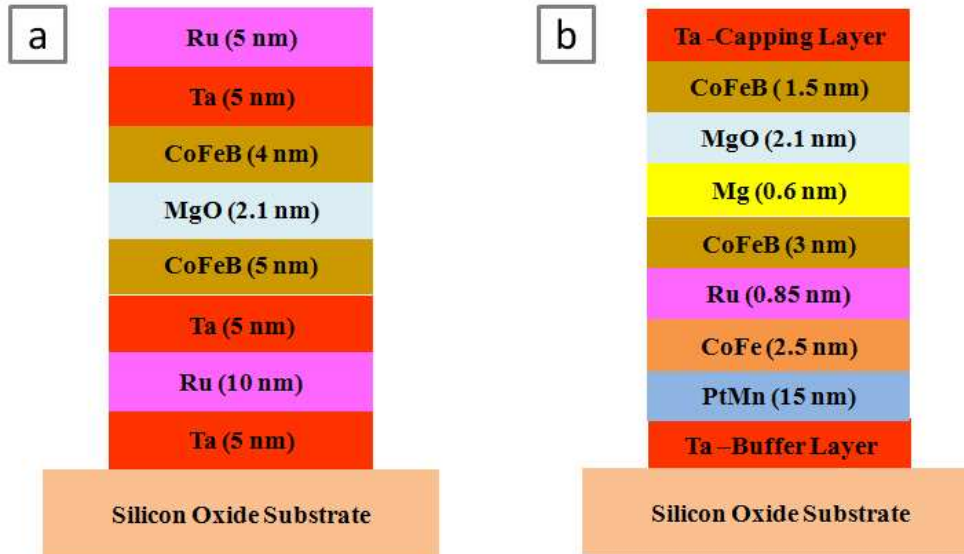


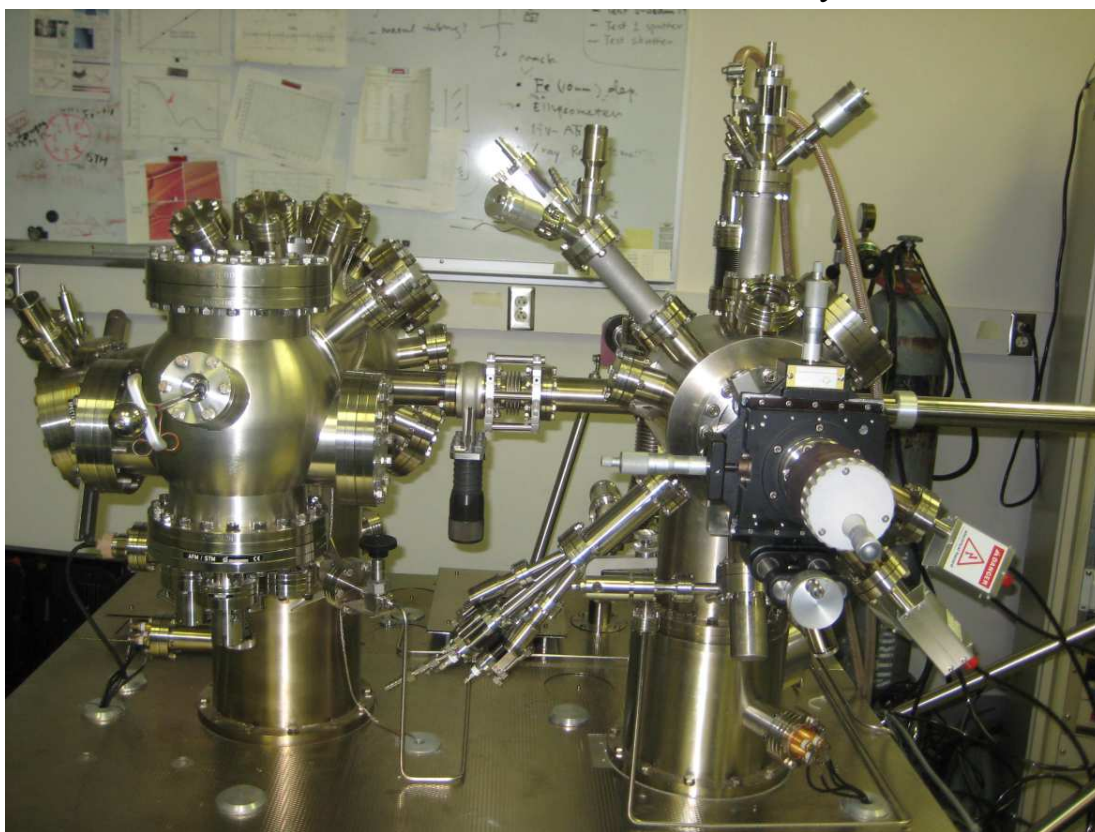
Figure 8.1 Examples of sample structures employing the CoFeB/MgO/CoFeB magnetic tunneling junction. The pseudo-spin-valve magnetic tunnel junction structure of (a) has produced a TMR of 604% at room temperature [88], and the sample structure of (b) was used for generating high-power microwave as reported in 2008 [89].

When all systems are in place, this will significantly improve our fabrication capability. We will be able to build complicated multilayer structures, such as substrate/Ta/Ru/CoFeB/MgO/CoFeB/Ta/Ru for achieving a TMR of 600 % [88], and/or substrate/buffer layer/PtMn/CoFe/Ru/CoFeB/Mg/MgO/CoFeB/capping layer for generating radio-frequency [89], as depicted in figure 8.1. These structures can be made by using three sputtering guns loaded with PtMn, CoFe and CoFeB sources, and e-beam evaporators loaded with Ta, Ru, Mg, and MgO materials. Details of the system modification are shown in the appendix.

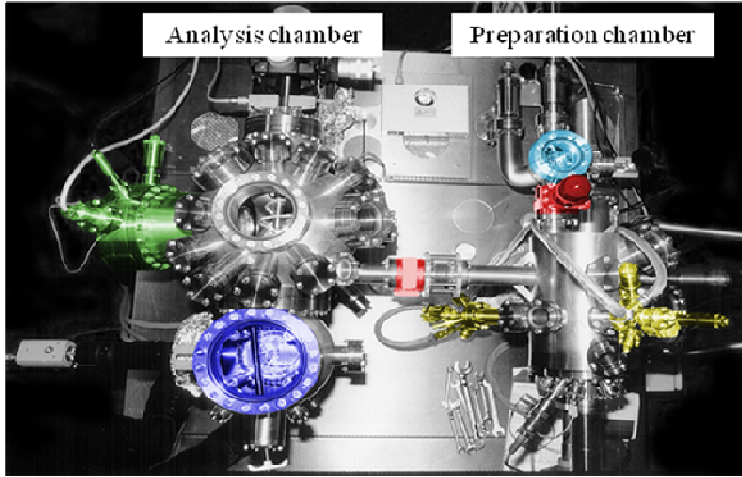
APPENDIX A: Overview of the Omicron UHV System

A.1. Overview of the Omicron UHV system

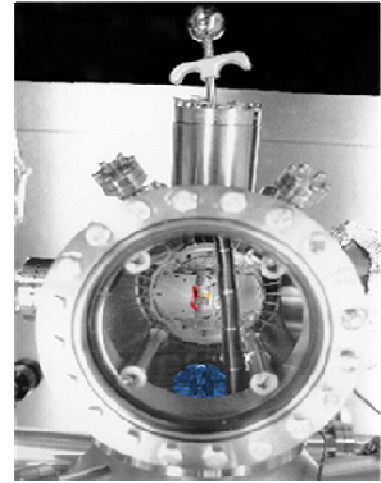
Front View of the Omicron UHV system



Chamber (top view)



Microscope (top view)



- two electron beam evaporators (MgO,Fe)
- sputter gun
- sample heater
- fast entry lock
- valve
- combined STM/AFM
- combined LEED/AES-system

- tip holder
 - sample holder
 - spare for 8 samples or tips
- Microscope parameters:
- scan range $6\ \mu\text{m} \times 6\ \mu\text{m}$
 - tip and sample can be changed in UHV

Figure A.1 Pictures with front view and top view of the existing Omicron UHV system. It consists of the analysis chamber and preparation chamber, which are interconnected by a gate valve. The analysis chamber has various in-situ diagnosis tools involving LEED, AES, AFM/MFM, and STM/STS, and the preparation chamber has equipped with two e-beam evaporators, an Ar-sputtering gun and a heating stage.

A.2 Upgrading the preparation chamber with fabrication capabilities

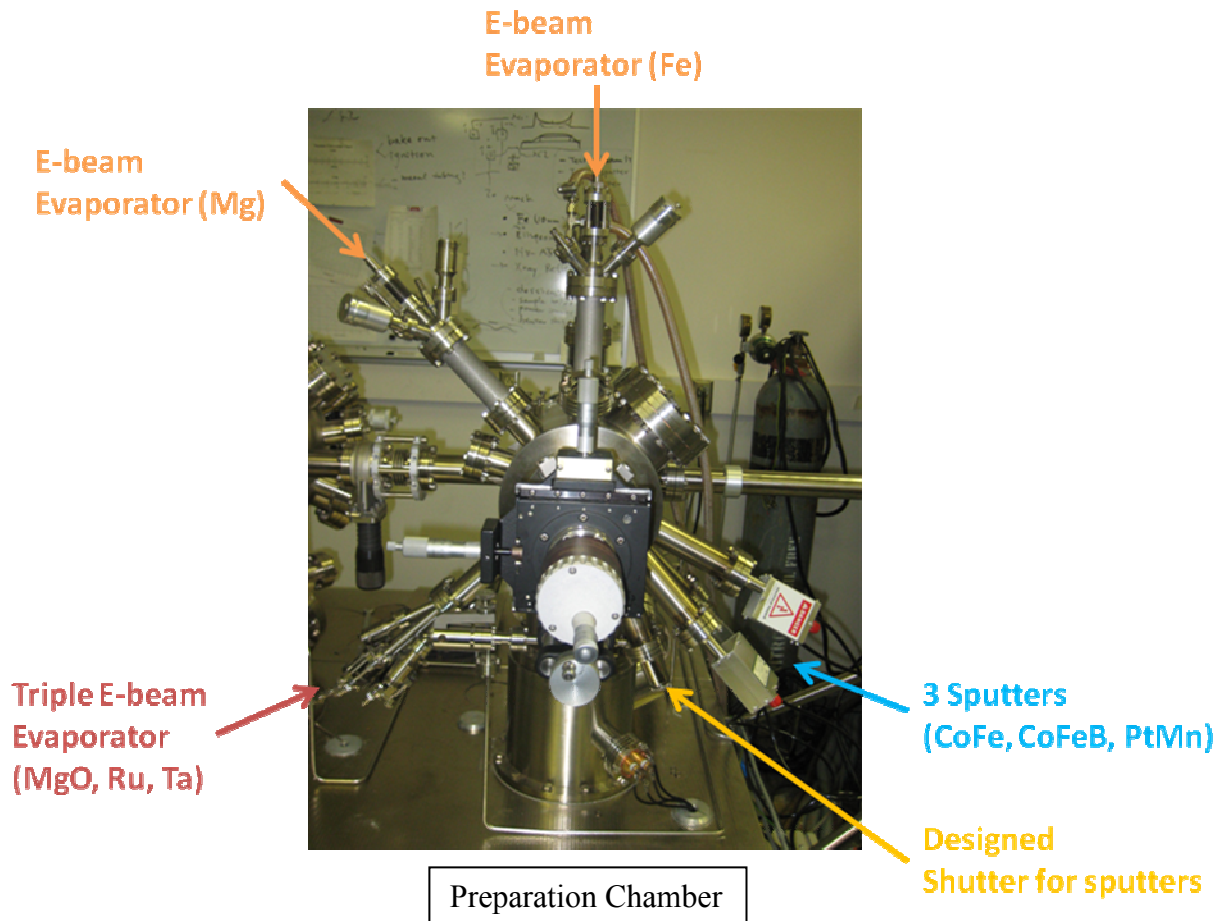
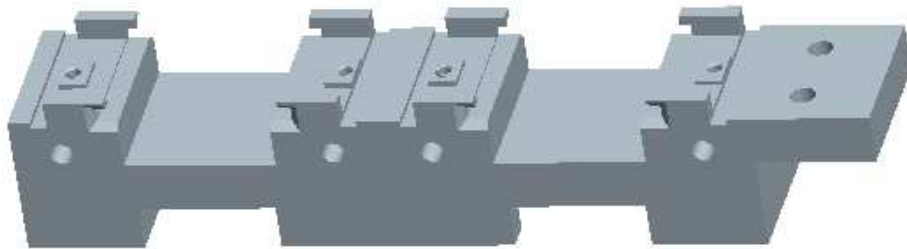


Figure A. 2 The upgraded preparation chamber with additional fabrication capabilities. Three sputtering guns with source materials of CoFe, CoFeB and PtMn are now attached in the right-handed side of the chamber, and one triple e-beam evaporator and two single e-beam evaporators are in the left-handed side with source materials of MgO, Ru, Ta, Mg and Fe, respectively.

APPENDIX B: Design and Modification for the UHV System

B.1 Sample holder for the fast-entry lock

a) 3-D rendering of the machine drawing



b) Implementation in the UHV system

SIMPLFD REP: Geometry Rep



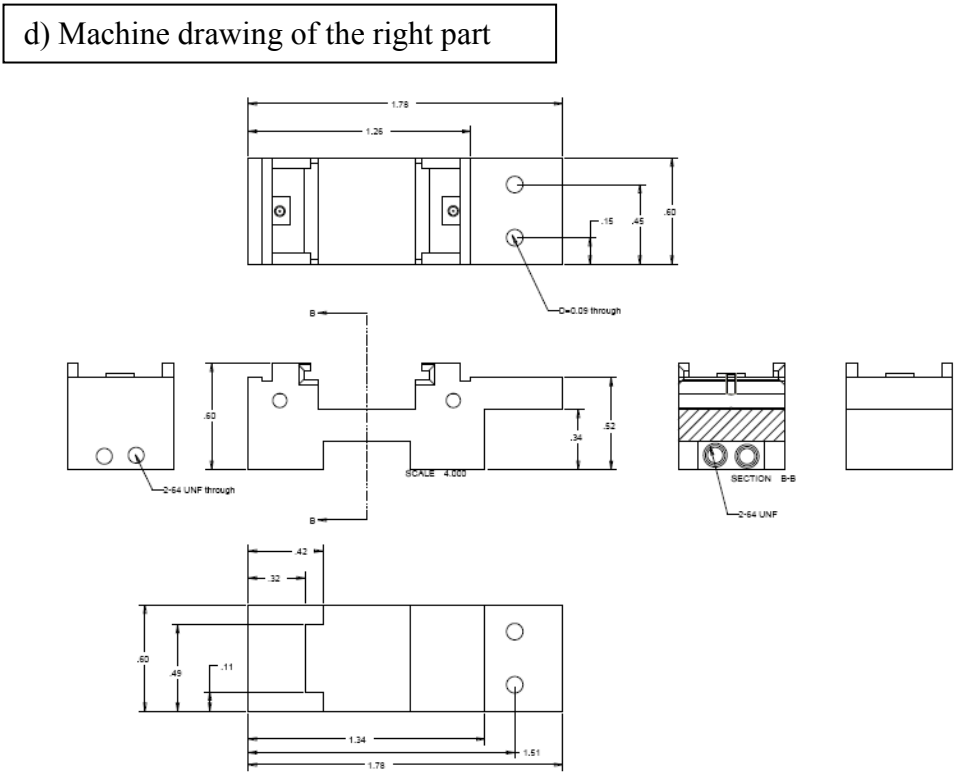
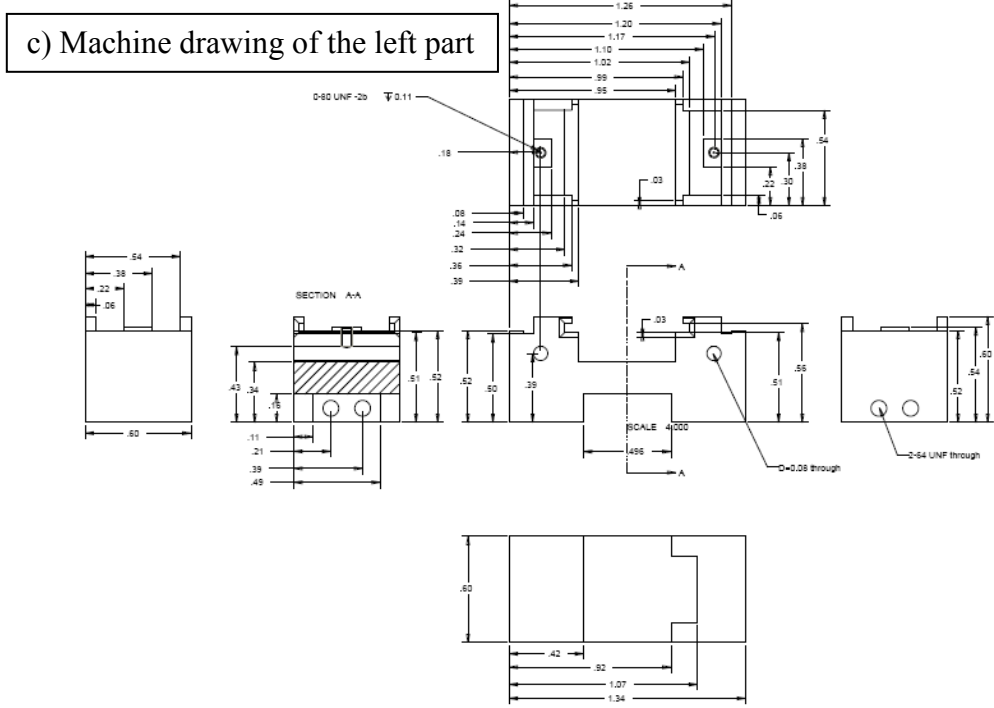
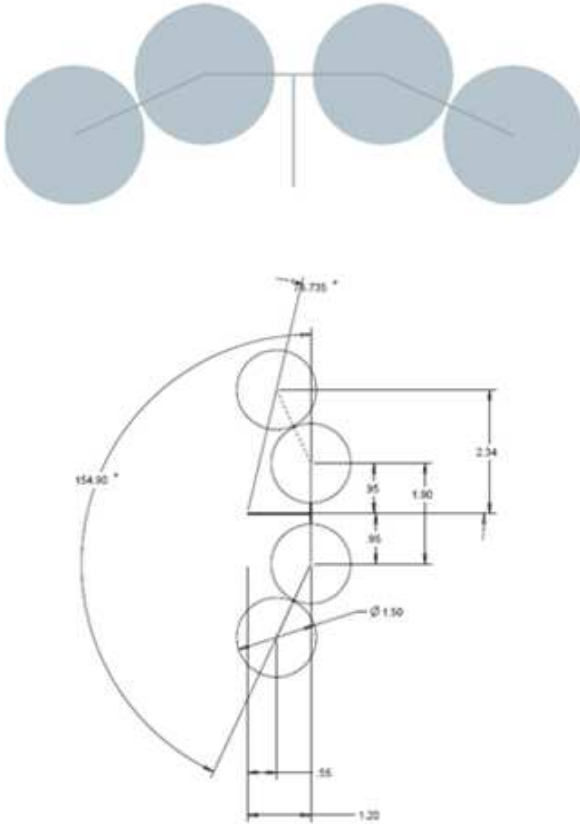


Figure B. 1 Design and implementation of a new sample holder for the fast-entry lock (FEL) in the UHV system to increase the sample throughput. The new design consists

of two identical holders, making it possible to transfer two samples into and out of the chamber at each FEL-pumping, while the original part had only one holder. Figures show (a) 3-D rendering of ProE design, (b) the fabrication and implementation in the system, and its machine drawing of (c) left and (d) right parts.

B.2 Shutter for three sputtering guns in the preparation chamber

a) Machine drawing for the shutter



b) Implementation in the UHV system

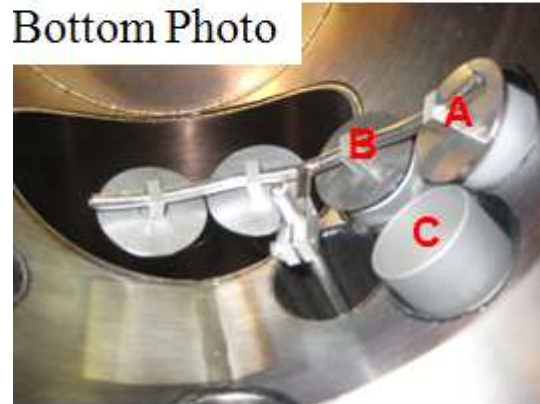
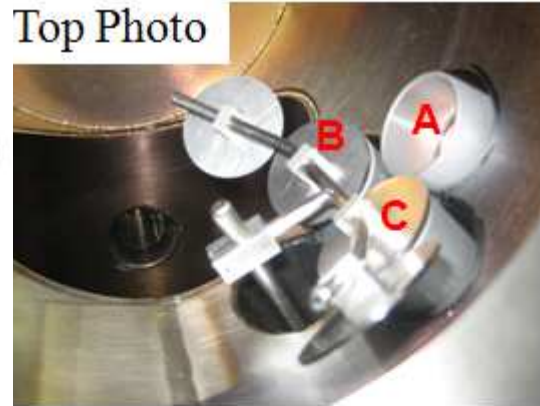
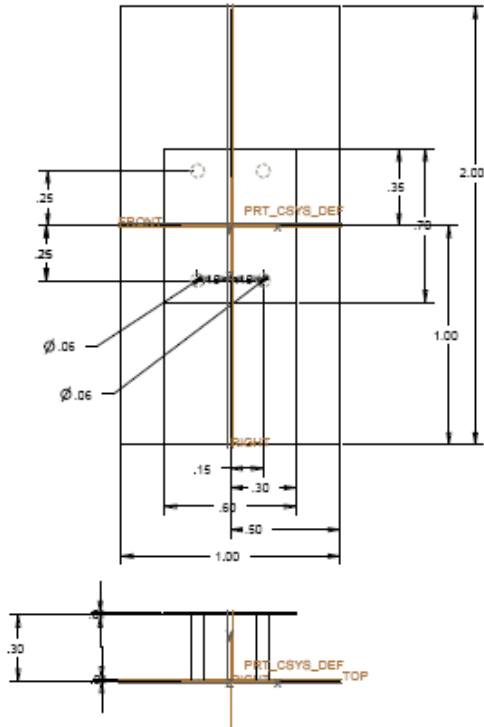


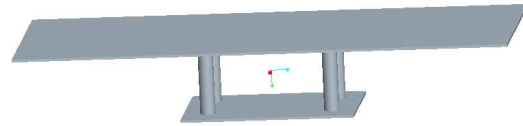
Figure B.2 A shutter for three additional sputtering guns, designed and built to prevent cross contamination: (a) machine drawing and (b) its implementation in the system. Due to the size restriction of the system and the limiting number of available flanges, the shutter has a wing shape and is bent out of plane with 6-inch curvature. Top photo: this shutter covers the two bottom guns (B and C), Bottom photo: a rotation of 77° counter clockwise makes it cover one top and one bottom guns (A and B) as shown in pictures.

B.3 Sample plate modification with an extended top plate

a) Machine drawing for the sample plate



b) 3-D rendering of the machine drawing



c) Implementation with the extension onto a conventional

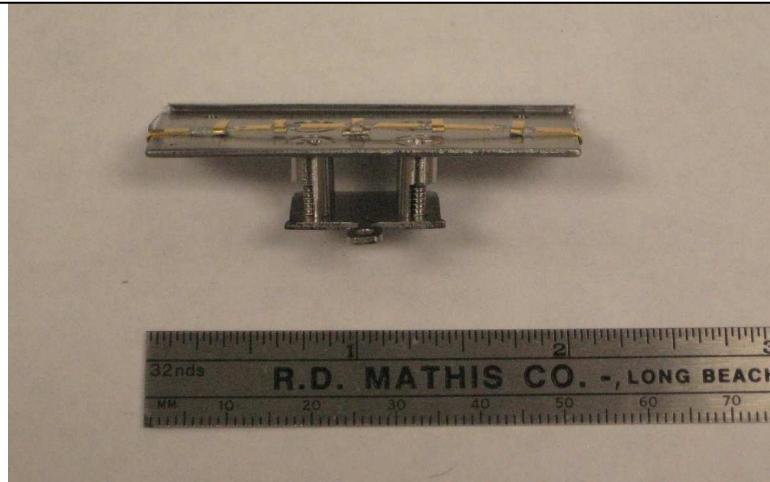


Figure B.3 Design and modification of a sample plate: (a) machine drawing, (b) 3-D rendering and (c) its implementation. A large plate (2 inch by 1 inch) is placed on top of a conventional sample plate for increasing sample throughput.

B.4 3-D drawing of a potential shutter for two additional sputtering guns

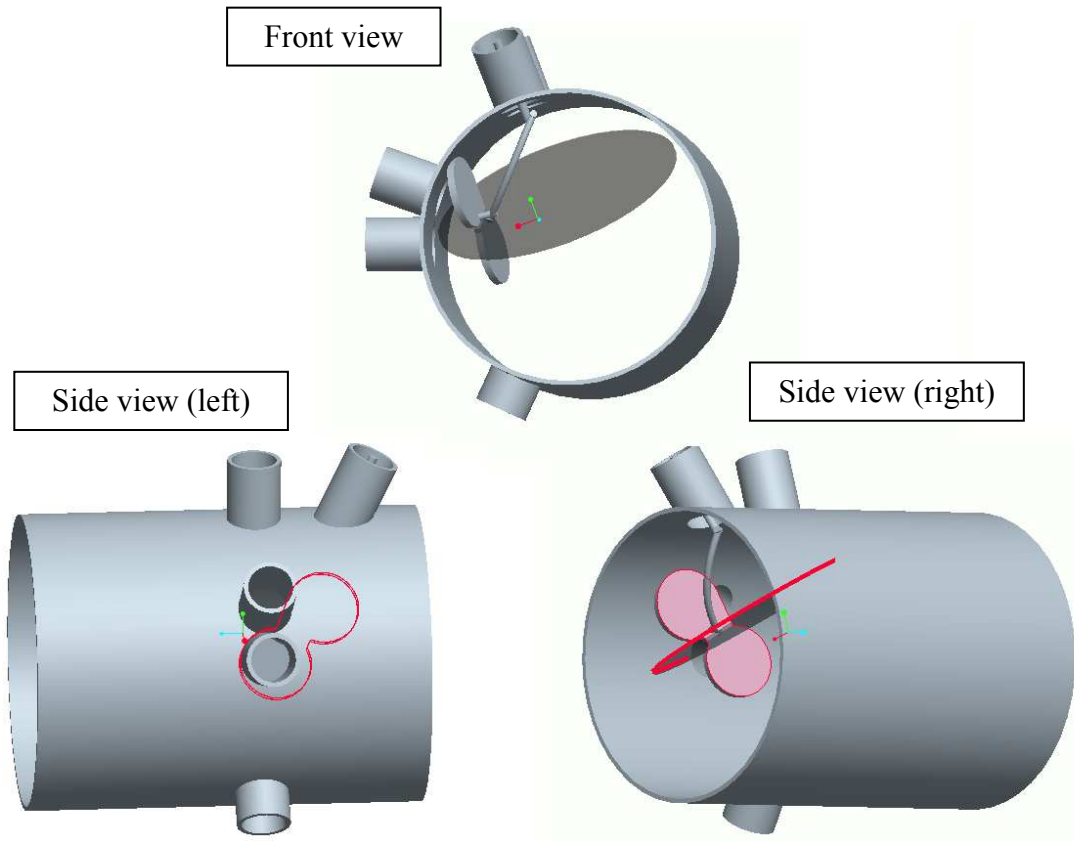


Figure B. 4 3-D rendering of the shutter in the preparation chamber, designed for the case of two additional sputtering guns. It would be attached to the front-top side of the preparation chamber because it is the only available flange. The shutter has a peanut shape and it rotates circularly along the center axis of the flange, which is angled 45° vertically.

APPENDIX C: The Growth of Carbon Nanotubes (CNTs) on Silicon Oxide and Quartz Substrates

C.1 Procedures

1. Dice a wafer, and wash with acetone/methanol/isopropanol/DI, N₂ blow dry
2. (Quartz) Pre-anneal for making aligned CNTs: for 12-20 hours, at 850°C
3. Catalyst Deposition Options
 - a. E-beam evaporation of Fe in UHV ~ 1 Å thickness
 - b. Ferritin: solution (from Atomate ®) diluted with DI
 - c. Iron-shadow mask: deposition by e-beam evaporator (aim to grow 3 Å thick Fe, but actual deposition is a couple of nm thickness)
 - d. Iron-photolithography
4. CNT growth via chemical vapor deposition (CVD)
 - 1) Heat in air at 850 °C for 10 min (for oxidization/reconfiguration of Fe)
 - 2) Cool down
 - 3) Flush furnace with Ar (flow rate:1688 ml/min) and H₂ (137 ml/min)
 - 4) Heat to 850 °C, holding for 10 min with H₂(137 ml/min)(for Fe reduction)
 - 5) CNT growth with H₂ (339 ml/min) with methane (366 ml/min), at 850 °C for 20 min
 - 6) Cool down to room temperature under H₂ flow

C. 2 Results: Secondary Electron Microscopy (SEM) measurements

1. CNT growth on silicon oxide substrates by using (a) e-beam evaporation of Fe: depositing a Fe thin film on silicon oxide substrates with around 1 Å thickness via e-beam evaporator in UHV (parameters: $V = 1 \text{ keV}$, $I_{\text{FLUX}} = 25 \text{ } \mu\text{A}$ and 75 seconds-duration).

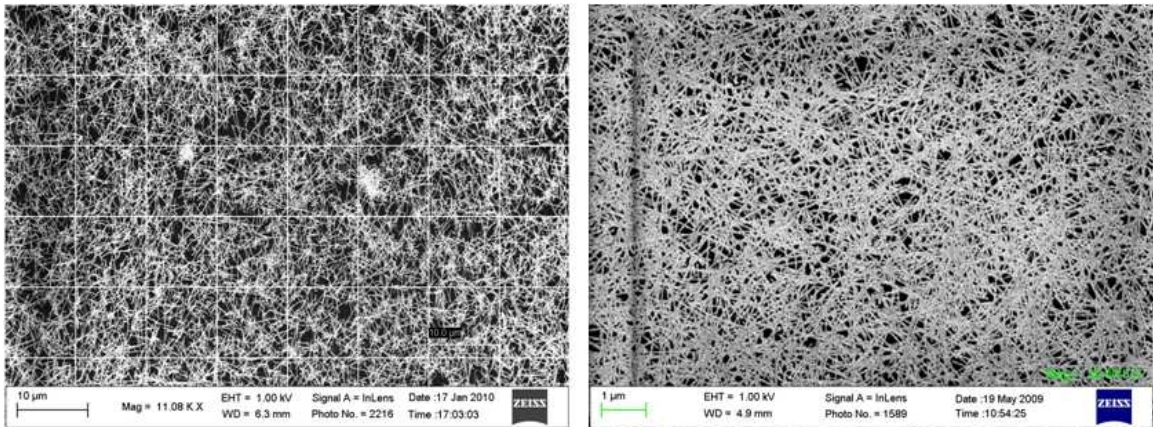


Figure C.1 SEM images of CNTs grown on silicon oxide substrates by evaporating Fe nanoparticles in UHV.

2. CNT growth on quartz substrates by using (b) ferritin solution: soaking the quartz substrates into the diluted Ferritin solution for several hours. The CNTs are well-aligned but have lots of kinks and cross-overs.

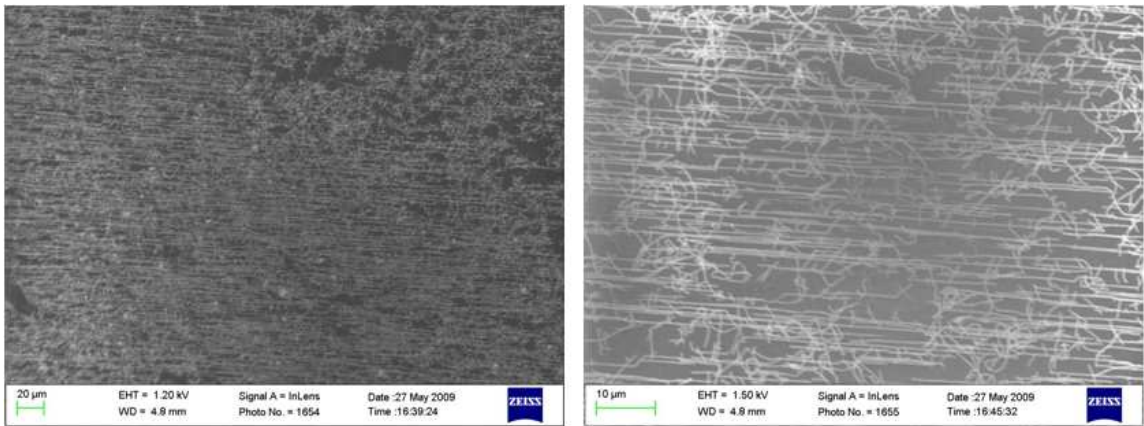


Figure C. 2 SEM images of CNTs on quartz substrates, which were grown by using a diluted ferritin solution.

3. CNT growth on quartz substrates by using (c) Fe-catalyst with a shadow-mask patterning: SEM exhibits well-aligned sparse CNTs with several hundred micrometers length, mostly starting from iron patterns.

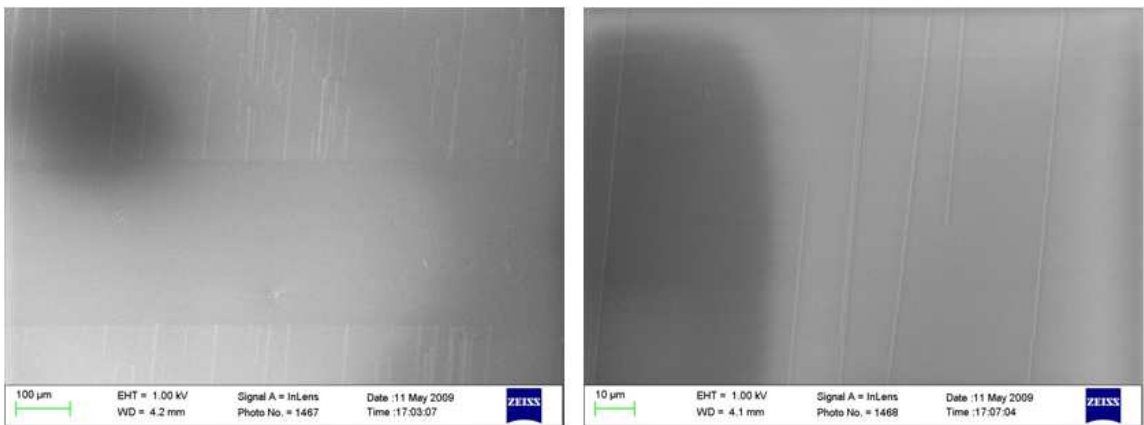


Figure C. 3 SEM images of CNTs on quartz by evaporating Fe-catalyst onto the sample, which was pre-covered by a metal shadow mask.

4. CNT growth on quartz substrates by using (d) Fe-catalyst that were pre-patterned by photo-lithography: SEM pictures show the successful growth of sparse CNTs across two iron patterns, which are 40 μm apart.

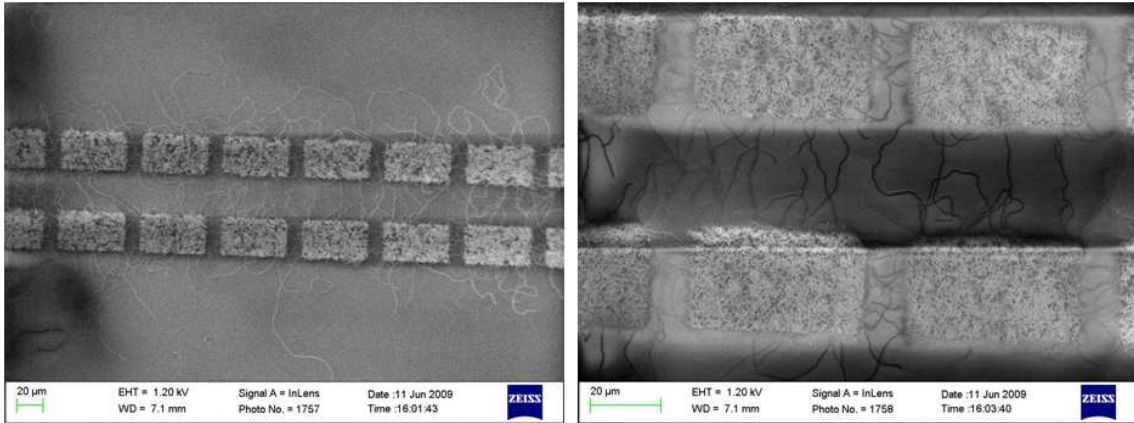


Figure C. 4 SEM images of CNTs on quartz substrates, which was pre-patterned by photo-lithography prior to the deposition of Fe and then lifted off.

Bibliography

- [1] Baibich M N, Broto J M, Fert A, Nguyen Van Dau F, Petroff F, Eitenne P, Creuzet G, Friederich A and Chazelas J, "Giant magnetoresistance of (001)Fe/(001)Cr magnetic superlattices," *Phys. Rev. Lett.* **61** 2472 (1998)
- [2] Miyazaki T and Tezuka N J, "Magnetic tunneling effect in Fe/Al₂O₃/Ni_{1-x}Fe_x junctions," *J. Magn. Magn. Mater.* **139** L231 (1995)
- [3] Moodera J S, Kinder L R, Wong T M and Meservey R, "Large magnetoresistance at room temperature in ferromagnetic thin film tunnel junctions," *Phys. Rev. Lett.* **74** 3273 (1995)
- [4] Julliere M, "Tunneling between ferromagnetic-films," *Phys. Lett. A* **54** 225 (1975)
- [5] Wang D, Nordman C, Daughton J, Qian Z and Fink J, "70% TMR at room temperature for SDT sandwich junctions with CoFeB as free and reference layers," *IEEE Trans. Magn.* **40** 2269 (2004)
- [6] Yuasa S, Nagahama T, Fukushima A, Suzuki Y and Ando K, "Giant room-temperature magnetoresistance in single-crystal Fe/MgO/Fe magnetic tunnel junctions," *Nature Material* **3** 868 (2004)
- [7] Parkin S, Kaiser C, Panchula A, Rice P, Hughes B, Samant M and Yang S, "Giant tunneling magnetoresistance at room temperature with MgO(100) tunnel barriers," *Nature Material* **3**, 862 (2004)
- [8] Butler W H, Zhang X G, Schulthess T C and MacLaren J M, "Spin-dependent tunneling conductance of Fe/MgO/Fe sandwiches," *Phys. Rev. B* **63** 054416 (2001)

- [9] Lee Y M, Hayakawa J, Ikeda S, Matsukura F and Ohno H, "Effect of electrode composition on the tunnel magnetoresistance of pseudo-spin-valve magnetic tunnel junction with a MgO tunnel barrier," *Appl. Phys. Lett.* **90** 212507 (2007)
- [10] Kittel C, "Introduction to Solid State Physics," John Wiley & Sons, Inc. 1996 (7th edition)
- [11] Marder P M, "Condensed Matter Physics," John Wiley & Sons, Inc. 2000
- [12] Sterns M B, "Simple explanation of tunneling spin-polarization of Fe, Co, Ni and its alloys," *J. Magn. Magn. Mater.* **5** 1062 (1977)
- [13] Slonczewski J C, "Conductance and exchange coupling of two ferromagnets separated by a tunneling barrier," *Phys. Rev. B* **39** 6995 (1989)
- [14] Tsymbal E Y, Mryasov O N and LeClair P R, "Spin-dependent tunneling in magnetic tunnel junctions," *J. Phys.: Condens. Matter* **15** R109-R142 (2003)
- [15] Zhang X G and Butler W H, "Band structure, evanescent states, and transport in spin tunnel junctions," *J. Phys.: Condens. Matter* **15** R1603-R1639 (2003)
- [16] Wiesendanger R, "Scanning Probe Microscopy and Spectroscopy: Methods and Applications," Cambridge University Press 1994
- [17] Tedrow P M and Merservey R, "Spin-dependent tunneling into ferromagnetic nickel," *Phys. Rev. Lett.* **26** 192 (1971)
- [18] Møller C and Plesset M S, "Note on an approximation treatment for many-electron systems," *Phys. Rev.* **46** 618 (1934)
- [19] Foulkes W M, Mitas L, Needs r J and Rajagopal G, "Quantum Monte Carlo simulations of solids," *Rev. Mod. Phys.* **73** 33-83 (2001)

- [20] Hohenberg P and Kohn W, “Inhomogeneous electron gas,” *Phys. Rev.* **136** B864 (1964)
- [21] Kohn W and Sham L J, “Self-consistent equations including exchange and correlation effects,” *Phys. Rev.* **140** A1133 (1965)
- [22] Kohn W, “Nobel lecture: Electronic structure of matter – wave functions and density functional,” *Rev. Mod. Phys.* **71** 1253 (1998)
- [23] Jones R O and Gunnarsson O, “The density functional formalism, its applications and prospects,” *Rev. Mod. Phys.* **61** 689 (1989)
- [24] Hill N A, “Density functional studies of multiferroic magnetoelectrics,” *Annu. Rev. Matter. Res.* **32** 1-37 (2002)
- [25] Barth U and Hedin L, “A local exchange-correlation potential for the spin polarized case,” *J. Phys. C: Solid State Phys.* **5** 1629 (1972)
- [26] Mathon J and Umerski A, “Theory of tunneling magnetoresistance of an epitaxial Fe/MgO/Fe(001) junction,” *Phys. Rev. B* **63** 220403(R) (2001)
- [27] MacLaren J M, Crampin S, Vvedensky D D and Pendry J B, “Layer Korringa-Kohn-Rostoker technique for surface and interface electronic properties,” *Phys. Rev. B* **40** 12164 (1989)
- [28] Thürmer K, Koch R, Weber M and Rieder K H, “Dynamic evolution of pyramid structures during growth of epitaxial Fe (001) films,” *Phys. Rev. Lett.* **75**(9) 1767 (1995)
- [29] Jordan S M, Lawler J F, Schad R and Kempen van H, “Growth temperature dependence of the magnetic and structural properties of epitaxial Fe layers on MgO(001),” *J. Appl. Phys.* **84**(3) 1499 (1998)

- [30] Subagyo A, Sueoka K, Mukasa K and Hayakawa K, "Scanning tunneling microscopy study of surface structure and magnetism of Fe thin films grown on MgO (001)," *Jpn. J. Appl. Phys.* **38** 3820 (1999)
- [31] Wassermann B, "Growth of iron films on MgO(100) substrates at 560-600 K," *Phil. Mag.* **83**(16) 1929 (2003)
- [32] Mizuguchi M, Suzuki Y, Nagahama T and Yuasa S, "Scanning tunneling microscopy observation of single-crystal Fe/MgO/Fe magnetic tunnel junctions," *J. Appl. Phys.* **99** 08T308 (2006)
- [33] Urano T and Kanaji T, "Atomic and electronic structure of ultrathin iron film on MgO(001) surface," *J. Phys. Soc. Jpn.* **57** 3043 (1988)
- [34] Li C and Freeman A J, "Giant monolayer magnetization of Fe on MgO: a nearly ideal two-dimensional magnetic system," *Phys. Rev. B* **43** 780 (1991)
- [35] Perdew J P and Zunger A, "Self-interaction correction to density-functional approximations for many-electron systems," *Phys. Rev. B* **23** 5048 (1981)
- [36] Whited R C, Flaten C J, and Walker W C, "Exciton thermoreflectance of MgO and CaO," *Solid State Commun.* **13**, 1903 (1973)
- [37] Tiusan C, Greullet F, Hehn M, Montaigne F, Andrieu S and Schuhl A, "Spin tunneling phenomena in single-crystal magnetic tunnel junction systems," *J. Phys.: Condens. Matter* **19** 165201 (2007)
- [38] Drakova D, "Theoretical modeling of scanning tunneling microscopy, scanning tunneling spectroscopy and atomic force microscopy," *Rep. Prog. Phys.* **64** 205-290 (2001)

- [39] Hofer W A, Foster A S and Shluger A L, “Theories of scanning probe microscopes at the atomic scale,” *Rev. Mod. Phys.* **75** 1287-1331 (2003)
- [40] Hamers R J, “Atomic-resolution surface spectroscopy with the scanning tunneling microscope,” *Annul. Rev. Phys. Chem.* **40** 531-59 (1989)
- [41] Schintke S and Schneider W-D, “Insulators at the ultrathin limit: electronic structure studied by scanning tunneling microscopy and scanning tunneling spectroscopy,” *J. Phys.: Condens. Matter* **16** R49-R81 (2004)
- [42] Moore A M and Weiss P S, “Functional and spectroscopic measurements with scanning tunneling microscopy,” *Annu. Rev. Anal. Chem.* **1** 857-82 (2008)
- [43] Stroscio J A and Kaiser W J, “Scanning Tunneling Microscopy,” Academic Press, Inc. 1993
- [44] Tersoff J and Hamann D R, “Theory and application for the scanning tunneling microscope,” *Phys. Rev. Lett.* **50** 1998-2001 (1983)
- [45] Tersoff J and Hamann D R, “Theory of the scanning tunneling microscope,” *Phys. Rev. B* **31** 805-13 (1985)
- [46] Feenstra R M, Thompson W A and Fein A P, “Real-space observation of π -bonded chains and surface disorder on Si(111)2 \times 1,” *Phys. Rev. Lett.* **56** 608-11 (1986)
- [47] Eigler D M, Weiss P S, Schweizer E K and Lang N D, “Imaging Xe with a low-temperature scanning tunneling microscope,” *Phys. Rev. Lett.* **66** 1189-91 (1991)
- [48] Lang N D, “Theory of single-atom imaging in the scanning tunneling microscope,” *Phys. Rev. Lett.* **56** 1164-67 (1986)

- [49] Lang N D, "Apparent size of an atom in the scanning tunneling microscope as a function of bias," *Phys. Rev. Lett.* **58** 45-48 (1987)
- [50] Feenstra R M and Stroscio J A, "Real-space determination of surface-structure by scanning tunneling microscopy," *Phys. Scripta* **T19A** 55 (1987)
- [51] Stroscio J A, Feenstra R M and Fein A P, "Electronic structure of the Si(111)2×1 surface by scanning-tunneling microscopy," *Phys. Rev. Lett.* **57** 2579-82 (1986)
- [52] Kaiser W J and Jacklevic R C, "Scanning tunneling microscopy study of metals: spectroscopy and topography," *Surf. Sci.* **181** 55-68 (1987)
- [53] Binnig G, Frank K H, Fuchs H, Garcia N, Reihl B, Rohrer H, Salvan F and Williams A R, "Tunneling spectroscopy and inverse photoemission: image and field states," *Phys. Rev. Lett.* **55** 991 (1985)
- [54] Binnig G, Rohrer H, Quate C F, and Gerber C, "Atomic force microscope," *Phys. Rev. Lett.* **56** 930 (1986)
- [55] Martin Y and Wickramasinghe H K, "Magnetic imaging by force microscopy with 1000Å resolution," *Appl. Phys. Lett.* **50** 1455 (1987)
- [56] Wadas A and Gruetter P, "Theoretical approach to magnetic force microscopy," *Phys. Rev. B* **39** 12013 (1989)
- [57] Dreyer M, Kleiber M, Wiesendanger R, "Simultaneous observation of atomic step and domain wall structure of ultrathin Co films by magnetic force microscopy in ultrahigh vacuum," *Appl. Phys. A* **69**, 359 (1999)
- [58] Dreyer M, Gomez R D and Mayergoyz I D, "Resolution enhancement by applying MFM under UHV conditions," *IEEE Trans. Magn.* **36**(5), 2975 (2000)

- [59] Cebollada F, Hernando-Mañeru A, Hernando A, Martínez-Boubeta C, Cebollada A and González J M, “Anisotropy, hysteresis, and morphology of self-patterned epitaxial Fe/MgO/GaAs films,” *Phys. Rev. B* **66**, 174410 (2002)
- [60] Oepen H P and Kirschner J, “Magnetization distribution of 180° domain walls at Fe(100) single-crystal surfaces,” *Phys. Rev. Lett.* **62**(7), 819 (1989)
- [61] Tusche C, Meyerheim H L, Jedrecy N, Renaud G, Ernst A, Henk J, Bruno P, and Kirschner J, “Oxygen-induced symmetrization and structural coherency in Fe/MgO/Fe(001) magnetic tunnel junctions,” *Phys. Rev. Lett.* **95** 176101 (2005)
- [62] Miao G X, Park Y J, Moodera J S, Seibt M, Eilers G, and Münzenberg M, “Disturbance of tunneling coherence by oxygen vacancy in epitaxial Fe/MgO/Fe magnetic tunnel junctions,” *Phys. Rev. Lett.* **100** 246803 (2008)
- [63] Lee J, Dreyer M, Krafft C, and Gomez R D, “Scanning tunneling microscopy/magnetic force microscopy study of ultrathin Fe film on MgO(001) in ultrahigh vacuum,” *J. Appl. Phys.* **101** 09D123 (2007).
- [64] Kuk Y, “STM on Metals” in Scanning Tunneling Microscopy I; Weisendanger R and Guntherodt H J (Eds), Springer Series in Surface Science 28 (1992) p. 23
- [65] Stroscio J A, Pierce D T, Davies A, and Celotta R J, “Tunneling spectroscopy of bcc (001) surface states,” *Phys. Rev. Lett.* **75** (16) 2960 (1995)
- [66] Biedermann A, Genser O, Hebenstreit W, Schmid M, Redinger J, Podloucky R, and Varga P, “Scanning tunneling spectroscopy of one-dimensional surface states on a metal surface,” *Phys. Rev. Lett.* **76** (22) 4179 (1996)

- [67] Bode M, Pascal R, Dreyer M, and Wiesendanger R, "Nanostructural and local electronic properties of Fe/W(110) correlated by scanning tunneling spectroscopy," *Phys. Rev. B* **54** (12) R8385 (1996)
- [68] Kawagoe T, Tamura E, Suzuki Y, and Koike K, "Scattering of surface-state electrons by the monatomic step in Fe(001): differential conductivity imaging by scanning tunneling microscopy," *Phys. Rev. B* **65** 024406 (2001)
- [69] Oka H, Subagyo A, Sawamura M, Sueoka K, and Mukasa K, "Scanning tunneling spectroscopy of $c(2 \times 2)$ reconstructed Fe thin-film surfaces," *Jpn. J. Appl. Phys.* **40** (6B) 4334 (2001)
- [70] Bischoff M M J, Yamada T K, Fang C M, de Groot R A, and van Kempen H, "Local electronic structure of Fe(001) surfaces studied by scanning tunneling spectroscopy," *Phys. Rev. B* **68** 045422 (2003)
- [71] Maris G, Jdira L, Hermsen J G H, Murphy S, Manai G, Shvets I V, and Speller S, "Towards spin-polarized scanning tunneling microscopy on magnetite (110)," *Jpn. J. Appl. Phys.* **45** (3B) 2225 (2006)
- [72] Schintke S, Messerli S, Pivetta M, Patthey F, Libioulle L, Stengel M, de Vita A, and Schneider W -D, "Insulator at the ultrathin limit: MgO on Ag(001)," *Phys. Rev. Lett.* **87** (27) 276801 (2001)
- [73] Mather P G, Read J C, and Buhrman R A, "Disorder, defects, and band gaps in ultrathin (001) MgO tunnel barrier layers," *Phys. Rev. B* **73** 205412 (2006)
- [74] Wu Y Z, Schmid A K, and Qiu Z Q, "Spin-dependent quantum interference from epitaxial MgO thin films on Fe(001)," *Phys. Rev. Lett.* **97** 217205 (2006)

- [75] Bode M, "Spin-polarized scanning tunneling microscopy," *Rep. Prog. Phys.* **66** 523 (2003)
- [76] Blügel S, Pescia D and Dederichs P H, "Ferromagnetism versus antiferromagnetism of the Cr(001) surface," *Phys. Rev. B* **39** 1392 (1989)
- [77] Kleiber K, Bode M, Ravlic R, and Tezuka N, "Magnetic properties of the Cr(001) surface studied by scanning tunneling spectroscopy," *J. Magn. Magn. Mater.* **240** 64 (2002)
- [78] Wiesendanger R, Bürgler D, Tarrach G, Schaub T, Hartmann U, Güntherodt H J, Shvets I V and Coey J M D, "Recent advances in scanning tunneling microscopy involving magnetic probes and samples," *Appl. Phys. A-Mat. Sci. Proc.* **53** 349 (1991)
- [79] Shvets I V, Wiesendanger R, Bürgler D, Tarrach G, Güntherodt H J, and Coey J M D, "Progress towards spin-polarized scanning tunneling microscopy," *J. Appl. Phys.* **71** 5489 (1992)
- [80] Maurice V, Cadot S, and Marcus P, "XPS, LEED and STM study of thin oxide films on Cr(110)," *Surf. Sci.* **458** 195 (2000)
- [81] Joly Y, Gauthier Y and Baudoing R, "Local environment of nitrogen in a surface nitride: a low-energy electron diffraction study of Cr(100)-(1×1)N," *Phys. Rev. B* **40** 10119 (1989)
- [82] Scheurer F, Ohresser P, Carrière B, Deville J P, Baudoing-Savois R and Gauthier Y, "LEED analysis of ultra-thin cobalt layers grown on Cr(100)," *Surf. Sci.* 298 107 (1993)
- [83] Schmid M, Pinczolits M, Hebenstreit W, and Varga P, "Segregation of impurities on Cr(100) studied by AES and STM," *Surf. Sci.* **377**, 1023 (1997)

- [84] Fu C L and Freeman A J, "Surface ferromagnetism of Cr(001)," *Phys. Rev. B* **33** 1755 (1986)
- [85] Meier F, Pescia D, and Schriber T, "Oxygen-induced magnetism of the nonreconstructed chromium (100) surface," *Phys. Rev. Lett.* **48** 645 (1982)
- [86] Klebanoff L E, Robey S W, Liu G and Shirley D A, "Observation of a surface magnetic phase transition on Cr(100)," *Phys. Rev. B* **30** 1048 (1984)
- [87] Wiesendanger R, Güntherodt H J, Güntherodt G, Ganbino R J and Ruf R, "Observation of vacuum tunneling of spin-polarized electrons with the scanning tunneling microscope," *Phys. Rev. Lett.* **65**(2) 247 (1990)
- [88] Ikeda S, Hayakawa J, Ashizawa Y, Lee Y M, Miura K, Hasegawa H, Tsunoda M, Matsukura F and Ohno H, "Tunnel magnetoresistance of 604% at 300 K by suppression of Ta diffusion in CoFeB/MgO/CoFeB pseudo-spin-valves annealed at high temperature," *Appl. Phys. Lett.* **93** 082508 (2008)
- [89] Deac A M, Fukushima A, Kubota H, Maehara H, Suzuki Y, Yuasa S, Nagamine Y, Tsunekawa K, Djayaprawira D D and Watanabe N, "Bias-driven high-power microwave emission from MgO-based tunnel magnetoresistance devices," *Nature Physics* **4** 803 (2008)